UNIVERSITY OF SOUTHAMPTON

Faculty of Engineering and the Environment

Identification and Attenuation of Slat Noise

by

Peng Chen

Thesis for the degree of Doctor of Philosophy

April_2012

ABSTRACT

In the case of civil transport aircraft, engines were the dominant noise source until the advent of the high-bypass ratio engines in the early 1970s. Since then, airframe noise has become more important, particularly during the approach-to-landing stage of aircraft operations. The main components of airframe noise are the flap side edge, leading edge slat, and the landing gear. Experiments in both the wind tunnel and via fly-over measurements have shown that the slat noise is a major contributor to the overall airframe noise during the landing approach for a commercial aircraft.

To achieve the goal of reducing slat noise significantly without adversely affecting the aerodynamic performance of the wing, it is obligatory to improve the understanding of the mechanism of slat noise generation. Experiments and numerical simulations were performed to investigate the phenomena of slat noise. It was found that the slat broadband noise generation is governed by two kinds of mechanism. At a low angle of attack of the wing, the typical circulation region is not formed in the slat cove and the slat noise level is low. As the angle of attack increases to a certain value, vortical structures are intermittently generated due to flow interaction occuring between the shear layer originating from the slat cusp and the flow convected from the stagnation line on the main element. Intense slat noise is produced as the vortical structures approach the slat cove surface. With the angle of attack increasing further, the slat noise becomes weak again. The interaction effect tends to become weaker as the shear layer deviates away from the surface of the main element.

Two approaches with the aim of attenuating the slat noise were experimentally and numerically studied. The first approach was to reduce the slat noise using air blown on the suction surface of the slat near its trailing edge. A numerical simulation showed that the slat noise levels over most of the frequencies, especially above a *St* number of 7, were obviously attenuated. In the second approach, a strip mounted on the pressure surface of the main element model was experimentally proven to be an effective method for reducing the broadband slat noise at an angle of attack of 8 degrees and a freestream velocity of 25 m/s. The position and height of the strip also influenced the level of the reduction.

Several tonal noise components appear in the slat noise spectrum at an angle of attack of 4 degrees and a freestream velocity of 25 m/s. The dominant tone is associated with the vortex shedding off the slat cusp through the Kelvin-Helmholtz instability. This tone was successfully suppressed using a plasma actuator employing an open-loop control. A maximum reduction of 11 dB was achieved at a *St* number of approximately 19.7. A quasi-static feedback control system was also developed, wherein a controller is responsible for calculating the control inputs in terms of feedback signals. The experimental results show that the controller can work effectively to suppress the slat noise.

Contents

List of figures

List of tables

DECLARATION OF AUTHORSHIP

I, Peng Chen

declare that the thesis entitled

Identification and Attenuation of Slat Noise

and the work presented in the thesis are both my own, and have been generated by me as the result of my own original research. I confirm that:

- this work was done wholly or mainly while in candidature for a research degree at this University;
- where any part of this thesis has previously been submitted for a degree or any other qualification at this University or any other institution, this has been clearly stated;
- where I have consulted the published work of others, this is always clearly attributed;
- where I have quoted from the work of others, the source is always given. With the exception of such quotations, this thesis is entirely my own work;
- I have acknowledged all main sources of help;
- where the thesis is based on work done by myself jointly with others, I have made clear exactly what was done by others and what I have contributed myself;
- none of this work has been published before submission, or [delete as appropriate] parts of this work have been published as: [please list references]

Signed: ……………………………………………………………………..

Date:……………………………………………………………………….

Acknowledgements

Foremost, I would like to acknowledge my supervisor, Professor Xin Zhang, for his invaluable guidance and huge encouragement throughout the course of my research. His professionalism and kindness make the study with him very rewarding and gratifying.

I am very grateful to Dr. David Angland for his patience and valuable advice on the paper writing. I would also like to thank Dr. David Marshall for his arrangement of the experimental model building and access to the wind tunnel and instruments. Thanks to Zhonglun Cai for his advice on the feedback control algorithm. Thanks also to Scott Chappell for his advice on the thesis writing.

Finally, thanks to my parents, Xiangtai Chen and Qingzheng Liu, for their constant support and also to my wife, Junrong Cao, for her tremendous support and encouragement throughout the duration of my studies.

Definitions and abbreviations

Alphanumeric Symbols

a_0	Speed of sound, m/s
A	Wing area, m^2
B	Total specific enthalpy, m^2/s^2
$\bar{c}$	Mean aerodynamic chord, m
c_{DES}	Empirical constant in DES model
C_l	Lift coefficient
c_s	Slat chord, m
c_m	Main element chord, m
d	Distance from a cell to the closest wall surface in S-A model
D	Depth of cavity, m
e_{ij}	The (i, j)th component of viscous stress tensor
E	Electric field
f	Frequency, Hz
f_b^*	Body force generated by plasma actuator, N
g	Green's function
g_s	Vertical overlap of slat
h	Spacing of grid
H	Heaviside function
i	Specific enthalpy, m^2/s^2

I	Sound intensity, W/m^2
I_A	Sound power, W/s
k	Wave number
L	Lamb vector, m/s^2
L_c	Length of cavity, m
Ma	Mach number
$\vec{n}$	Normal unit vector directed outside the integration surface
o_s	Horizontal gap of slat
p	Pressure, Pa
P_{plasma}	Power consumed by plasma actuator, W
q	Dynamic pressure, N/m^2
q^{-1}	Backwards shift operator in ARX
r	Distance from sound source to observer, m
$\mathbf{r}$	Vector from sound source to observer, m
R	Curvature radius, m
Re	Reynolds number
S	Control surface in FW-H equation
St	Strouhal number
$\overline{S_{ij}}$	Strain rate tensor
t	Time, s
T_{ij}	Lighthill stress tensor, N/m^2
u_d	Duty cycle, control input to plasma actuator

u_s	Local flow velocity, m/s
u_x, u_y, u_z	Cartesian velocity vector components, m/s
V	Control volume in FW-H equation
W	Weight of aircraft, kg
w_b	Measurement noise in system identification
W_c	Overlap of electrode of plasma actuator, m
W_g	Width of the coated electrode of plasma actuator, m
w_j	Process noise in system identification
x_i, x_j, x_k	Cartesian coordinates vector components, m
y^+	Non-dimensional wall distance

Greek Symbols

δ	Kronecker delta
δ_s	Slat deflection angle, degrees
δ_F	Flap deflection angle, degrees
ε	Turbulence dissipation rate
ϵ	Error component
ε_0	Permittivity of free space
λ	Acoustic wavelength
λ_D	Debye length
μ	Viscosity of the fluid, kg/ms
μ^*	Displace thickness, *m*

μ_t	Turbulent viscosity
$\tilde{\nu}$	Eddy viscosity
φ	Electric potential
η, τ	Curvilinear coordinates
ρ	Fluid density, kg/m^3
τ	Turbulence stress tensor
τ_e	Retarded time, s
ϕ_i	Empirical basis in POD
ω	Angular frequency
ω_z	Vorticity in z direction

Subscripts or Superscripts

$\overline{()}$	Ensemble or time averaged
$()^T$	Matrix transpose
$()'$	Perturbation value
$()_{AC}$	Alternative current
$()_{FS}$	Full scale
$()_{peak}$	Peak value
$()_{rms}$	Reference value
$()_{rms}$	Value of root mean square
$()_{SS}$	Small scale
$()_{total}$	Total value

$\dot{()}$	Derivative with respect to time
$()_\infty$	Freestream/reference value

Abbreviations and Acronyms

2D	Two-dimensional
3D	Three-dimensional
AC	Alternative current
AOA	Angle of attack of wing
ARX	Auto-regressive/exogenous
CAA	Computational aeroacoustics
CFD	Computational fluid dynamics
CSM	Cross spectral matrix
D/A	Digital-to-analogue
DBD	Dielectric barrier discharge
DC	Direct current
DDES	Delayed detached eddy simulation
DES	Detached eddy simulation
DRP	Dispersion Relation Preserving
DNS	Direct numerical simulation
E	Electric field
FD	Finite difference
FW-H	Ffowcs Williams and Hawkings

LED	Light-emitting diode
LES	Large eddy simulation
LQE	Linear quadratic estimator
LQG	Linear-Quadratic-Gaussian
LQI	Linear quadratic integral
N-S	Navier-Stokes
P	Power, W
PIV	Particle image velocimetry
POD	Proper orthogonal decomposition
PSD	Power spectral density
PWM	Pulse width modulation
RANS	Reynolds-averaged Navier-Stokes
RMS	Root mean square
S-A	Spalart-Allmaras
SDBD	Single dielectric barrier discharge
SGS	Sub-grid stress
SPL	Sound pressure level, with a reference pressure of 20 μ Pa
SNR	Signal-to-noise ratio
TKE	Turbulent kinetic energy
URANS	Unsteady Reynolds-averaged Navier-Stokes

Chapter 1

Introduction

1.1 Overview

Aeroacoustics is a branch of acoustics that is concerned with the noise generated by either unsteady aerodynamic forces or turbulent fluid motion. According to the Goldstein's[1] definition, aeroacoustics is concerned with the sound generated by aerodynamic forces or motions originating in a flow rather than by the externally applied forces or motions of classical acoustics. The academic discipline of aeroacoustics has gradually become more important and gained greater recognition since aviation noise became a public issue in the late 1960s. Aircraft noise covers a broad range of noise originating from various components including jet noise, turbomachinery noise, combustor noise and airframe noise. Historically, engine noise was the most dominant from amongst all these various noise sources. However, since the advent of the first twin cycle bypass turbofan engines in the early 1970s, engine noise has been reduced to a level comparable to airframe noise under approach and landing conditions. To satisfy the requirements of the European ACARE Visions 2020[2] that state that by 2020 aircraft noise should be reduced by 10 dB per operation, relative to the year 2000, airframe noise has been attracting extensive over the past decade. These studies have identified that high-lift devices and landing gears are the dominant sources for airframe noise[3]. An important component of the high-lift devices, the leading edge slat contributes significantly to the airframe noise.[4-6] This current study is thus motivated by the need to understand the mechanism of slat noise generation and to develop effective methods for its attenuation.

1.2 Literature Review

1.2.1 Aeroacoustic Analogy Theory

Lighthill was the first to establish the fundamental theory on aeroacoustics. The Lighthill acoustic analogy equation[7-8] links unsteady flow with noise generation. Based on the equation, several extensions were proposed, including the Ffowcs Williams and Hawkings equation (FW-H equation)[9], the Powell equation[10] and the Howe equation[11].

The Lighthill equation is a crucial tool for analysis and simulation in many aeroacoustic fields. The equation is briefly derived as follows. The continuity and momentum equations can be written as

$$\frac{\partial \rho}{\partial t} + \frac{\partial}{\partial x_j}\rho u_j = 0 \qquad (1.1)$$

$$\rho\left(\frac{\partial u_i}{\partial t} + u_j\frac{\partial}{\partial x_j}u_i\right) = -\frac{\partial p}{\partial x_i} + \frac{\partial e_{ij}}{\partial x_j} \qquad (1.2)$$

where e_{ij} is the (*i, j*)th component of the viscous stress tensor. For a Stokesian gas, the viscous stress tensor can be expressed in terms of the velocity gradients

$$e_{ij} = \mu\left(\frac{\partial u_i}{\partial x_j} + \frac{\partial u_j}{\partial x_i} - \frac{2}{3}\delta_{ij}\frac{\partial u_k}{\partial x_k}\right) \qquad (1.3)$$

where μ is the viscosity of the fluid and δ_{ij}denotes the Kronecker delta. Multiplying Equation (1.1) by u_i, and adding the result to Equation (1.2) yields

$$\frac{\partial \rho u_i}{\partial t} = -\frac{\partial}{\partial x_j}(\rho u_i u_j + \delta_{ij}p - e_{ij}) \qquad (1.4)$$

adding the term of $a_0^2\partial\rho/\partial x_j$ to Equation (1.4) gives

$$\frac{\partial \rho u_i}{\partial t} + a_0^2\frac{\partial \rho}{\partial x_j} = -\frac{\partial T_{ij}}{\partial x_j} \qquad (1.5)$$

where subscript 0 denotes the constant reference values, which are taken to be the corresponding properties of the undisturbed freestream, a_0 is sound speed at rest medium and

$$T_{ij} = \rho u_i u_j + \delta_{ij}[(p - p_0) - a_0^2(\rho - \rho_0)] - e_{ij} \qquad (1.6)$$

is Lighthill's turbulence stress tensor. Finally, differentiating Equation (1.1) with respect to time *t*, and subtracting the divergence of Equation (1.5) yields the Lighthill equation

$$\frac{\partial^2 \rho'}{\partial t^2} - a_0^2\nabla^2\rho' = \frac{\partial^2 T_{ij}}{\partial x_i \partial x_j} \qquad (1.7)$$

Equation (1.7) has the same form as the wave equation governing the propagation of sound by a quadrupole source $\partial^2 T_{ij}/\partial x_i \partial x_j$ in a non-moving medium[1]. It is clear that the flow field has to be solved prior to the acoustic field. Under some conditions, Lighthill's turbulence stress tensor T_{ij} can be simplified. For example, within the flow of a high Reynolds (*Re*) number, the viscous stress e_{ij} is negligible when compared with the Reynolds stress term $\rho u_i u_j$, because the ratio between the Reynolds stress and the viscous stress is of the order of the magnitude of the *Re* number[1]. Within an isentropic flow, the term $(p - p_0) - a_0^2(\rho - \rho_0)$ can be neglected because of $p - p_0 \approx a_0^2(\rho - \rho_0)$. Therefore, in most aeroacoustic applications the Reynolds stress term is always dominant over the other terms.

Green's function also plays an important role in obtaining the solution to the Lighthill equation. The Greens function $g(x,t|y,\tau)$is the response to a sound pulse

$$\left(\frac{1}{a_0^2}\frac{\partial^2}{\partial t^2} - \frac{\partial^2}{\partial {x_i}^2}\right) g(x,t|y,\tau) = \delta(x-y)\delta(t-\tau) \tag{1.8}$$

Equation (1.8) expresses that as a sound pulse is released at source position *y* at time *τ* , a corresponding response at observer *x* at time *t* is measured by *g*. In two dimensional (2D) space, Green's function becomes

$$g(x,t|y,\tau) = \frac{1}{2\pi a_0^2}\frac{H(g)}{\sqrt{t^2 - r^2/a_0^2}}, \qquad g = \tau - t + r/a_0 \tag{1.9}$$

where *r* denotes the distance from the source to the observer and H represents the Heaviside function. The Green's function in 3D free space is

$$g(x,t|y,\tau) = \frac{\delta(g)}{4\pi r} \tag{1.10}$$

The Lighthill equation (1.7) can be used to predict the noise generated from unsteady flows in the absence of solid boundaries. However, the presence of solid boundaries plays a direct role in noise generation and is of practical interest in many cases. Consider that a body is enclosed by a control surface *S*, and define the control volume *V* on the fluid side of *S*, the outer normal *n* on *S* is directed towards the body enclosed by *S*. The solution to the Lighthill equation can be written as[1]

$$\begin{aligned} \rho'(x,t) = &\frac{1}{a_0^2}\int\int_V \frac{\partial^2 g}{\partial y_i y_j} T_{ij} d^3 y d\tau + \frac{1}{a_0^2}\int\int_S \frac{\partial g}{\partial y_i} f_i d^2 y d\tau \\ &+ \frac{1}{a_0^2}\int\int_S \rho_0 u_n d^2 y d\tau \end{aligned} \tag{1.11}$$

where

$$f_i \equiv -n_i(p - p_0) + n_j e_{ij} \tag{1.12}$$

is the i^{th} component of the force per unit area exerted by the boundaries on the fluid. The first term in Equation (1.11) on the right-hand side represents the sound generated by a volumetric source, which behaves as an acoustic quadrupole. The second term represents the sound produced by unsteady forces exerted on the fluid by the solid boundaries, which behave as an acoustic dipole. The third term represents the sound generated by volume displacements, which behaves as an acoustic monopole.

An acoustic monopole is generally associated with the time dependent displacement of the fluid. Hence it is also referred to as the thickness noise. The sound pressures radiated by the monopole in all directions are the same. Thus the monopole appears as a circle in a directivity pattern. An acoustic dipole consists of two monopoles with equal source strength and opposite phases, separated by a small distance comparative to the wavelengths of the source. The axis of the dipole is aligned along the line which links the two monopoles. The directivity pattern of the dipole shows two lobes with the maxima along the axis. In aeroacoustic problems, a dipole is usually generated by a fluctuating force exerted on the fluid by solid boundaries. Looking at the generation of the aeroacoustic dipole, Goldstein[1] decomposed the velocity fluctuation into solenoidal (zero divergence) and irrotational (zero curl) parts in such a way that the pressure fluctuation is determined only by the irrotational part. The irrotational part is also called the acoustic particle velocity, and the solenoidal part the vortical velocity. In the flow far away from solid boundaries the two parts behave as if the other were not present. However, in the presence of a solid boundary the two parts interact due to the fact that the total velocity must satisfy the boundary condition. It is the coupling between the two parts that generates the acoustic dipole at a solid surface. Meanwhile, since the coupling is a linear process, it can be assumed that the dipole source dominates over the nonlinear quadrupole volumetric source. Powell[12] reformulated Curle's solution to the Lighthill equation using a rigid wall (zero normal-gradient) Green's function, and demonstrated that the normal stress dipole is the image of the Reynolds stress quadrupole. An acoustic quadrupole consists of two identical dipoles which are opposite in phase. There are two types of quadrupole: lateral quadrupole and longitudinal quadrupole. A lateral quadrupole has two axes not aligned along the same line; hence four lobes appear in its directivity pattern. By contrast, a longitudinal quadrupole consists of two dipoles with axes aligned along the same line. Therefore, only two lobes appear in its directivity diagram. In aeroacoustics, the lateral quadrupole commonly corresponds to shear stresses in turbulent flows, whilst the longitudinal quadrupole corresponds to normal stresses. It is well known that turbulent regions near solid surfaces are better acoustic radiators than those far from solid surfaces, and turbulent regions near sharp edges are even better noise radiators[13]. This stems from the fact that the turbulent flow generates acoustic dipole pattern noise in the regions near the solid surfaces or sharp edges, whilst generating quadrupole pattern noise in the regions far from the surfaces. The quadrupole pattern is much weaker in its capacity for noise radiation when compared with that of a dipole pattern.

When the control surface is stationary and the Green function in free space is employed, the Curle equation[14] can be derived from Equation (1.11)

$$
\begin{aligned}
\rho^{'}(x,t) = &\frac{1}{4\pi a_0^4}\int_V \frac{r_i r_j}{r^2}\frac{\partial^2}{\partial t^2} T_{ij}\left(y, t-\frac{r}{a_0}\right) d^3y \\
&+\frac{1}{4\pi a_0^3}\int_S \frac{r_i}{r^2}\frac{\partial}{\partial t} n_j p_{ij}\left(y, t-\frac{r}{a_0}\right) d^2y
\end{aligned}
\tag{1.13}
$$

The more general solution to the Lighthill equation is the FW-H equation[14], which allows the control surfaces to be movable

$$
\begin{aligned}
\rho^{'} = \quad &\frac{1}{4\pi a_0^2}\frac{\partial^2}{\partial x_i \partial x_j}\int_V \left[\frac{T_{ij}}{r\left|1-\frac{\boldsymbol{r}}{r}\cdot Ma\right|}\right]_{\tau=\tau_e} d^3y \\
&-\frac{1}{4\pi a_0^2}\frac{\partial}{\partial x_i}\int_S \left[\frac{f_i}{r\left|1-\frac{\boldsymbol{r}}{r}\cdot Ma\right|}\right]_{\tau=\tau_e} d^2y \\
&-\frac{1}{4\pi a_0^2}\frac{\partial}{\partial x_i}\int_V \left[\frac{\rho_0 a_i}{r\left|1-\frac{\boldsymbol{r}}{r}\cdot Ma\right|}\right]_{\tau=\tau_e} d^3y \\
&+\frac{1}{4\pi a_0^2}\frac{\partial}{\partial x_i \partial x_j}\int_V \left[\frac{\rho_0 u_i u_j}{r\left|1-\frac{\boldsymbol{r}}{r}\cdot Ma\right|}\right]_{\tau=\tau_e} d^3y
\end{aligned}
\tag{1.14}
$$

where the notation $[]_{\tau=\tau_e}$ indicates that the quantity enclosed within the brackets should be evaluated at the position y and the retarded time τ_e, obtained by solving the following equation:

$$
\tau_e - t + \frac{1}{a_0}|x-y| = 0 \tag{1.15}
$$

The control surface in Equation (1.14) can be an open surface[15]. This is especially useful when vortical turbulences pass through the control surface, where the contribution from the turbulence stress shows a spurious fluctuation which can dominate the predicted noise. The open surface, which doesn't let the vortical turbulences pass through the control surface, ensures that no spurious sound is generated[16]. Wang *et al.*[17] developed an effective treatment of this error in the context of the Lighthill equation.

In the implementation of the solution to the FW-H Equation, it is general practice to ignore the quadrupole noise sources. This is because commonly the dipole sources dominate over the quadrupole sources, and assessing the quadrupole sources costs significant computational resources. However, in some cases, the quadrupole sources are not negligible; Brentner and Farassat[18] show that the quadrupole terms contribute significantly to helicopter rotor noise.

Howe[11] introduced a different formulation for the equivalent sources: the Lamb vector $\omega \times u$. At a low *Ma* number, the acoustic pressure in the far-field generated by an unsteady flow in the presence of a rigid body is

$$p'(x,t) = -\rho_0 \iint_V (\omega \times u) \frac{\partial g}{\partial y_i} d^3 y d\tau \tag{1.16}$$

As well as all the methods mentioned above, Kirchhoff's surface-integral method[19] is another way to predict the sound generated by unsteady flow. This method analyses pressure and its normal derivative distribution over a surface, enclosing all the noise sources as an input to predict the sound field outside the surface.

1.2.2 Role of the Slat in Airframe Noise

In the field of aeronautics, engines were the dominant noise source during all flight stages until the advent of the high-bypass ratio engines. Since then, the airframe noise has become important during the approach-to-landing stage. The main components of airframe noise are the flap side edge, the slat, and the landing gear. Soderman *et al.*[20] identified airframe noise sources on a 7% scaled unpowered Bombardier CRJ-700 aircraft model in the NASA Ames 7 by 10 ft wind tunnel, and Guo and Joshi[6] conducted experiments on a 4.7% scaled model of the McDonnell Douglas DC-10 transport airplane in the 40 by 80 ft wind tunnel at the NASA Ames Research Center; both experiments proved that the slat was a crucial noise source. Dobrzynski and Pott-Pollenske[21] performed an experiment on a full scale wing equipped with high lift devices, and found that both the slat and the side edge of the trailing flap contributed significantly to the airframe noise. Figure 1.1 shows the typical results of fly-over measurements[22] on an Airbus A340. It can be seen that the main noise sources are the landing gear, slat and flap. The landing gear contributes the most to the total airframe noise, whilst the flap contributes the least. However, the slat noise is comparable to the landing gear noise in the rearward arc.

1.2.3 Mechanism of Slat Noise Generation

To achieve the goal of significantly mitigating the slat noise, it is first necessary to improve the general understanding of the mechanisms behind the slat noise generation. Various tools, such as wind tunnel tests, fly-over measurements and numerical simulations, all contribute to the investigation of the slat noise.

A slat is an aerodynamic device generally employed in multi-element airfoil configurations to increase the maximum lift. The main purpose of the slat is to reenergize the flow above the suction surface of the main element by providing high speed flow through the slat gap. Although the slat itself does not account for a major portion of the lift augmentation, it does allow the wing to operate effectively at higher angles of attack[23]. However, employment of the slat leads to an unpleasant side-issue: slat noise. Slat noise represents a complex aeroacoustic problem; the underlying mechanisms governing the generation of slat noise have been extensively explored over the past several decades but are still far from clarity. When considering the crucial features of slat noise, it is generally agreed that slat noise is broadband in nature and in some cases superimposed by tonal components[23-24]. One of the tonal components is related to the coherent vortex shedding off a blunt slat trailing edge. However, the tone is unlikely to appear on a full scale slat because the relative trailing edge thickness is smaller than that of a scaled slat. The other two tonal components are assumed to be the consequence of too low *Re* numbers[25]. The low frequency component is generated near the slat cusp due to the coherent laminar flow separation. The high frequency component is generated on the slat suction surface due to the Tollmien–Schlichting boundary layer instability (for a 1/10 scaled high-lift model, low frequency corresponds to a frequency range from 1 kHz to 4 kHz and high frequency is from 10 kHz to 20 kHz). Nonetheless, other mechanisms concerned with the generation of the tonal components have also been proposed. Tam and Pastouchenko[26] suggested that the frequency at which a vortex was shed off a blunt trailing edge of a slat was not simply associated with the thickness. In their research, the bluntness parameter h/μ^* covered a range from 0.24 to 0.55, where h was the thickness of the trailing edge, and μ^* was the displaced thickness of the boundary layer at the trailing edge. The tonal noise was generated throughout the entire range of bluntness parameters, even those less than 0.3. This was not in accordance with previous research, which assumed that the tone was negligible at bluntness parameters of less than 0.3. Therefore, Tam and Pastouchenko suggested that the tonal noise was regulated by a kind of feedback loop; accompanying the shedding of a vortex at the trailing edge, an acoustic pulse was generated which was then reflected back by the surface of the main element. As the echoed pulse stroked the trailing edge, another vortex was shed off, and the shedding of the new vortex led to the emission of another acoustic pulse. Therefore, the tone was attributed to the repeated cycle of the vortex shedding off the trailing edge.

Roger and Perennes[27] claimed that one of tonal components shared the same mechanism as cavity tones. Their experiment was conducted on a 2D 1/11 scaled wing. The most prominent feature in the experiment was the generation of narrowband noise, wherein the frequency of the narrowband noise agreed well with the frequency predicted using the Rossiter formula[28] provided that the distance between the slat cusp and the trailing edge was the determinant parameter.

With respect to the slat broadband noise, several models have been proposed. Molin and Roger[29] attributed the slat broadband noise to the interaction of the turbulent structures originated inside the slat cove and the leading edge of the main element. Dobrzynski and Pott-Pollenske[21] conjectured that the slat noise arose from the interaction between the vortex originating from the unsteadiness in the slat cove and the slat trailing edge. However, a more general view about the broadband noise generation is as follows. The free shear layer shedding off the slat cusp is a good amplifier for initial perturbations. This results in a process of vortex rollup and then the formation of discrete vortices. As the shear layer impinges on the cove surface of the slat, those vortices experience severe stretching and distortion due to the rapid deceleration and subsequent acceleration within the local flow field. This process is regarded as the main reason for the generation of slat broadband noise in several articles[23, 30]. After the impingement, a significant fraction of the vortical structures are convected past the trailing edge of the slat but the remaining structures get trapped within the recirculation zone, convecting back to the cusp. Those trapped in the cove induce further unsteady eruptions of secondary vortices along the cove surface.

1.2.4 Approaches for Reducing Slat Noise

Any approach developed for slat noise reduction must also take into account the aerodynamic performance of the wing. One important parameter is the maximum lift coefficient, which determines the minimum landing speed. If the maximum lift coefficient is decreased by 10 percent due to an approach used for slat noise reduction, the landing speed must increase by about 5.4 percent. The increase of the landing speed leads to a 1.4 dB increase in the slat noise, which compromises the achieved benefit by the noise attenuation approach[25]. Several approaches which aim to attenuate the slat noise were proposed and verified over the last decade. Those approaches can be grouped into three categories. The first category, named the fairing method, prevents the generation of the free shear layer. The second category looks at the absorption of noise; with partial surfaces of the slat or main element equipped with a liner or other noise absorbent materials, the slat noise can be absorbed. The third is called noise control, which uses passive or active remedies to restrain the generation of slat noise.

Fairing: As described above, the shear layer shedding off the slat cusp plays a key role in the generation of slat broadband noise. If the vorticity intensity in the free shear layer is suppressed, the slat noise would be reduced. Dobrzynski *et al.*[31] showed that a slat cove cover was a promising method for broadband noise reduction. The slat noise within most of the frequency range was reduced by several dBs. A samilar idea with an extended seal attached to the slat cusp was tested by Khorrami and Lockard[32]. Streamlined fillers, which completely fill the slat cove with a streamlined body, were tested by NASA, the European Aeronautic Defence and Space Company and the Japanese Aerospace Exploration Agency[33-35]. All the corresponding results demonstrated a significant noise reduction.

Treatment of the trailing edge: It is known that tonal noise can be produced as vortices shed off a blunt trailing edge. Various efforts which aim to reduce the tonal noise have been made in recent years. Soderman[20] demonstrated a successful application using serrations flush mounted on the suction surface of a slat, near the trailing edge. The results showed that the serrations reduced the area of the noise source, although the sound level went up slightly at the core region of the noise source. Chow *et al.*[22] demonstrated that blushes flush mounted on the suction surface of a slat near the trailing edge could also reduce the slat noise significantly, especially at low frequencies. It is already known that the blunt trailing edge is closely associated with the tones at high frequencies. Therefore, the underlying mechanism, by which the noise at a low frequency was reduced, should deserve much attention. Pott-Pollenske[36] illustrated that the slat noise could be reduced using a perforated trailing slat. The results showed that the slat noise level within a frequency range from 2 kHz to 4 kHz was reduced by 2 to 3 dB, however a significant noise increase at higher frequencies (higher than30 kHz) was then introduced. This was presumably caused by the interaction between the flow near the trailing edge and the micro-perforations.

Liner: Ma *et al.*[37] performed a numerical simulation, wherein partial surfaces of the slat and the main element were equipped with liners. The results showed that the slat noise level was reduced by 2 to 3 dB. Similar works were experimentally conducted by Pott-Pollenske[36], who equipped the surfaces of the slat cove and the leading edge of the main element with liners. Measurements showed that the slat noise was reduced by up to 3 dB within the frequency range from 0.8 to 5 kHz, with a slight increase at higher frequencies.

1.2.5 Scaling Law

Geometric scaling law: Aeroacoustic measurements in wind tunnels are often performed on a scaled model. The sound levels and frequencies associated with the scaled model should be adjusted based on the scale factor SF (the ratio of characteristic length between a scaled model and the corresponding full scale aircraft). The sound levels scaling law can be written as

$$\mathrm{SPL}_{fs} = \mathrm{SPL}_{ss} + 20\log(\frac{1}{\mathrm{SF}}) \tag{1.17}$$

where subscripts *fs* and *ss* denote full scale and small scale respectively and SPL represents sound pressure level at a specific frequency. The frequency scaling law can be written as

$$f_{fs} = f_{ss}\mathrm{SF} \tag{1.18}$$

Mach number scaling law: Airframe noise is composed of a range of noise sources originating from various components. Crighton[38] claimed that the slat noise was analogous to a baffled or free acoustic dipole. Hence the slat noise level should be an exponent of five with the *Ma* number. However, not all the measurements comply with this rule. Dobrzynski and Pott-Pollenske[21] conducted acoustic measurements on several models and showed that the slat noise level had a best fit with a power law of 4.5 of the *Ma* number. Soderman *et al.*[20] conducted an acoustic measurement on a 7 percent scaled unpowered Bombardier CRJ-700 aircraft in the NASA Ames 7ft by 10 ft wind tunnel. In the experiment, the *Ma* numbers were set at 0.22 and 0.26. The results showed that an exponent of six with the *Ma* numbers gave a better fit at the frequencies below 10 kHz, whereas an exponent of five was more suitable at the frequencies above 10 kHz. Guo[6] made an analysis on slat noise segmented into two bands, with a low frequency band from 0.1 to 10 kHz and a high frequency band from 10 to 100 kHz. For the low frequency band, the corresponding wavelengths were sufficiently long so that the distance between noise sources with any sharp edges were shorter than one wavelength. In this case, the noise radiation was dominated by sharp edge diffraction, which was typically governed by a power law of five with the *Ma* number. However, the noise within the high frequency band was closely related to the unsteady forces exerted on the fluid by the solid boundaries and corresponded to the acoustic dipoles. Therefore, a sixth power law dependence was more suitable.

1.2.6 Component Based Model for the Prediction of Slat Noise

Prediction at cruise configuration: Airframe noise levels for aircraft in their cruise configuration are 7 to 10 dB less than when they have deployed their high lift devices, and are considered as the ultimate airframe noise barrier[39]. Lockard and Lilley[40] deemed that the radiated noise from a clean airframe was dominated by the scattering of noise from the wing trailing edge. A component based model for the prediction of airframe noise levels was then presented based on this assumption. The radiated noise from the wing of an aircraft flying straight and level in a clean configuration with a lift coefficient less than 0.5 can be written as

$$I = \frac{13.6}{\pi^3} u_\infty Ma^2 \left(\frac{u_{rms}^t}{u_\infty}\right)^5 \frac{W}{C_l r^2} \tag{1.19}$$

where u_{rms}^t is the turbulent fluctuating velocity at the trailing edge of a wing, which can be obtained from numerical simulation or experimental measurements, W is the weight of the aircraft, and r is the distance from the wing to an observer. However, the radiated noise from the wing of an aircraft flying in the approaching stage with a lift coefficient from 1.5 to 1.7 can be written as

$$I = \frac{1.7}{\pi^3}\left(1 + \frac{1}{4}{C_l}^2\right)^4 \frac{u_\infty Ma^2 W}{C_l r^2} \tag{1.20}$$

The overall sound pressure level is given as

$$\mathrm{SPL}_{total} = 10\log\left(I/I_{ref}\right) + K = 120\ dB + 10\log(I) + K \tag{1.21}$$

where K is a constant and allows for a later adaptation to test data. The frequency, at which the spectral level achieves the maximum, is approximated as

$$f_{peak} = 492\frac{u_{rms}^t}{\bar{c}} \tag{1.22}$$

where $\bar{c}$ is the mean chord. Furthermore, the noise spectrum below the frequency of f_{peak} is the same as that of a white noise spectrum, while the noise level decreases with f^2 at a frequency higher than f_{peak}.

Noise prediction for high lift devices: Pott-Pollenske *et al.*[39] approximated the noise spectrum of the high lift devices by two straight lines for fully deflected slats and flaps

$$\begin{aligned} \mathrm{SPL}_{norm,1} &= K_1 + 3\log(St) + \Delta\mathrm{SPL}_{S,F} && \text{for } St \le St_s \\ \mathrm{SPL}_{norm,2} &= K_2 - 18\log(St) && \text{for } St \ge St_s \end{aligned} \tag{1.23}$$

where St_s is the St number at which the two straight lines are intersected, constants K_1 and K_2 are introduced to allow for a later adaptation to experimental data, and

$\Delta\mathrm{SPL}_{S,F}$ is introduced to account for the effects of slat and flap deflections. For $St \leq St_s$, the $\Delta\mathrm{SPL}_{S,F}$ can be given as

$$\Delta\mathrm{SPL}_{S,F} = -15.6 + 0.416(\delta_s + \delta_F) - 0.0025(\delta_s + \delta_F)^2 \tag{1.24}$$

where $\delta_s$and δ_F are the deflection angle for the slat and flap respectively. Finally, the slat noise can be estimated according to the following equation

$$\begin{aligned} \mathrm{SPL}_{total} = {} & \mathrm{SPL}_{norm,1\,or\,2} + 10\log(D_x) + 10\log\left(D_y\right) + 50\log\left(\frac{u_\infty}{u_{ref}}\right) \\ & +30\log(\cos\psi) + 20\log\left(\frac{l}{r}\right) \end{aligned} \tag{1.25}$$

where l is the wetted trailing edge length, D_x and D_y are directivity factors with

$$\begin{aligned} D_x &= \left[\sin^2(\left|\varphi_x - \varepsilon + \alpha\right|) + 0.1\cos^2(\left|\varphi_x - \varepsilon + \alpha\right|)\right] \\ D_y &= 0.5\left[\left|\cos(\varphi_y - \nu)\right| + \left|\cos(\varphi_y + \nu)\right|\right] \end{aligned} \tag{1.26}$$

the definitions of other parameters in Equations (1.25) and (1.26) are shown in Figure 1.2.

Guo[6] developed a set of empirical functions based on the experimental data associated with the Boeing aircraft. The functions can be used to predict the noise spectra associated with a particular component in the far-field. The formula tells

$$\mathrm{SPL} = L_0 F(Sr) D(\theta) Ma^{b_1} C_l^{b_2} \left(\frac{l}{r}\right)^{b_3} (sin\alpha)^{b_4} (sin\delta)^{b_5} \tag{1.27}$$

where SPL is the noise spectrum for a particular component, L_0, b_1, b_2, b_3, b_4, b_5 are constants, $F(Sr)$ denotes normalized spectrum, l is the length of the component, r is the distance between the source and an observer, $D(\theta)$ is the directivity factor, μ is the directivity angle in the flyover plane, α is the angle of attack and δ is the deflection angle of the component.

1.2.7 Experimental Techniques

Experiments on the study of slat noise inevitably involve wind tunnels, experimental models, instruments etc. The main features of an acoustic wind tunnel include a low background noise level, equipped with an anechoic chamber, open jet nozzle etc. With respect to the background noise level, generally this should be 10 dB lower than the noise level of the tested model in the frequency range of interest. If the difference between them is less than 6 dB, the measurement accuracy becomes poor[41]. Jacob *et al.*[42] developed a method by which the tested model noise can be properly measured even if the background noise level is higher. In this method, two microphones at least are required, one close to the noise source and the other in the acoustic far-field. The tested model noise is separated from the background noise through the coherence of the signals measured by the two microphones. There are several typical acoustic wind tunnels, including the 40 ft × 80 ft wind tunnel at NASA Ames, the 8 m × 6 m wind tunnel at the DNW, the AWB wind tunnel at the DLR, and the 9 ft × 7 ft Low Speed Aeroacoustic Facility at Boeing, amongst others. For an aeroacoustic experiment in a wind tunnel, struts are employed to support microphones, models etc. However, the struts could induce intense noise if the vortices shed off the struts lead to periodic or quasi-periodic loads on the experimental model. When employed in an open jet wind tunnel, the microphone can be kept outside the airstream and thus avoid the negative influence by flow turbulence. However, when used in a closed test section, the microphone is often flush mounted onto the walls of the wind tunnel. In this case, the boundary layer turbulence can lead to a failure of the acoustic measurement. Recessing the wall-mounted microphone can avoid the issue, because even a small recess can result in a significant reduction of the boundary layer noise[42].

The phased microphone array is a useful tool for noise source locating. The basic theory about the phased microphone array is briefly presented as follows. Let an array consisting of M microphones be immersed in an acoustic field, the acoustic pressure sensed by the i^{th} microphone can be written as

$$p_i = s_i + \epsilon_i \tag{1.28}$$

where s_i represents the sound signal and ϵ_i denotes the error component. If the noise plane (a plane on which the sound power spectrum density will be measured) is divided into $N_i \times N_j$ grids, the Green's function g_i, which is defined on a specified node, and the i^{th} microphone can be calculated. Let the acoustic intensity at any node be I, the signal acquired by the i^{th} microphone is equal to $g_i I$. A matrix containing all grid nodes and microphones can be constructed as

$$p = gI + \epsilon \tag{1.29}$$

With

$$\begin{aligned} p^T &= [p_1, p_2, \cdots, p_M] \\ g^T &= [g_1, g_2, \cdots, g_M] \\ \epsilon^T &= [\epsilon_1, \epsilon_2, \cdots, \epsilon_M] \end{aligned} \tag{1.30}$$

where vector g is often referred to as the steering vector. The sound intensity at the specified node can be calculated by

$$I = \frac{g^T \langle pp^T \rangle g}{[gg^T]^2} \tag{1.31}$$

where the M × M matrix $\langle pp^T \rangle$ is called the cross-spectral matrix (CSM). However, several factors should be considered when the phased microphone array is employed in a wind tunnel experiment. For example, if an experiment has to be performed in a closed test section, strong background noise and reverberations can cause artefact maps of the noise source. This problem has been partially resolved over the last few years[43-45]. The assessment of the array performance depends on the array resolution and the average side lobe levels. The resolution of an array is a function of aperture size, frequency and distance between the microphone array and the experimental model. The size of a point source as it appears on a beamforming plot is the measure of the resolution of an array. The current design of an array employs an aperiodic pattern, in which the vector distance between any two microphones is not repeated, and therefore the adverse effects of spatial aliasing do not add up.

1.2.8 Numerical Simulation

The rapid development of computer capabilities and the increasing demands on the reduction of aeroacoustic noise have prompted the development of computational aeroacoustics (CAA). Aeroacoustic problems are by nature different from standard aerodynamics problems; aeroacoustic problems are time dependent whereas aerodynamics problems are commonly time independent. Tam[46] listed some of the major features of CAA when compared with the conventional CFD (computational fluid dynamics):

- In aeroacoustic problems, the sound pressure level in a wide frequency range needs to be computed. Therefore, numerical resolution of the high frequency waves with short wavelengths becomes an obstacle to accurate numerical simulation;
- Compared to the energy levels of unsteady flow fluctuations, the sound pressures of the acoustic waves have small amplitudes because only a minor fraction of the total energy of the mean flow can be radiated as sound. The

sound intensity is usually five to six orders smaller. To compute sound waves accurately, a numerical scheme must have low numerical noise;

- The sound level in the acoustic far-field is of interest rather than the near-field in most aeroacoustic problems. This needs a solution that is uniformly valid from the source regions all the way to the far-field. Therefore, CAA schemes must have minimal numerical dispersion and dissipation due to the long propagation distance;
- In aeroacoustic problems, the boundary conditions are different to standard aerodynamic problems. Acoustic waves decay slowly and can reach the boundaries of a computation domain, whilst flow disturbances generally decay faster and become small at the boundaries of the computation domain. Therefore, radiation and outflow boundary conditions should be imposed at the boundaries to avoid the spurious reflections of outgoing sound waves back into the computation domain.

Predicting the noise radiation associated with unsteady flows is the central theme of aeroacoustics. The unsteady flow can be computed at different levels of idealization in terms of various flow control equations. Based on the computed unsteady flow, different noise prediction approaches can be employed to obtain the radiated noise. Colonius and Lele[47] listed a hierarchy of noise prediction methods, which is shown in Figure 1.3. The numerical simulation of noise prediction can be classified into three broad categories: direct, indirect (or hybrid) and stochastic methods.

The stochastic method has the least computational cost when compared with the other two methods. It uses the results of the TKE (turbulent kinetic energy) and the corresponding turbulent length scale from the Reynolds-averaged Navier-Stokes (RANS) model solution to predict the noise[48]. Let the noise source term on the right side in the Equation (1.7) be represented by q(x, t), the sound density in the far-field can be expressed by integration over the source volume[48]

$$\overline{p'^2(x,\omega)} = \int_V \int_\xi g^*(x, y - {}^{\xi}/_{2}, \omega)\, g(x, y + {}^{\xi}/_{2}, \omega) q_{12}(x,\xi,\omega) d\xi d^3 y \qquad (1.32)$$

where $g^*$and g are the Green's function and its conjugate complex in the frequency domain, q_{12} is a cross spectral density, which is calculated from the Fourier transformation of the two-point space-time covariance of the sources (between source points $y_1 = y - \xi/2$ and $y_2 = y + \xi/2$) and a time separation τ

$$q_{12}(x,\xi,\omega) = \int_{-\infty}^{\infty} R(y,\xi,\tau) e^{i\omega\tau} d\tau \qquad (1.33)$$

with

$$R(y,\xi,\tau) = \overline{I\left(y - {}^{\xi}/_{2}, t - {}^{\tau}/_{2}\right) I\left(y + {}^{\xi}/_{2}, t + {}^{\tau}/_{2}\right)} \tag{1.34}$$

Equation (1.32) is the basis of the statistical method in the frequency domain, because the noise spectrum in the far-field is determined if the two-point space-time covariance of the sources represented by Equation (1.33) is known.

The direct method attempts to compute both the unsteady flow and the sound generation in one step. This method uses a domain that includes the noise generation flow region and a part of the near-acoustic-field[49]. High-fidelity approaches such as direct numerical simulation (DNS) and large eddy simulation (LES) are the best candidates for direct sound prediction. In DNS, both the energy containing range and the dissipative range of scales are resolved. However, the resolution of the energy containing scales requires a sufficiently large computational domain and long run time. In addition, resolution of the dissipative scales requires a sufficiently fine mesh. This renders DNS very time consuming and expensive in terms of computational resource. LES captures the energy containing eddies and models the effect of subgrid-scale (SGS) eddies. The subgrid model is established through a spatial filtering operation applied to the Navier-Stokes equations[50]. Since the Lighthill stress tensor at low *Ma* numbers can be approximated by $\rho_0 u_i u_j$, the effect of SGS modeling can be illuminated by decomposition of the Lighthill stress tensor[50]

$$\rho_0 u_i u_j = \underbrace{\rho_0 \overline{u_i}\,\overline{u_j}}_{T_{ij}^{LES}} + \underbrace{\rho_0\left(\overline{u_i u_j} - \overline{u_i}\,\overline{u_j}\right)}_{T_{ij}^{SGS}} + \underbrace{\rho_0\left(u_i u_j - \overline{u_i u_j}\right)}_{T_{ij}^{MSG}} \tag{1.35}$$

where the overbar denotes spatial filtering. The first term on the right side, T_{ij}^{LES}, denotes the Lighthill stress tensor evaluated from the resolved velocity field. The second term, T_{ij}^{SGS}, represents the subgrid scale values to the Lighthill stress at resolved scales. However, the subgrid scale values are generally inaccurate. The last term represents the unresolved part of the Lighthill stress. Therefore, a common practice for the Lighthill stress tensor calculations is to use merely the first term to represent the sound source. LES costs less computational resources than DNS. For example, to simulate a subsonic turbulent jet, the cost of DNS is proportional to Re^3/Ma^4, whilst it is only Re^2/Ma^4 for LES[51]. Nonetheless, in most cases of noise prediction, especially in the presence of solid boundaries and at high *Re* numbers, even LES is not always affordable. A crucial obstacle with LES is the requirement of strict near-wall grid resolution, which is nearly comparable to DNS[52]. Meanwhile, in some regions, such as the pressure side of a wing, crude modelling is sufficient. Therefore, a method, named hybrid RANS (Reynolds-averaged Navier-Stokes)/LES or detached eddy simulation (DES), was developed. Basically, the DES model is tailored according to the advantages of both RANS and LES. The RANS model is appropriate when employed in thin boundary layers due to the small and isotropic turbulence scale. Meanwhile the requirement of a grid in a RANS model is not as stringent as those used in LES, in which the grids need to be approximately isotropic. Therefore, the size of grid can be reduced dramatically. Due to the significant decrease of the computational cost compared with the DNS or LES, the DES method is clearly the most promising method to conduct unsteady flow simulations at present[53]. In DES, the switch between RANS and LES depends on a length scale $\tilde{d}$ which is defined as

$$\tilde{d} = \min(d, C_{des}\Delta) \tag{1.36}$$

where d is the distance to the closest wall surface, Δ is the largest grid spacing in x, y, or z directions, and C_{des} is an empirical constant of 0.65 for most cases. The DES performs either as a RANS solver as $d < C_{des}\Delta$, or LES as $d < C_{des}\Delta$. Since a computational domain in the DES is non-explicitly split into two zones, in principle two different turbulence models could be applied for the two zones. However, following the concept of Spalart[54-55], a Spalart-Allmaras (S-A) turbulence model[56] is generally employed either as a normal turbulence model in the RANS zones or as an SGS model in the LES zones.

The S-A model is based on Boussinesq's approximation, which describes the Reynolds stresses tensor $\rho u_i u_j$ as the product of the strain rate tensor $\overline{S_{ij}}$ and eddy viscosity $\tilde{v}$, which can be obtained by solving the flowing transport equation

$$\frac{\partial \rho\tilde{v}}{\partial t} + \frac{\partial}{\partial x_j}(\rho\tilde{v}u_i) = G_v + \frac{1}{\sigma_v}\left[\frac{\partial}{\partial x_j}(\mu + \rho\tilde{v})\frac{\partial\tilde{v}}{\partial x_j} + C_{b2}\rho\left(\frac{\partial\tilde{v}}{\partial x_j}\right)^2\right] - Y_v \tag{1.37}$$

where G_v is the production of turbulent viscosity and Y_v is the destruction of turbulence, C_{b2} and σ_v are constants which will be given in the following. Once the eddy viscosity $\tilde{v}$ is solved, the turbulent viscosity, v_t, can be obtained from

$$v_t = \rho\tilde{v}f_{v1}, \quad f_{v1} = \frac{\chi^3}{\chi^3 + C_{v1}^3}, \quad \chi \equiv \frac{\tilde{v}}{v} \tag{1.38}$$

where f_{v1} is the viscous damping function.

Finite-difference (FD) schemes are widely used in the majority of CAA studies because they can be easily extended to high-order accuracy. A centred approximation for $f_i^{\square} = \frac{\partial f}{\partial x}(x_i)$ at the node $x_i = h(i-1)$ on a uniform mesh can be written as[47]

$$\sum_{j=1}^{N_\alpha} \alpha_j (f'_{i+j} + f'_{i-j}) + f'_i = \frac{1}{h}\left(\sum_{j=1}^{N_a} a_j (f_{i+j} + f_{i-j}\right) + O(h^n) \tag{1.39}$$

where, if N_α = 0, the scheme is explicit, otherwise, the scheme is implicit or compact. The compact scheme requires the derivatives at all nodes to be resolved simultaneously. The coefficients α_j and a_j are chosen in terms of minimizing the truncation error for a given stencil width. For example, as N_a = 3 with a_1 = (496-15π)/42c, a_2 = (1725π -5632)/84c and a_3 = (272 -85π)/84c, c = 45π-128, the FD scheme becomes the well-known 'dispersion-relation-preserving' (DRP) scheme. Nonetheless, with an FD scheme several issues arise from the discretization of a partial differential equation. The first issue is the numerical dispersion. Invariably, a discretized equation behaves mathematically as a dispersive wave system[57-58]. For an original non-dispersive partial differential equation, the Fourier components of the solution travel with the same constant phase speed and waveforms comprised of the superposition of various modes retain their shape when propagating. However, in a discretized partial differential equation, the Fourier components of the solution travel with different phase speeds, and waveforms comprised of a superposition of modes do not retain their identity when propagating. The time derivative can be approximated by a single-step method such as the Runge–Kutta (RK) scheme. In such an approximation the group velocity corresponding to the discretized equation is not the same as its original equation. The second issue related to the FD scheme is numerical dissipation. The dissipation of the numerical solution depends critically on whether a central difference stencil or an asymmetric difference stencil is used. A central difference stencil is always linked with a non-dissipative scheme. However, a computation scheme should have the capability to suppress spurious short waves, which can be generated at the surfaces of discontinuities or computation boundaries[47]. These spurious short waves can not only contaminate the computation but can also cause numerical instability. It can be shown that an upwind asymmetric stencil can dampen the spurious waves and engender numerical stability. In addition, artificial dissipation and viscosity, and filtering of the dependent variables, can be used to suppress instabilities associated with the growth of spurious waves. The third issue related with the FD scheme is the aliasing. An FD scheme can only treat a fundamental wave number range, and the wave numbers that fall outside this range are under-resolved. They are aliased back inside the fundamental range, thus contaminating the computation.

The basic idea behind a hybrid method of noise prediction is concerned with the separation of noise sources from their propagation. In a common hybrid method, the unsteady flow simulation is performed first, followed by the acoustic propagation simulation or calculation of the sound using the FW-H equation. Several methodologies can be employed to implement the prediction, including DNS/LES with acoustic analogy, vortex methods with acoustic analogy, incompressible/acoustic split, or linearized Euler equations with source terms[47].

In a numerical simulation of an acoustic problem, the size of the computation domain should be considered. It is clear that the computation domain should be sufficiently large to contain all the sources of noise. However, there is no detailed guidance on the choice of the size of the computation domain[46]. Kurbatskii and Tam[59] performed a numerical investigation into the effect of the computation domain size on the cavity tone phenomenon, wherein three different sizes were used. Based on the results, they recommended that the computation domain boundaries should be placed at least one wavelength away from the sources.

1.3 Aims of this Research

In the literature review in the preceding section, the issues related with this research have been outlined. In particular, we have seen that the slat contributes significantly to the airframe noise, and the mechanisms which govern the generation of the slat noise are complicated and not fully understood. Few approaches are effective in attenuating the slat noise at present, and in most cases are accompanied with adverse side effects to the aerodynamic performance. The specific aims of this research are to:

- Investigate the relationship between the slat noise level and the angle of attack (AOA) of the main element by finding the difference of the noise sources at various AOAs;
- Develop approaches with the aim to attenuate the slat noise;
- Develop a feedback control using plasma actuators to reduce the slat noise.

1.4 Structure of the Thesis

This thesis is organized into six chapters. In Chapter 2, results from both experiments and numerical simulation on a scaled slat model are presented. Discussion is focused on the difference of noise sources at various AOAs. A potential mechanism, which governs the difference, is proposed. Chapter 3 is concerned with an active method which aims to reduce the slat noise using air being blown on the suction surface near the slat trailing edge. A passive method, in which a piece of strip was mounted on the surface of the main element near the leading edge, is also investigated. The corresponding results are presented in Chapter 4. Chapter 5 is mainly concerned with the development of a feedback control approach using a plasma actuator to suppress the slat noise and Chapter 6 presents the conclusions and suggestions for future work.

1.5 Summary

An overview of the topics central to this thesis has been presented. The aims of the research have been stated and the thesis structure has been outlined.

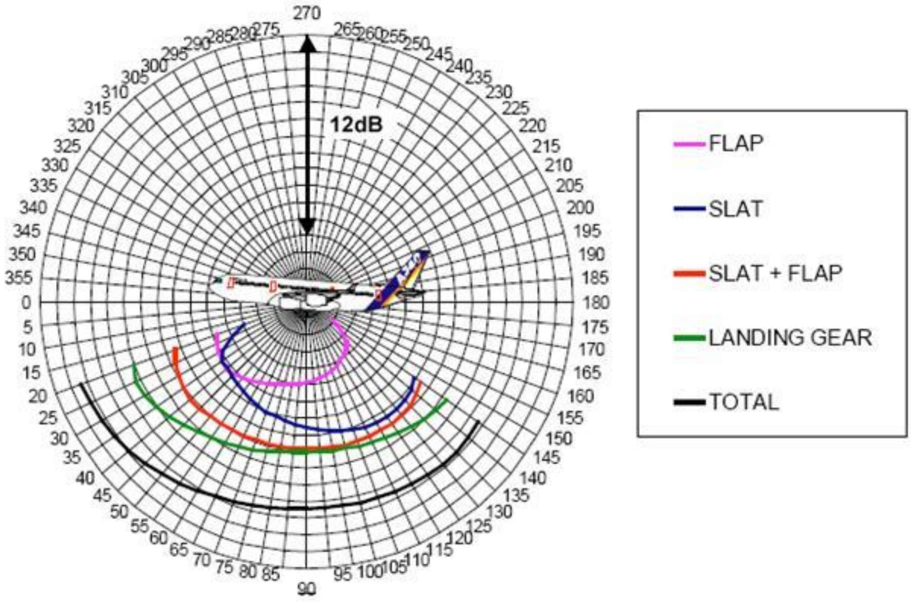

Figure 1.1: A340 aerodynamic noise sources directivity OASPL level[22].

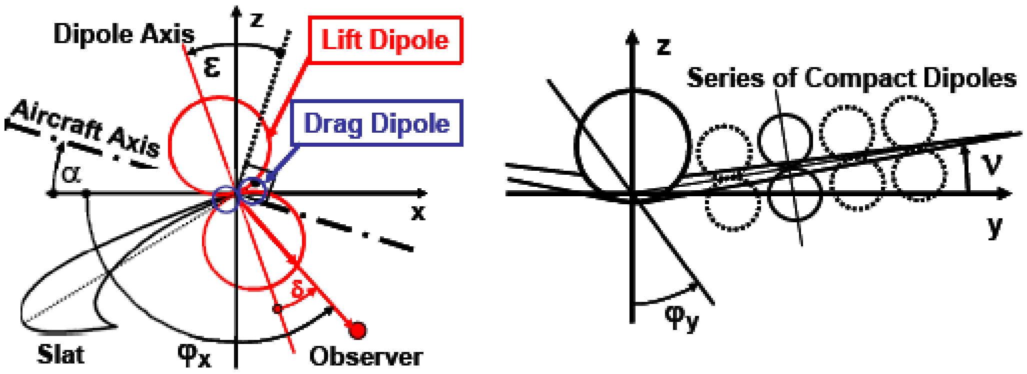

Figure 1.2: Simplified dipole model for slat trailing edge noise radiation[39].

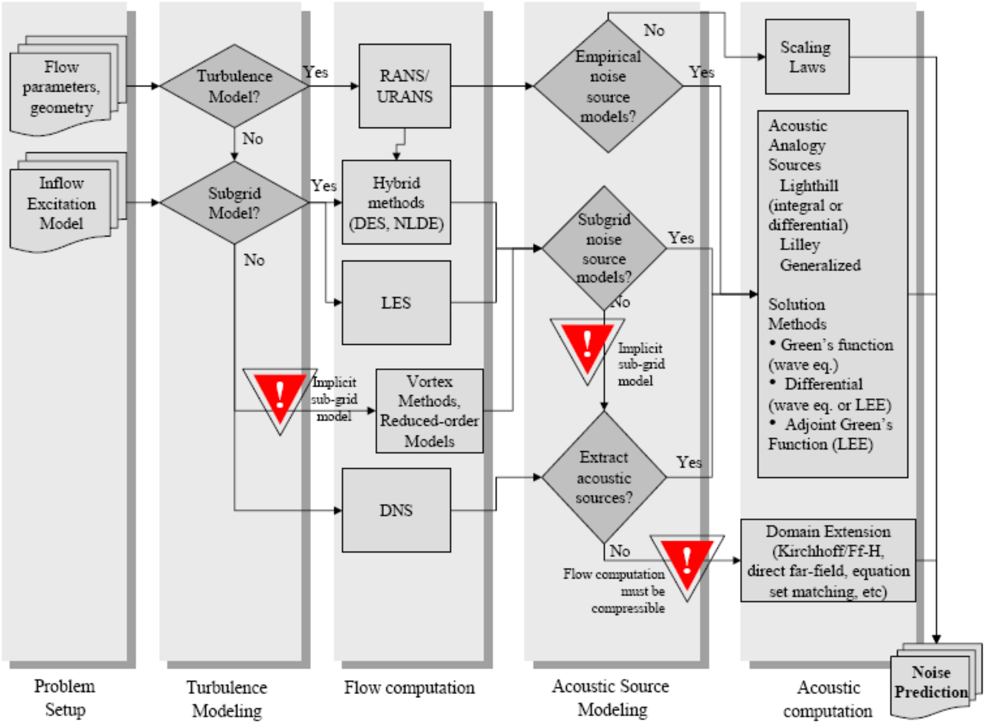

Figure 1.3: A hierarchy of noise prediction methods[47].

Chapter 2

Identification of Slat Noise

2.1 Introduction

As discussed in Chapter 1, slat noise represents a complex aeroacoustic problem and the underlying mechanisms have received extensive exploration over the past decades. It is generally agreed that the slat noise is broadband in nature, with highest levels appearing at a *St* number around 2 (based on the slat chord) and, in some cases, superimposed by tonal components[21, 23, 25]. However these tonal features are likely to be related to scaled wind tunnel experiments and have not yet been found to be present in full scale tests[25]. Three possible sources of tonal noise generation have been identified. The first is related to the coherent vortex shedding off a blunt slat trailing edge. This occurs on the scaled model when the relative trailing edge thickness (the thickness of the slat trailing edge compared with the slat chord) is high. The other tones occur at low *Re* numbers. One is linked with laminar flow separation at the slat cusp. The other results from the Tollmien–Schlichting boundary layer instabilities on the slat suction surface[25]. As for the broadband noise generation, several models have been proposed in the past. Molin and Roger[29] attributed the broadband component to an interaction between turbulent structures in the slat cove region and the leading edge of the main element. Dobrzynski and Pott-Pollenske[21] stated that the slat noise was produced by an interaction between the vorticity generated in the slat cove and the slat trailing edge. However, a more generally acknowledged view regarding slat noise generation is that the impingement of the free shear layer originating from the slat cusp on to the cove surface leads to intensive noise production[25, 29, 60]. A slat noise spectrum can be scaled by the corresponding freestream velocity. Andreou *et al.*[61] gave a u_∞^5 scaling law at frequencies below 25 kHz, and then u_∞^8 above the frequency. A similar scaling law was proposed by Guo and Joshi[6], in which a u_∞^5 scaling law for low frequencies was proposed, however at higher frequencies this changed to u_∞^6. The slat noise level is closely correlated to the AOA; in a range of AOA from low to moderate values (typical for landing conditions), the noise level increases as the AOA decreases. In addition, the slat noise directivity shows at maximum in the rear arc direction[25].

In this chapter, the slat noise levels obtained from both near- and far-field measurements, using an on-surface microphone and a phased microphone array respectively, are presented. The velocity field in the vicinity of the slat, acquired using a PIV system, is also presented. Furthermore, the velocity fluctuations in the slat gap region are examined using hot-wire anemometry. A discussion on the dynamic processes which present in the flow field around the slat, obtained from the fast PIV measurements, is also included. Lastly, numerical simulation results, performed to reveal the mechanism of the slat noise generation, are also discussed.

2.2 Setup

2.2.1 Setup for the Experiment

Wind tunnel model

The profile of the two-dimensional airfoil model was that of the EUROPIV 1[62]. The model consisted of two elements; a slat and a main element. As shown in Figure 2.1, the deflection angle of the slat (δ_s) was set to 30 degrees. The horizontal gap (o_s) and vertical overlap (g_s) were -2.4% and 2.7% of the chord in the stowed configuration respectively. The chord of the main element (c_m) was 350 mm, and 88 mm for the slat (c_s). The model had a span of 500 mm. The same geometric size was used for the numerical simulation. Pivots were inserted at either end of the model and allowed the angle of attack to be altered from 0 to 16 degrees in increments of 2 degrees. A zigzag tape with a thickness of 0.5 mm was mounted onto the surface near the slat cusp to trip the flow in all the experiments, with the exception of the experiment discussed in Chapter 5 wherein the slat noise was attenuated using a plasma actuator. A transparent board, which permitted PIV measurements, was used to link the slat and the main element. The freestream velocity in the experiment was set to 25 m/s (due to the limitation of the wind tunnel's maximum velocity). This corresponded to a *Re* number of approximately 5.7×10^5 (based on c_m).

Wind tunnels

The experiments were conducted in the 0.9 m × 0.6 m wind tunnel at the University of Southampton. The wind tunnel is a closed working section, open loop circuit design. The cross section measures 0.9 m (width) × 0.6 m (height) and the length of the working section measures approximately 4 m. The attainable maximum flow velocity in the working section is approximately 30 m/s and the intensity of the freestream turbulence (FST) is less than 1%. A thermometer and barometer permitted the temperature and atmospheric pressure to be measured at every experimental run. A Pitot tube, located 0.5 m behind the inlet of the test section, was employed to measure the freestream velocity. The flow visualization portion of the study was performed in the Plasma low speed wind tunnel at the University of Southampton. The tunnel has an open jet nozzle with a width of 350 mm and a height of 250 mm. The maximum wind velocity is approximately 18 m/s.

Instruments

PIV: PIV is an optical method of fluid visualization. It is used to measure instantaneous velocities and related properties in fluids. The fluid is seeded with tracer particles which, for the purposes of the PIV, are generally assumed to faithfully follow the flow motion. It is the motion of these seeded particles that is used to calculate the velocity information of the flow being studied. In this study, a TSI PIV system was employed to acquire instantaneous velocity around the slat. The PIV system consists of a camera and a CCD (Make: Camera 630059 Powerview 4M Plus) which provides a view field of 2048×2048 pixels, together with a Laser YAG New Wave pulse laser which generates the laser sheet. The system was operated at 2 Hz throughout the whole experiment. The post-processing of the PIV data involved a cross-correlation with a 16 × 16 pixel window, filtering and validation. The final results had a spatial resolution of 0.81 mm over a field of 130 mm × 90 mm.

A fast camera system (LaVision Highspeedstar6) was also employed to visualize the flow field in the vicinity of the slat. The fast PIV can collect images at 5000 frames per second. Using the provided software, the collected images were transformed into videos which were useful for observing the dynamics of the flow field.

On-surface microphone: A Bruel & Kjaer 4948 microphone was employed to measure the acoustic level in the near-field. The microphone has a sensitivity of 1.33 mV/Pa, a frequency range of 5 Hz to 10 kHz, and a dynamic range of 55 to 160 dB. Figure 2.2 shows the hardware by which the noise signals were collected and processed. The slat noise was first sensed by the microphone at a sampling rate of 30 kHz and a sampling time of 16 s. Next, the collected signals were pre-amplified and filtered before being converted to digital signals by a dSPACE A/D converter. The stop frequency of the low pass filter was set to 9.5 kHz. Finally, the acoustic signals were post-processed.

However, a potential issue can arise when performing near-field microphone measurements, wherein the microphone is unable to discern the acoustic pressure from the aerodynamic pressure associated with the boundary layer turbulence. In addition, the aerodynamic pressure is generally much higher than the acoustic pressure. This could result in measurement errors, and the microphone itself could be damaged if the aerodynamic pressure overly exceeds the dynamic range of the microphone. To avoid this issue, the microphone was mounted and recessed 5 mm from the cove surface and covered with a piece of sponge of 3 mm thickness (shown in Figure 2.3b). To verify whether the configuration of the microphone was detrimental to the acoustic measurements, three cases were tested:

- Microphone on surface without sponge cover;
- Microphone in cavity without sponge cover;
- Microphone in cavity with sponge cover.

As shown in Figure 2.3b, a white noise generator was placed on the slat suction surface side approximately 1.5 m away from the slat model. In all three cases, the noise generator produced the same noise levels. Figure 2.4 shows the comparison of noise spectra with a frequency resolution of 7.5 Hz of the three cases. Only slight deviations can be observed between the spectra. However it is noticeable that the spectra do not feature a full white-noise spectrum in the presence of the slat model (a white-noise spectrum should have an identical level throughout the entire frequency range). The magnitudes of the spectra notably depend on the frequency, e.g., the magnitude at $f = 2$ kHz is 23 dB higher than that at $f = 2.5$ kHz. This means that the slat geometry is an effective factor which determines the spectrum feature of the slat noise. Therefore, when investigating slat noise not only are the individual slat noise sources important, but the noise propagation in the presence of the slat geometry is also of note.

Hot-wire anemometer: A hot-wire anemometer (Make: Mini CTA 54T30, Dantec) was used to measure the velocity fluctuations in the slat gap region. The working principle for a hot-wire anemometer is based on the cooling effect of a flow on a heated body. The anemometer measures velocity at a point and provides continuous velocity time series, which can be processed into amplitude and time-domain statistics. Examples are mean velocity, turbulence intensity, higher order moments, auto-correlations and power spectra. In this experiments, the hot-wire anemometer was first calibrated prior to conducting measurement. A power law between the freestream velocity and the probe bridge voltage was used. It is well know that change in ambient temperature can result in a significant error in the velocity measurement. That is 1 °c change of the ambient temperature can give an error of approximate 2% in velocity. The error was corrected using the ratio between the over-temperatures during calibration and measurement. The flow velocity range in the calibration falls within 5 m/s to 32 m/s with an increment of 3m/s. The seven-time's calibration provided an accuracy of 0.1 m/s. In the experiment, the sampling rate was set at 30 kHz and the sampling time was 16 s. The data were segmented into 120 blocks with 4096 samples in each block. This provided a frequency resolution of 7.5 Hz.

Phased microphone array: A 49-channel phased microphone array with an aperture of 0.6 m was employed to locate the slat noise sources. The array was designed according to the principle of a multi-arm logarithmic spiral and the vector spacing between any two microphones was not repeated. The major sources of error in microphone array measurements are:

a) Electret microphones: the frequency response of microphones varies from one sample to another. A white noise generator and a B & K low noise microphone (make: 4179) were used. A frequency response calibration was conducted prior to the experiment, wherein the noise generator was a white noise generator and the reference microphone was a B& K 4179 microphone.

b) Free-space Green's functions: in the beamforming theory of microphone array, a free-space Green’s function was always assumed. This is an inaccurate assumption, especially for small, hard-walled wind tunnel sections, for example, the 0.9 m × 0.6 m wind tunnel. However, according to the measurements in the experiment, it was found that the boundary turbulence leaded to the main error. The measurements became acceptable after treatment of the microphone array. This will be discussed later.

c) Coherent sources: the beamforming theory assumes a point source at the focus point, in the absence of any other interfering sources. In practice there is usually a distribution of sources with some degree of coherency between them. This error will mostly influence quantitative values.

To avoid the negative effect caused by the boundary layer turbulence generated above the side wall of the wind tunnel, the array was recessed about 10 mm behind a stretched light fabric. To improve the clarity of the slat noise sources, several optimization techniques were used in the data post-processing, including subtraction of background noise and removal of the leading diagonal of the cross-spectral power matrix. The acoustic signals were acquired at a sampling rate of 48 kHz. For each experimental run, the signal consisted of 128 blocks with 4096 samples in each block. It provided a frequency resolution of 11.7 Hz. The phased microphone array was mounted in parallel to the axis of the wind tunnel and was flush mounted to the side wall of the wind tunnel. The distance between the centres of the phased microphone array and the experimental model was 0.4 m.

2.2.2 Setup for Numerical Simulation

In this study, delayed detached eddy simulation (DDES) was performed[63]. The DDES model employed an unsteady RANS one-equation turbulence model in regions close to a solid boundary, and LES in massively separated regions away from the solid boundaries. Figure 2.5 shows the grids around the slat. The computational domain extended from $-10c_m$ to $10c_m$ in both the x and y directions. Because it is not yet fully understood how the spanwise extension affects the computed output, various extensions have been used in several articles. For example, Deck used an extension of $25\%c_s$ in the spanwise direction[64], as did Choudhari and Khorrami 37.3%[65] and Imamura *et al.* 34.1%[35]. Lockard and Choudhari suggested that the near field fluctuations had a spanwise coherence length in the order of $10\%c_s$[66]. In this study, an extension of $41\%c_s$ and 37 grid points were used in the spanwise direction. The grid consisted of 71 blocks and a total of 130,000 grid points at a two-dimensional mid-span plane, and a total of 5×10^6 points in the entire three-dimensional domain. The first point off the solid surfaces was at approximately $y^+ \approx 1$.

A commercial code, FLUENT, was used in the study. An incompressible pressure based solver was employed to discretize the continuity, momentum and scalar transport equations. The temporal discretization employed a second-order scheme. All the solid surfaces were imposed as no-slip boundary conditions. Periodic boundary conditions were employed across the spanwise boundaries of the computational domain. A turbulence viscosity ratio of 2 was set as the velocity inlet condition. A dual time-stepping algorithm was used with 20 subiterations within each time step of 10^{-5} s, corresponding to a 7.14×10^{-4} flow time unit (time non-dimensionalized by c_m/u_∞).

The simulation procedure included three steps. Firstly, a steady simulation was performed to obtain a primary flow field, followed by an unsteady simulation. After the monitored drag force turned to be statistically stable, the primitive variables (i.e., velocities and pressure) were recorded at the end of every time step. A total of 16384 samples were collected, which correspond to approximately 12 flow time units.

The far-field noise was calculated using FW-H equations. The integration surfaces, over which the FW-H equations were employed, are shown in Figure 2.6. The choice of the integration surfaces was similar to that used by Casper *et al.*[67]. In the figure, the black solid line represents the slat surface whilst the blue solid and blue dotted lines represent the integration surfaces. The lines followed the grid lines of the CFD computation. The integration surfaces were segmented into two portions. It was surmised prior to the start of the computation that the flow in the wake of the slat gap contained intense vortical structures, which might result in errors in the calculation of the slat noise when the FW-H equations were performed. The contributions of these two separated portions to the overall slat noise will be compared later.

2.2.3 Signal Post-Processing

In this research, the data post-processing of the experimentally measured and computed signals involved the following techniques.

DFT: The Discrete Fast Fourier Transform (FFT) transforms a signal from the time domain into the frequency domain. If x_0, $x_1, \ldots, x_N$ denotes a discrete serial signal, with N representing the sample size, the DFT is expressed as

$$X_k = \sum_{n=0}^{N-1} x_n \, e^{-i2\pi k\frac{n}{N}} \qquad k = 0, 1, \cdots, N-1 \tag{2.1}$$

Cross-correlation: Cross-correlation can be used to find the correlating level between two signals and the corresponding lag time. The cross-correlation between two discrete signals $f(t)$ and $g(t)$ is

$$(f \times g)_n = \sum_{m=-\infty}^{+\infty} f_m{}^{*} g_{n+m} \tag{2.2}$$

Power spectral density (PSD): The PSD describes how the 'energy' of a signal is distributed with frequency. For a discrete signal *f*(*t*), the definition of the PSD is

$$S(\omega) = \left| \frac{1}{\sqrt{2\pi}} \sum_{n=-\infty}^{+\infty} f_n e^{-i\omega\frac{n}{N}} \right|^2 = \frac{F(\omega)F^*(\omega)}{2\pi} \tag{2.3}$$

where $F(\omega)$ is the Fourier transform of the signal *f*(*t*).

Filter: A filter function lets the signal within a certain range of frequency pass and the signal outside of the range is suppressed. It can be categorized into low-pass, high-pass and band-pass filter. In mathematics, the output *y*(*k*) of a digital filter is related to the input *x*(*k*) by convolution with impulse response *h*(*k*) of the filter. If *X*(*z*), *Y* (*z*) and *H(z)* denote the Z-transform of the *x*(*k*), *y*(*k*) and *h*(*k*) respectively, the filter can be written as

$$Y(z) = H(z)X(z) \tag{2.4}$$

with

$$H(z) = \frac{b_0 + b_1 z^{-1} + b_2 z^{-2} + \cdots + b_N z^{-N}}{a_0 + a_1 z^{-1} + a_2 z^{-2} + \cdots + a_M z^{-M}} \tag{2.5}$$

where the coefficients, a_k, are the 'feed-backward' coefficients and, *bk*, are the 'feed-forward' coefficients. The resultant linear difference equation is

$$y_n = -\sum_{k=1}^{N} a_k \, y_{n-k} + \sum_{k=1}^{M} b_k \, x_{n-k} \tag{2.6}$$

Several techniques can be employed to calculate the coefficients, a_k and b_k, e.g., Butterworth, Chebyshev Type I, Elliptic. In this research, all the above post-processing programmes were coded using Matlab.

To investigate and identify the slat noise, both experiments and numerical simulations were performed. The experimental matrix is shown in Table 2.1. Table 2.2 lists the primitive variables which were recorded during the numerical simulation and the corresponding post-processed variables, which were calculated based on the primitive variables. The post-processed variables were compared amongst various AOAs to reveal the features and mechanism of the slat noise.

2.3 Results and Discussions

2.3.1 Mean Aerodynamic Features

Lift coefficient with AOA

Figure 2.7 shows the computed lift coefficients at several AOAs. The lift coefficient is defined as

$$C_l = L/q_\infty A \tag{2.7}$$

where L is the lift force of the wing and q_∞ and A are the dynamic pressure of the freestream and wing area respectively. A near linear increase in C_l with the AOA is seen between 6 to 10 degrees, and the slope of the coefficient is approximately 0.26 per degree. The coefficient achieves the highest value of 2.7 at approximately AOA = 13.5 degrees. The relationship between the lift coefficient and the AOA is in accordance with that of the general wing, although no experimental results are available to be compared with the computed results.

Mean velocity field at various AOAs

Figure 2.8 shows the computed mean flow fields around the slat at AOA = 6, 8 and 12 degrees. Several features can be observed. Firstly, the size of the circulation region is represented by the distance from the leading edge of the slat to the vertex of the circulation region (shown in Figure 2.8). It can be seen that the sizes are 1.01, 0.935 and 0.825cs at AOA = 6, 8 and 12 degrees respectively. The size decreases as the AOA increases. This agrees with the results obtained by Dobrzynski *et al.*[68]. Secondly, a virtual cusp flow channel is defined. This is the channel formed by two streamlines, one of which passes close to the slat cusp, the other passes close to the leading edge of the main element. The width of the channel is defined as the distance from the slat cusp to the streamline which passes closest to the leading edge of the main element (shown in Figure 2.8). The widths are 0.09, 0.13 and 0.17cs at AOA = 6, 8 and 12 degrees respectively. The width becomes larger as the AOA increases. The velocity in the slat gap can be estimated to increase with the AOA because the width of the channel at the slat gap is fixed, whilst the width at the slat cusp is increased with the increasing AOA. Provided that the mean flow velocity at the slat cusp is not changed, the mean velocity at the slat gap must increase with the AOA according to the mass conservation law. Thirdly, the static pressure near the leading edge of the main element decreases as the AOA increases. Finally, the streamline which passes closest to the slat cusp at AOA = 6 degrees is significantly different from those at other AOAs. At AOA = 6 the streamline passes through the slat gap without impingement on the slat cove surface, whilst at different AOAs it convects into the circulation region after impingement on the slat cove surface. According to the mean flow field, it is found that the size of the circulation region, the mean velocity in the slat gap region, and the width of the cusp flow channel have a close relationship. It will be seen that the size of the circulation region has an important effect on the slat noise generation.

Mean flow features at various freestream velocities

Figure 2.9 shows the computed mean flow field around the slat at AOA = 8 degrees and a freestream velocity of 70 m/s. The size of the circulation region and the channel width are nearly the same to those at AOA = 8 degrees and a freestream velocity of 25 m/s. Figure 2.10 shows the computed mean velocities and static pressures along the gap line (this is the line which links the trailing edge of the slat with the leading edge of the main element) at freestream velocities of 25, 40, 55 and 70 m/s. It can be seen that the non-dimensionalized mean velocities and static pressures along the line are nearly identical. This means that the mean flow features are weakly dependent on the freestream velocity.

2.3.2 Relationship between Slat Noise Level and Angle of Attack

Effect of distance on slat noise level

The acoustic pressures in the far-field were calculated using FW-H equations, and the corresponding integration surfaces are shown in Figure 2.6 (represented by both solid and dotted blue lines). The observation distance between the leading edge of the main element and the observer, r, was changeable but the observation angle was kept at 280 degrees. Figure 2.11 illustrates the relationship between the root mean square (RMS) of acoustic pressure with the observation distance. The pressure drops dramatically with r shorter than $100c_s$, followed by a gradual decrease. This agrees with the $1/r$ law. Figure 2.12 shows the comparison of sound pressure levels (SPL) which were calculated at four observation distances. The discrepancy is negligible if the *St* number is less than 5. Above this *St* number, the discrepancy tends to be augmented. The SPLs corresponding to the shorter distances (11 and $28c_s$) are obviously lower than those corresponding to the longer distances (102 and $738c_s$) during the high *St* number range. However the discrepancy corresponding to 102 and $738c_s$ is negligible throughout the entire range. Therefore, in this study, only when the observation distance is longer than $102c_s$ can the condition of the acoustic far-field be satisfied. At a distance of $102c_s$, the ratio between the observation distance and the wavelengths corresponding to a 1 kHz sound wave is approximately 26. In the following results, when the SPL of the slat noise is presented it corresponds to the longest distance of $738c_s$.

Effects of the integration surface

The choice of the integration surface has a significant effect on the predicted acoustic pressure when using the FW-H equation. Khorrami *et al.*[69] compared the acoustic pressures of a high-lift device (HLD) with three types of integration surfaces: a) on-body surfaces; b) surfaces extended outside the boundary layer of the slat suction surface and encompassing the slat cove region; and c) surfaces composed of the slat suction surface and encompassing the slat cove region. The results indicated that a significant difference occurred amongst the computed acoustic pressures during a frequency range from 4 to 10 kHz. Casper *et al.*[67] suggested that there was a potential for erroneous noise sources to be generated as vortices in the wake passing through the integration surface. In addition, the contribution of volumetric noise sources (quadrupole-like noise) to the total noise is not negligible in high lift simulations. In this study, the flow passing through the slat gap was suspected to contain intense vortices. Therefore errors may have arisen in the calculation of the slat noise using an integration surface traversing through the wake of the slat gap. To understand this issue, the integration surface was segmented into two portions (shown in Figure 2.6). The noise contributions from the two portions were calculated respectively and compared. Figure 2.13 shows the directivity comparison. The acoustic pressure predicted over the surface S2 (shown in Figure 2.6) is obviously higher than that predicted over surface S1 throughout the entire observation angle range, especially at the observation angle of 60 and 240 degrees. In addition, the observation angles at which the acoustic pressures achieve the maxima are also different: for the surface S1, the two observation angles are approximately 120 and 300 degrees, while for S2, they are approximately 105 and 285 degrees. Figure 2.14 shows the comparison of the 1/3 octave SPLs computed over the surfaces of S1 and S2 at an observation angle of 280 degrees. The SPL corresponding to surface S2 is slightly higher throughout the entire frequency range. This is a reasonable result because this surface (represented by the dotted blue line in Figure 2.6) also contributes a fraction to the noise in the far-field. According to the results, it cannot be concluded that obvious errors have resulted from the integration surface passing through the wake of the slat gap because the SPLs associated with S2 are not excessively higher than those associated with S1. In addition, the frequency-dependant features of the two SPLs are similar. Therefore, in the following section, the surface S2 was chosen as the integration surface when the slat noise in the far-field was predicted.

Sealed slat gap

A test was performed in the 0.9 m × 0.6 m wind tunnel where the slat gap was sealed by a piece of sponge. This meant no flow passed through the slat gap. The near-field noise was measured using the on-surface microphone. Figure 2.15 shows the comparison of the 1/3 octave SPLs between the slat gap, sealed or not. The SPL corresponding to the sealed gap is significantly lower throughout the entire frequency range. Two conclusions can be derived from this comparison. The first is that the slat gap flow dominates the generation of the slat noise, because the noise level is remarkably low when no flow convects through the gap. The second is that the slat noise can be properly measured using the on-surface microphone in the presence of the background noise of the wind tunnel. Because the background noise level remained unchanged regardless of whether the gap was sealed or not, the fact that when the slat noise with a sealed gap was sufficiently low showed that the slat noise with a normal gap was sufficiently high to be measured properly.

Relationship between SPL of slat noise with AOA

As mentioned in Chapter 1, the relationship between the slat noise level and the AOA is complex. However, within a certain range of AOA, the slat noise level was found to decrease as the AOA increased. In this study, the slat noise was measured in the 0.9 m × 0.6 m wind tunnel using an on-surface microphone at various AOAs and u_∞ = 25 m/s. Figure 2.16 shows the relationship between the 1/3 octave SPL and the AOA. Firstly, the spectrum at AOA = 4 degrees is obviously different with those at other AOAs; the SPL at frequencies lower than 3 kHz is significantly low, and the frequency-dependent SPL appears differently than those at other AOAs. Secondly as the AOA is altered from 6 to 8 degrees, the SPL increases significantly, achieving the maximum at AOA = 8 degrees. Finally, the SPL gradually drops as the AOA is changed from 8 to 16 degrees. This result is in accordance with the conclusion given by Choudhari *et al.*[70], who stated that the noise levels decreased when the AOA increased, within a range of low and moderate AOAs. To verify whether the slat noise in the far-field had a similar AOA-dependent feature, the far-field noise was measured using a 49 channel phased microphone array. In the measurements, the distance from the leading edge of the main element to the centre of the microphone array was 0.4 m, which corresponded to 2.4 wavelengths for a sound wave with a frequency of 2 kHz. Figure 2.17 shows the measurements at AOA = 6, 8, and 10 degrees and the 1/3 octave frequencies f = 1.6, 2.5 and 4 kHz. The noise levels at AOA = 8 degrees are the highest, followed by those at AOA = 10 degrees. At AOA = 6 degrees, the noise levels are at their lowest. This agrees well with the near-field noise measurements. Meanwhile, it can be observed from the array measurements that intense noise is generated in the slat gap region. Figure 2.18 shows the comparison of the computed slat noise level in the far-field. The AOA-dependent feature of the slat noise is in accordance with the experimental measurements. The mechanism which governs the relationship between the slat noise level and the AOA is the focus of the following sections.

2.3.3 Location of Noise Sources

Turbulence kinetic energy

The TKE is defined as

$$\text{TKE} = \frac{1}{2}\sum_{i=1}^{3}\overline{u_i'^2}\,, \qquad u_i' = u_i - \overline{u_i} \tag{2.8}$$

Several studies have linked slat noise sources with the TKE values around a slat. For instance, Ewet and Emunds[48] claimed that the TKE had a close relationship with the noise source. For isotropic turbulence, the Lilley formula[71] can be written as

$$I_A = \alpha_k \rho_0 \varepsilon M_t^5 \tag{2.9}$$

where I_A is acoustic power, α_k is a constant and can be set to 0.1[72], ε is the turbulence dissipation rate and

$$M_t = \frac{\sqrt{2\text{TKE}}}{a_0} \tag{2.10}$$

According to Equation (2.9), acoustic power due to the unit volume of isotropic turbulence is directly related to the TKE value. Meanwhile, the simplified Lighthill's turbulence stress tensor shows that the TKE can be linked with the noise source. At high *Re* numbers, the Reynolds stress term $\rho u_i u_j$ is much larger than the viscous stress term e_{ij}, hence the e_{ij} can be negligible. Meanwhile, at low *Ma* numbers, the flow around the slat can be regarded as isentropic flow, hence

$$p - p_0 \approx c_0^2(\rho - \rho_0) \tag{2.11}$$

Therefore, the Lighthill's stress tensor can be approximated as $T_{ij} \approx \rho_0 u_i u_j$. By comparing the simplified Lighthill's stress tensor with the definition of the TKE, it is seen that the TKE is closely related with the simplified Lighthill's stress tensor. Figure 2.19 shows the computed TKE distributions in the vicinity of the slat at AOA = 8 and 12 degrees respectively. Large TKE values appear along the shear layer originating from the slat cusp and in the wake of the slat gap. However, the highest values appear inside the reattachment region at both AOA = 8 and 12 degrees (in this study the reattachment region is referred to as the region where the shear layer approaches the cove surface). Similar TKE distribution patterns have been observed in research by Imamura *et al.*[24] and Choudhari *et al.*[23]. According to the TKE distribution, the flow in the reattachment region can be regarded as the dominant noise source. By comparing the two TKE distributions at AOA = 8 and 12 degrees, it is observed that the former is higher than the latter in the reattachment region and in the wake of the slat gap. If the slat noise in the far-field arises from the TKE in the reattachment region, the TKE distributions can explain why the noise level at AOA = 8 degrees is higher than that at AOA = 12 degrees.

Vorticity

Several publications[60, 66, 69-70] have described the vorticity behaviour around a slat, which was generally regarded as an indication of the slat noise sources. Figure 2.20 shows the computed mean of the absolute value of the vorticity in the spanwise direction around the slat at AOA = 8 and 12 degrees. The mean of the absolute value of the vorticity is defined as

$$\overline{|\omega_z|} = \frac{1}{N}\sum_{i=1}^{N}|\omega_{z_i}|, N = 600 \tag{2.12}$$

where *N* is the number of the profile data at the mid-span plane. A total of 600 such profile data were acquired during the processing of the numerical simulation. The employment of $\overline{|\omega_z|}$, rather than instantaneous ω_z, tends to obtain statistically reliable distributions of ω_z. According to the results, the highest $\overline{|\omega_z|}$ value occurs in the reattachment region. High $\overline{|\omega_z|}$ values are observed in the wake of the slat gap and the slat cusp as well. Comparing $\overline{|\omega_z|}$ at AOA = 8 and 12 degrees, the values of $\overline{|\omega_z|}$ in the reattachment region at AOA = 8 degrees is significantly higher than those at AOA = 12 degrees. Generally, the distribution of $\overline{|\omega_z|}$ is similar to the distribution of TKE around the slat, wherein large values of both $\overline{|\omega_z|}$ and TKE occur in the same region.

Lamb vector

The Powell formula[10] can be employed to find the noise sources around the slat

$$\frac{1}{c_0^2}\frac{D^2B'}{Dt^2} - \nabla^2 B' = \nabla \cdot L, \qquad L = \omega \times v \tag{2.13}$$

with

$$B = i + \frac{1}{2}v^2, B' = i' + v_0 v', i' = \frac{p'}{\rho_0} \tag{2.14}$$

where *i* is the specific enthalpy and *B* is the total specific enthalpy. At low *Ma* numbers, the Powell's approximation is,

$$\frac{1}{a_0^2}\frac{\partial^2 p'}{\partial t^2} - \nabla^2 p' = \rho_0 \nabla \cdot L \qquad (2.15)$$

Equation (2.15) explicitly states that the $\nabla \cdot L$ acts as a noise source. Figure 2.21 shows a computed instantaneous $\nabla \cdot L$ value distribution around the slat. High values of $\nabla \cdot L$ appear near all solid surfaces. This results from the fact that large velocity gradients are generated due to boundary layer flow close to the solid surfaces. Meanwhile, high values of $\nabla \cdot L$ also appear in the wakes of the slat cusp and the slat trailing edge. An important feature of $\nabla \cdot L$ distribution is that the high values behind the slat cusp merely propagate a short distance and then decline sharply. However, in region C (shown in Figure 2.21), high values of $\nabla \cdot L$ are re-generated. This means that the high values of $\nabla \cdot L$ in region C are not the succession of the shear layer, but regenerated by means of a mechanism which is discussed later. Figure 2.22 shows the comparison of the computed means of the absolute value of $\nabla \cdot L$ at AOA = 8 and 12 degrees. The mean of the absolute value of $\nabla \cdot L$ is defined as

$$\overline{|\nabla \cdot L|} = \frac{1}{N}\sum_{i=1}^{N} |\nabla \cdot L_i|, \qquad N = 600 \qquad (2.16)$$

where N is the number of the profile data at the mid-spanwise plane, N = 600 in this research. The distributions of the $\nabla \cdot L$ at both AOA = 8 and 12 degrees suggest that the slat gap region is a main noise source, in addition to the wakes of the slat cusp and the trailing edge of the slat. Meanwhile, high values are observed in the region C (shown in Figure 2.21). This is in accordance with the instantaneous $\nabla \cdot L$ distribution. Nonetheless, as shown in Figure 2.22, no obvious difference in the $\overline{|\nabla \cdot L|}$ distribution can be seen between AOA = 8 and 12 degrees. This results from the fact that the velocity in the gap region at AOA = 12 degrees is much higher than that at AOA = 8 degrees (the velocity in the gap region will be shown later), and the velocity is part of the calculation of $\nabla \cdot L$.

Pressure fluctuations

In Equations (1.7) and (2.15), the terms on the left hand are directly related to the pressure fluctuation. The pressure fluctuation is interpreted as acoustic pressure in the far-field and pressure fluctuation in the flow region[1]. This means that the pressure fluctuation in the flow region has a direct relationship with the acoustic pressure in the far-field. The study on slat noise by Yokokawa *et al.*[73] has shown that the pressure fluctuations in the slat gap region are closely linked with the noise in the far-field. In this study, the computed pressure fluctuation at the i^{th} time step in the mid-span plane is defined as

$$p_i' = p_i - \bar{p}, \qquad \bar{p} = \frac{\sum_{i=1}^{N} p_i}{N} \tag{2.17}$$

where N is the number of the data frames, here N = 600. Figure 2.23 shows a computed instantaneous pressure fluctuation distribution around the slat. The fluctuating pressures near the trailing edge of the slat and the leading edge of the main element achieve high values. This is in accordance with the results obtained by Choudhari and Khorrami[65], who found that the peak pressure fluctuations along the main element surface were concentrated within the leading edge region, but the amplitudes of those fluctuations were weaker than the pressure fluctuations near the reattachment location. Figure 2.24 shows the comparison of the RMS of pressure fluctuations at AOA = 8 and 12 degrees. It is clear that the fluctuations near the leading edge of the main element at AOA = 12 degrees are weaker than those observed at AOA = 8 degrees. Meanwhile the geometric size of the region, in which intense fluctuations occur, is larger at AOA = 8 degrees than that at AOA = 12 degrees. By comparing the pressure fluctuations it can be clearly understood that the slat noise sources at AOA = 8 degrees dominate over those at AOA = 12 degrees. Figure 2.25 shows the RMS of pressure fluctuations in a wide domain. High RMS values appear in the upward and downward direction, while low values appear in the forward and rear direction. This agrees with the directivity of the slat.

Several physical variables, including TKE, $\overline{|\omega_z|}$, $\overline{|\nabla \cdot L|}$ and p'_{rms}, are employed to locate the noise sources of the slat. At AOA = 8 degrees, the locations of the noise sources addressed by those variables are slightly different than at AOA = 12 (shown in Table 2.3). Because the calculation of the variable $\nabla \cdot L$ involves the velocity gradient, excessively high values of $\nabla \cdot L$ appear in the regions close to the solid surfaces and in the wakes. Meanwhile, due to the fact that the flow velocity in the gap region at AOA = 12 is much higher than that at AOA = 8 degrees, it is difficult to tell the intensity of the $\overline{|\nabla \cdot L|}$ values distribution between an AOA = 8 and 12 degrees. The variables TKE and ω_z have a similar value distribution around the slat, both indicate the reattachment region is a dominant noise source. However, the variable p'_{rms} indicates that both the reattachment region and the region near the leading edge of the main element are the dominant noise sources. The variable p'_{rms} is the preferred choice when locating the noise sources because it has a direct relationship with the acoustic pressure in the far-field. However, experimental measurement of the variable p' in a flow field is difficult to perform because no appropriate instrument can be employed, whilst the velocity can easily be measured by PIV and the variables TKE, ω_z and $\nabla \cdot L$ are all calculated based on the PIV measurements. Amongst the variables TKE, ω_z and $\nabla \cdot L$, the variable TKE is the most preferable when locating noise sources because it is a statistic value associated with fluctuating velocity and avoids the issue of mean velocity. It is known that sound is by nature comprised of pressure fluctuations and is not directly related to mean value. In the following section it will be shown that the velocity fluctuations in the slat gap region have a close relationship with the pressure fluctuations.

2.3.4 Discussion of the Slat Noise Mechanism

Relationship between shear layer and slat noise

Several studies[23, 29, 60] regarding the origins of slat broadband noise concluded that it originated from the shear layer shedding off the slat cusp. The process, in which the shear layer impinges on the cove surface and the subsequent distortion and stretching of the vortices, plays an important role in the slat broadband noise generation. However, it is also important to explain the AOA-dependent feature of the slat noise level. One possible explanation is as follows. The potential velocity near the slat cusp decreases as the AOA increases, hence the intensity of the vorticity in the wake of the slat cusp decreases, owing to the feature of flow instability. This leads to the decrease of the slat noise level. However the results obtained from the experiments conducted in the 0.9 m × 0.6 m wind tunnel at a freestream velocity of 25 m/s indicated that slat noise has only a weak relationship with the shear layer.

Figure 2.26 schematically shows the wind tunnel model. A piece of strip with a thickness of 1 or 2 mm and a width of 10 mm was mounted on the surface near the slat cusp. The inclusion of the strip altered the property of the shear layer. This was proven by results obtained from hot-wire anemometer measurements (not shown here). Figure 2.27 shows a comparison of the noise spectra at AOA = 8 degrees and u_∞ = 25 m/s with various strip thicknesses. The strip has a minor effect on the spectra. According to the results, it can be concluded that the slat noise is not closely associated with the shear layer and the shear layer itself is not a dominant noise source, because the alteration of the shear layer did not cause any significant change to the noise spectra. Dobrzynski[25] showed that only the low frequency tonal component could be attenuated or even eliminated through massive tripping at the slat cusp.

Velocity measurement and visualization of flow field around the slat using PIV

To gain an insight into the flow field around the slat, the velocity field around the slat was measured using the TSI PIV system. The measurements were conducted in the 0.9 m × 0.6 m wind tunnel. The AOA and freestream velocity were set to 8 degrees and 25 m/s respectively. Figure 2.28a shows a mean velocity field averaged over 200 velocity frames around the slat. A regular recirculation region appears in the slat cove. By contrast, the instantaneous velocity field (shown in Figure 2.28b) appears to be much more complex. Several vortical structures are present in the slat cove. By inspecting whole sequences of PIV images, it was found that the instantaneous velocity vectors in the slat cove varied significantly with time both in their direction and magnitude. Furthermore the vortical structures only appeared in a portion of the images. The flow in the slat cove presented a typical unsteady flow feature. Unfortunately, the PIV system could not be operated at a higher acquisition rate. To capture the dynamics of the flow field around the slat, a fast camera system (Make: LaVision Highspeedstar6) was employed. The experiment was conducted in the Plasma low speed wind tunnel at the University of Southampton. The AOA was set to 8 degrees and the freestream velocity was set to 15 m/s. The sampling rate was set to 5000 frames per second, and 500 images in total were captured over 0.1 s. A video was made using all the images in order to examine the dynamics of the flow. Observing the video, several crucial features were found. Firstly, similar to the velocity field shown in Figure 2.28b, the flow convected from the stagnation line of the main element intermittently altered its velocity magnitude and direction, and large scale vortical structures were intermittently generated in region C (shown in Figure 2.28b). The flow field around a slat was measured using PIV by Takeda *et al.*[74], who also found large vortical structures ejected through the slat gap. The computed distribution of $\nabla \cdot L$ values (shown in Figure 2.21) has also illustrated that high values behind the slat cusp merely propagate a short distance and then decline sharply, followed by high values of $\nabla \cdot L$ being regenerated in the region C. The large scale vortical structures are assumed to be resulting from the unsteady interaction between the shear layer and the flow convected from the stagnation line of the main element because the two flows join together in region C. Since the fluctuating components regenerated in the region C, rather than those contained in the shear layer, will be convected to the reattachment region and, consequently, the slat noise will be produced. It is suggested that this interaction, rather than the shear layer, is the origin of the slat noise generation. In this study, region C is named as the interaction region because of its important role in the slat noise generation. Secondly, the flow near the slat trailing edge changed its direction in a periodic fashion. Finally, the flow in the vicinity of the slat gap behaved as an oscillatory system. By counting the number of vortical structures that appeared in region C during the 0.1 s, the oscillation frequency was estimated to be approximately 60 Hz, which corresponds to a *St* number of 0.35 (based on the slat chord).

Mean and fluctuating velocity in the gap region

A hot-wire anemometer (Make: Mini CTA 54T30, Dantec) was used to measure the velocity fluctuations in the gap region at AOA = 8 degrees and a freestream velocity of u_∞ = 25 m/s. Figure 2.29 schematically shows the positions at which the velocities were measured by the hot-wire anemometer. The velocity fluctuation is defined as $u_i' = u_i - \bar{u}$, where u_i is the instantaneous velocity, and $\bar{u}$ is the mean velocity. The sampling rate was set to 30 kHz and the sampling time was 16 s. Figure 2.30 shows the velocity fluctuation spectra at the three positions. A peak clearly appears at f = 75 Hz, which corresponds to a *St* number of 0.264 (based on the slat chord). Although the value is slightly different to the one estimated from the flow visualization, both share the same feature of a low frequency phenomenon due to intermittently generated vortical structures identified in the flow visualization. McGinley *et al.*[75] also observed, using a hot-wire anemometer in the slat wake, that unsteady phenomena seen at low AOAs were not present at high AOAs.

Besides the measurements using the hot-wire anemometer, the velocity fluctuations in the gap region were studied using numerical simulations. Figure 2.31 shows the computed mean velocities at various AOAs, wherein 18 monitors with equal spacing were placed along the gap line (not including the positions on the solid surfaces). The time history of the velocities at those positions was recorded during the numerical simulation. Although differences occur between the experimental and computed results, the trends are similar. Several features can be observed according to the mean velocities:

a) At all AOAs, the mean velocity gradually increases along the gap line from the trailing edge of the slat to the leading edge of the main element. This results from the fact that the flow in the gap region represents a typical flow along a large curvature surface. As shown in Figure 2.32, a local coordinate system with the leading edge of the main element as the origin and the η axis along the gap line can be constructed. A control element at the gap line mainly experiences two kinds of force in the η direction, the eccentricity force and normal stress. Under these two forces, the control element is kept in equilibrium. This can be expressed as

$$-\frac{\partial p}{\partial \eta}+\rho\frac{v_\tau^2}{R+\eta}=0 \tag{2.18}$$

where R is the curvature radius at the leading edge of the main element. Assuming that the fluid on the η axis is convected from the far-field, and without energy dissipation along the flow path, the fluid contains the same total pressure

$$p+\frac{1}{2}\rho v_\tau^2=p_0 \tag{2.19}$$

Differentiating Equation (2.19) with respect to η gives

$$\frac{\partial p}{\partial \eta}=-\rho v_\tau\frac{\partial v_\tau}{\partial \eta} \tag{2.20}$$

Substituting Equation (2.20) into Equation (2.18) gives

$$v_\tau = \frac{C}{\eta + R} \tag{2.21}$$

where C is a constant, which is determined by the AOA. It can be seen that the velocity decreases with the coordinate η.This is in accordance with the experimental and computed results.

b) At the same coordinate, η, the velocity increases with the AOA. This relationship agrees with the previous statement associated with Figure 2.8. However, it can be seen that the velocity pattern at AOA = 6 degrees deviates significantly from those at other AOAs. It implies that the flow features in the gap region at AOA = 6 degrees are not similar to those at other AOAs. Regarding the mean flow field shown in Figure 2.8, it can be assumed that a typical recirculation region is not formed at AOA = 6 degrees.

c) The slat noise level is adversely proportional with the mean velocity at various AOAs except at AOA = 6 degrees. It has been shown that the noise levels decrease with increasing AOA and reach their highest level at AOA = 8 degrees.

Figure 2.33 shows the comparison of the computed RMS of velocity fluctuations along the gap line at various AOAs. The RMS values appear to be similar at AOA = 8, 10 and 12 degrees. An obviously different trend is seen at AOA = 6 degrees. This further indicates that the flow at AOA = 6 degrees varies significantly to those present at other AOAs. According to the results, the RMS values at AOA = 8 degrees achieve the highest, followed by the values at AOA = 10 and 12 degrees. It can be found that the slat noise levels are proportional to the RMS values, i.e. high RMS values correspond to a high noise level. The RMS values gradually increase from the leading edge of the main element to the trailing edge of the slat at all AOAs except at 6 degrees. Besides this, a peak appears at the 6th monitor at AOA = 8 degrees. No peak appears at any other AOA. It is suggested that the peak arises from the intermittent ejection of vortical structures originating from the slat cove at relatively low AOAs. This phenomenon agrees with the observation by Paschal *et al.*[76], who showed that the probability of the occurrence of the vortical structures in the slat cove was much greater at a low angle of attack (4 degrees) than that at a high angle (10 degrees).

Figure 2.34 shows the comparison of the computed RMS of pressure fluctuations along the gap line at various AOAs. The RMS values at AOA = 8 and 12 degrees share similar trends along the gap line, while those at AOA = 6 degrees present a significantly different trend. By comparing the value patterns between the RMS of pressure and velocity fluctuations, it is observed that the velocity fluctuations have high values near the trailing edge of the slat and low values near the leading edge of the main element, while the pressure fluctuations have a peak at the 5th monitor, which is close to the trailing edge of the slat, and high values also appear near the leading edge of the main element. The two RMS values present in a significantly different fashion. However, the relationship between the TKE values and the p'_{rms} values can be approximately estimated as follows. In Equation (2.19), let $p = \bar{p} + p'$, $v_\tau = \bar{v_\tau} + v_\tau{}'$, where the overbar denotes mean time and the prime represents a fluctuating component

$$(\bar{p} + p') + \frac{1}{2}\rho(\bar{v_\tau} + v_\tau{}')^2 = p_0 \tag{2.22}$$

because $\bar{p} + \frac{1}{2}\rho\bar{v_\tau}^2 = p_0$ and assuming $|\bar{v_\tau}v_\tau{}'| \gg v_\tau{}'^2$, we have

$$p' + \rho\bar{v_\tau}v_\tau{}' = 0 \tag{2.23}$$

substituting Equation (2.21) into Equation (2.23) gives

$$|p'| = \rho\frac{C}{R+\eta}|v_\tau{}'| \tag{2.24}$$

Since p' and $v_\tau{}'$ have zero mean values, the relationship between the RMS of velocity fluctuations and pressure fluctuations can be approximately written as

$$p'_{rms} = 2\rho\frac{C}{R+\eta}\mathrm{TKE} \tag{2.25}$$

Equation (2.25) can be used to partially explain the difference of the value patterns shown in Figures 2.33 and 2.34. In the region close to the leading edge of the main element, although the TKE value gradually decreases with η, the resulting p'_{rms} values estimated using Equation (2.25) increase with η due to the effect of η.

Although the freestream velocity has minor effects on the non-dimensionalized mean flow field (shown in Figure 2.9) or on the mean velocity and static pressure along the gap line (shown in Figure 2.10), it has obvious influences on the TKE values and p'_{rms}values. As shown in Figure 2.35, the non-dimensionalized TKE values are slightly altered, wherein the values close to the trailing edge of the slat decrease, while increasing at other positions. The reason for this is not fully understood, but is suspected to be linked with the production and dissipation of TKE at different *Re* numbers. The non-dimensionalized p'_{rms} are significantly affected by the velocity of the freestream (shown in Figure 3.36). It can be seen that the peaks at the 6th and 18th monitors are significantly higher. As discussed above, the peaks are assumed to link with a peak in the slat noise spectrum. Therefore, a *Ma* number (or freestream velocity) scaling law with an exponent of four cannot appropriately express the relationship between the slat noise level in the far-field and the *Ma* number. As shown in Figure 2.37, as the p'_{rms} values are non-dimensionalized by $u_\infty^{2.16}$, the values at the two peaks are nearly identical. Correspondingly, it can be conjectured that the SPL in the far-field should be scaled approximately with $Ma^{4.7}$ ($2.16^2 \approx 4.7$). This is close to the *Ma* number scaling law with an exponent of five[6, 38].

Modes of pressure fluctuations in the vicinity of the slat

To further investigate the behaviour of the near-field pressure fluctuations, a proper orthogonal decomposition (POD) technique was employed. The POD is a post-processing technique, which takes a set of data and extracts basis functions. The technique was originally developed by Lumley[77] to identify the most energetic coherent structures contained in a turbulent flow. If $p_k{}'$ ($1 \le k \le N$) represents a set of snapshots of the pressure fluctuations in the vicinity of the slat, with the subscript *k* representing the k^{th} snapshot, a correlation matrix can be constructed as follows

$$C_{ij} = \langle p'_i, p'_j \rangle = \int_D p'_i \cdot p'_j dx \tag{2.26}$$

The modes of the pressure fluctuations can be found by performing eigenvalue decomposition

$$CQ = Q\Lambda \tag{2.27}$$

where Q and Λ are the matrices of eigenvector and eigenvalue of the matrix C_{ij} respectively. Because the matrix C_{ij} is a nonnegative Hermitian, matrix Q is orthogonal. For each eigenvalue λ_j, there is a corresponding mode ϕ_j[78]

$$\phi_j = \frac{1}{\sqrt{\lambda_j}} V q_j \tag{2.28}$$

where q_j is the j^{th} eigenvector. The matrix V is constructed from the N snapshots

$$V = \{p'_1, p'_2, \cdots, p'_N\} \tag{2.29}$$

The k^{th} snapshot can be approximated by

$$p'_k \approx \widehat{p'_k} = \textstyle\sum_{j=1}^{N} y_j(k)\phi_j, \;\; y_j(k) = \langle p'_k, \phi_j \rangle \tag{2.30}$$

Figure 2.38 shows the comparison of the cumulative ‘energy’ between the cases of AOA = 8 and 12 degrees based on the computational results. It can be seen that the first several modes contribute a large bulk of the total ‘energy’. At AOA = 8 degrees, the first five modes contain approximately 80 percent of the total energy, while at AOA = 12 degrees only the first four modes contain an approximate amount of energy. After the 9th mode the increase in the cumulative ‘energy’ slows down.

An instantaneous pressure fluctuation field of the first mode at AOA = 8 degrees is shown in Figure 2.39. The highest values of pressure fluctuation appear near the trailing edge of the slat and the leading edge of the main element. This is similar to the overall pressure fluctuations field (shown in Figure 2.23). This is due to the fact that the first mode contains the highest ‘energy’ amongst all the modes. The time history of the pressure fluctuations of the first mode at points A and B (shown in Figure 2.40) reveals the crucial feature that the two pressures have identical magnitude but with opposite phases. This feature indicates that the first mode behaves as a pressure dipole with its axis approximately aligned along the gap line. Furthermore, the magnitude of the first mode is around 1.2 times that of the freestream dynamic pressure. This implies that the pressure dipole induces large pressure fluctuations in the slat gap region.

Figure 2.41 shows the comparison of the first four basis functions between AOA = 8 and 12 degrees. For the first basis function, the values near both the trailing edge of the slat and the leading edge of the main element at AOA = 8 degrees is clearly higher than those at AOA = 12 degrees. This means that the strength of the pressure dipole becomes weaker as the AOA increases. For the second basis function, the intense pressure fluctuations occur near the trailing edge and in the interaction region. It is known that one function of the POD technique is to find the spatially related structures. Therefore, the pressure fluctuations near the trailing edge and in the interaction region are spatially related. As mentioned previously, vortical structures are intermittently generated in the interaction region. As the vortical structures approach the trailing edge of the slat, intense pressure fluctuations are generated. The values relating to the second basis function at AOA = 8 degrees are obviously higher those at AOA = 12 degrees. In addition, a crucial feature can be observed in that the position corresponding to the highest value in the interaction region moves away from the surface of the main element when the AOA increases. At AOA = 8 degrees, the distance between this position and the surface of the main element is $0.106c_s$, while it is $0.146c_s$ at AOA = 12 degrees. Therefore, it can be concluded that as the AOA increases, the size of the circulation region becomes smaller, or the shear layer deviates away from the surface of main element. This leads to the interaction becoming weak. Hence the strength of the vortical structures decreases and, consequently, the slat noise level drops. This presents a clue into how slat noise can be attenuated: if the size of the circulation region is reduced by means of flow control, the slat noise can be attenuated. Furthermore the size of the circulation region is related to the mean velocity in the slat gap region, as the mean velocity increases the size of the circulation region decreases simultaneously with an increase in AOA. Therefore the reduction of the size of the circulation region can be implemented by increasing the mean velocity in the gap region. The attenuation of the slat noise in this manner will be discussed in Chapter 3. The third and fourth modes have minor differences in the cases of AOA = 8 and 12 degrees.

2.4 Summary

Experiments and numerical simulations were performed to investigate the phenomena of slat noise. In the experiments, the near-field noise was measured using an on-surface microphone, while the far-field noise was acquired using a phased microphone array, wherein the distance from the leading edge of the main element to the centre of the microphone array was 0.4 m, which corresponded to 2.4 wavelengths for a sound wave with a frequency of 2 kHz. The velocity in the slat region was measured using a hot-wire anemometer. PIV was employed to obtain the velocity field and fast PIV was employed to visualize the dynamic processes of the flow around the slat. Numerical simulations were performed using the DDES technique. Based on the experimental and computational results, several conclusions were made:

a) The slat noise level depends on the AOA. In this study, the noise level was lowest at AOA = 6 degrees and highest at AOA = 8 degrees. Within the AOA range from 8 to 12 degrees, the slat noise level gradually decreased with an increasing AOA.

b) Two mechanisms govern the slat noise generation. At a low AOA (6 degrees), the typical circulation region was not formed and the noise level was low. As the AOA increased to 8 degrees, vortical structures were intermittently generated in the interaction region. Intense pressure fluctuations in the reattachment region were produced as the vortical structures approached the slat cove surface. Meanwhile, the pressure fluctuations in the reattachment region led to intense pressure fluctuations near the leading edge of the main element. Consequently, a pressure dipole was produced along the gap line. When the AOA is further increased, the size of the circulation region is decreased and this interaction tended to weaken. Therefore, the pressure fluctuations in the slat gap region were weakened and the slat noise level became less.

c) Several physical variables, including TKE, $\overline{|\omega_z|}$, $\overline{|\nabla \cdot L|}$ and p'_{rms}, are employed to locate the noise sources of the slat. The locations addressed by those variables are different at some extend. It is suggested that the variable p'_{rms} is the most suitable for noise locating, because the p'_{rms}in flow region is directly related with the acoustic pressure in far-field. The variables $\overline{|\omega_z|}$ and $\overline{|\nabla \cdot L|}$ contains the mean velocity information which is weakly related to noise generation. This leads to inappropriate locations of noise sources. In addition, the variables TKE has clear relationship to p'_{rms} in the slat gap region.

d) The freestream velocity has weak effect on the mean flow field around the slat, wherein the non-dimensionalized mean velocity and pressure are not altered in an obvious way by the alteration of the freestream velocity. However, freestream velocity obviously affects the non-dimensionalized variable p'_{rms}. The p'_{rms} holds a power law of 2.16 with freestream velocity. This suggests that the slat noise in far-field has of power law of 4.7 with *Ma* number.

e) Based on the understanding of slat noise generation, two approaches, aimed at the attenuation of slat noise, can be proposed. The first is to increase the mean velocity in the slat gap region by using air blowing on the suction surface of the slat near the trailing edge. This will be demonstrated in Chapter 3. The second is to delay the formation of the circulation region in the slat cove by using a strip mounted on the surface of the main element. This will be demonstrated in Chapter 4.

Table 2.1: Matrix of wind tunnel experiments

Instruments	Wind-tunnel	Aims	AOAs (degrees)	u_∞(m/s)
PIV	0.9 m × 0.6 m	Mean flow field around slat.	6, 8, 10, 12, 14, 16	25
Fast PIV	0.35 m × 0.25 m	Dynamic process of flow around slat.	8	15
On surface microphone	0.9 m × 0.6 m	Effect of AOA on features of slat noise.	6, 8, 10, 12, 14, 16	25
Phased microphone array	0.9 m × 0.6 m		6, 8, 10, 12, 16	25
Hot-wire anemometer	0.9 m × 0.6 m	Fluctuating velocity spectra in slat gap region.	6, 8, 10, 12, 14, 16	25

Table 2.2: Primitive and corresponding post-processed variables

Primitive variables	Post-processed variables
Pressure and velocity on the integration surfaces.	Slat noise in far-field.
Instantaneous vorticity and velocity at the mid-span plane of slat.	Instantaneous or averaged values of Lamb vector, vorticity, TKE.
Instantaneous pressure at mid-span plane of slat.	POD modes and RMS of fluctuating Pressure.
Lift and drag forces.	Lift and drag coefficients.

Table 2.3: Variables and corresponding locations of slat noise

Variables	Location of noise sources
TKE	Reattachment region of shear layer.
ω_z	Reattachment region of shear layer, wake of slat cusp.
$\nabla \cdot L$	Reattachment region of shear layer, near leading edge of main element, slat gap region, wake of slat cusp.

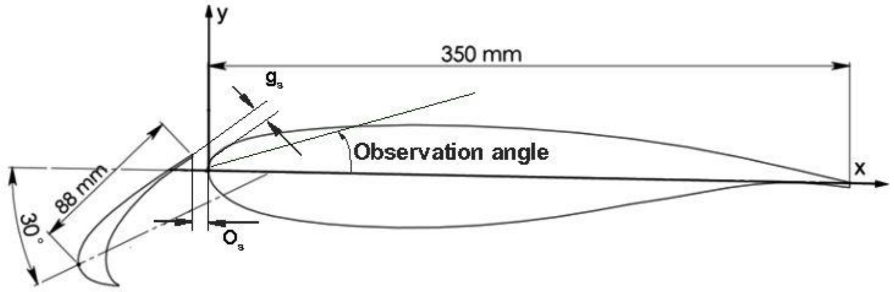

Figure 2.1: Schematic of model size and definition of observation angle.

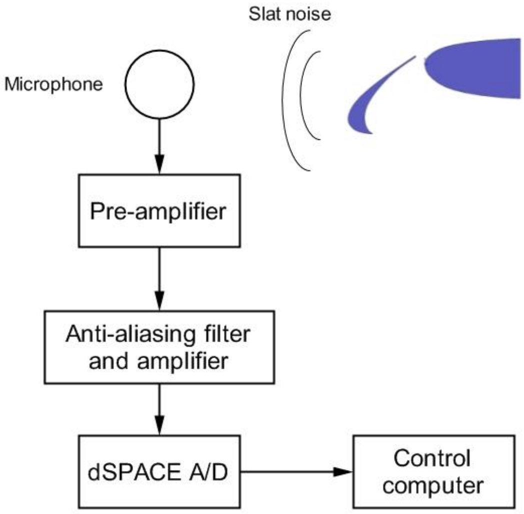

Figure 2.2: Hardware used for near-field noise measurements.

a) Photo of wind tunnel model and noise generator.

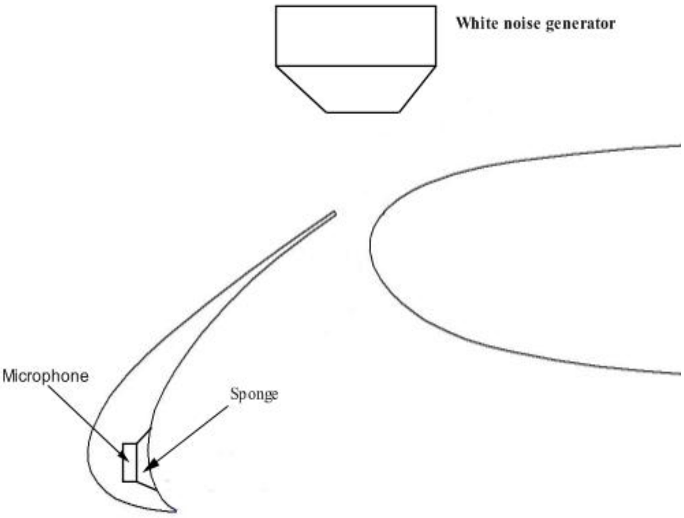

b) Configuration of microphone.

Figure 2.3: Photo and schematic of locations of noise generator and microphone.

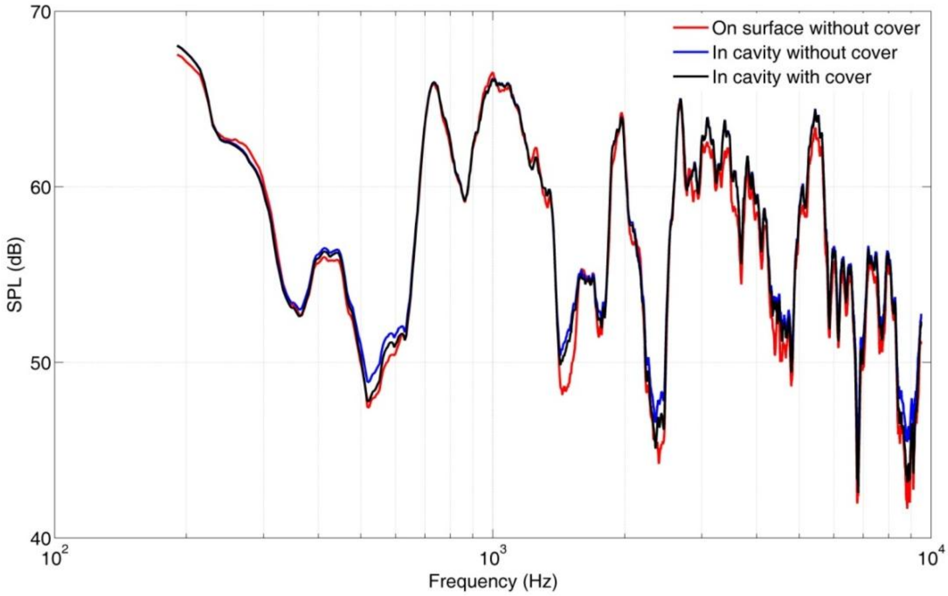

Figure 2.4: Comparison of SPLs amongst three configurations of the near-field microphone, the frequency resolution is 7.5 Hz.

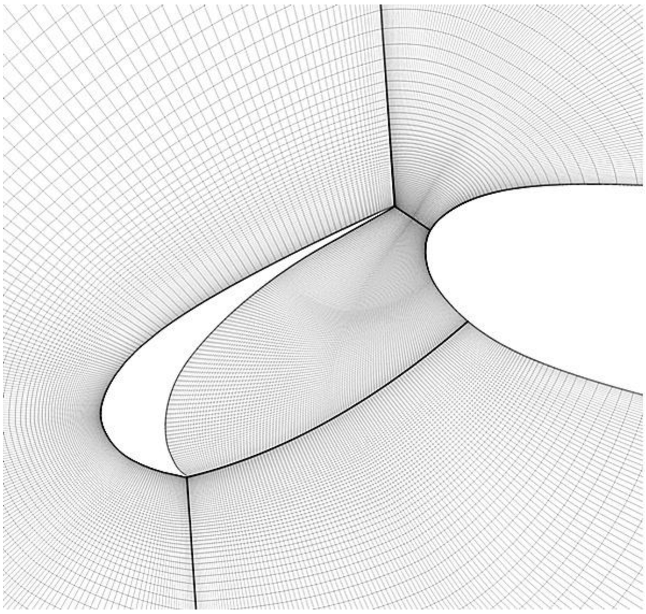

Figure 2.5: Grids in the vicinity of the slat.

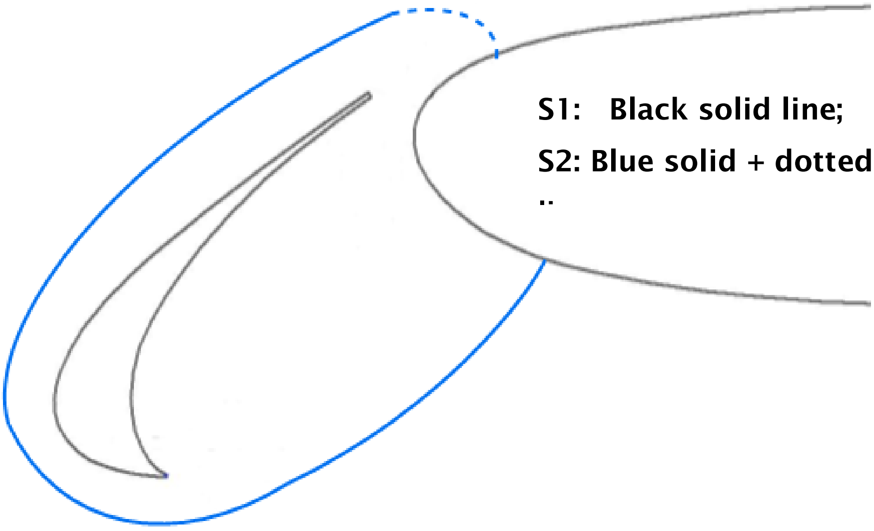

Figure 2.6: Integration surfaces associated with FW-H equations, the surface is segmented into two parts, represented by solid and dotted blue lines respectively, and black solid line represents the surface of the wing.

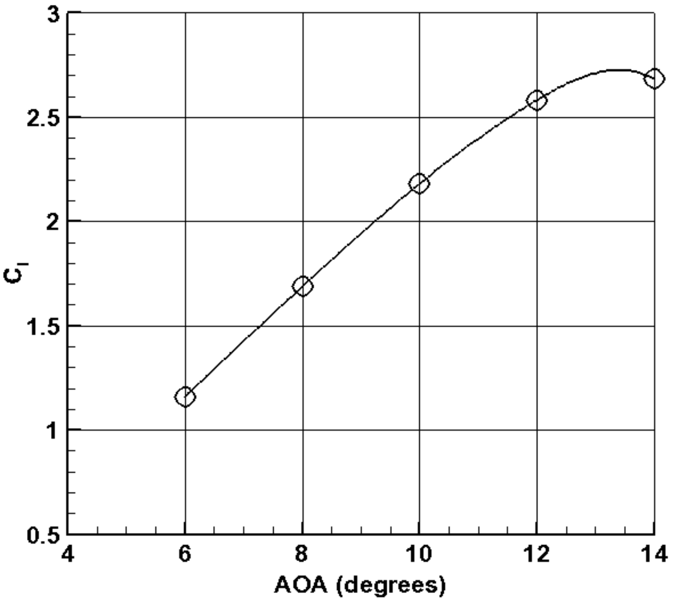

Figure 2.7: Lift coefficient curve with AOA increasing.

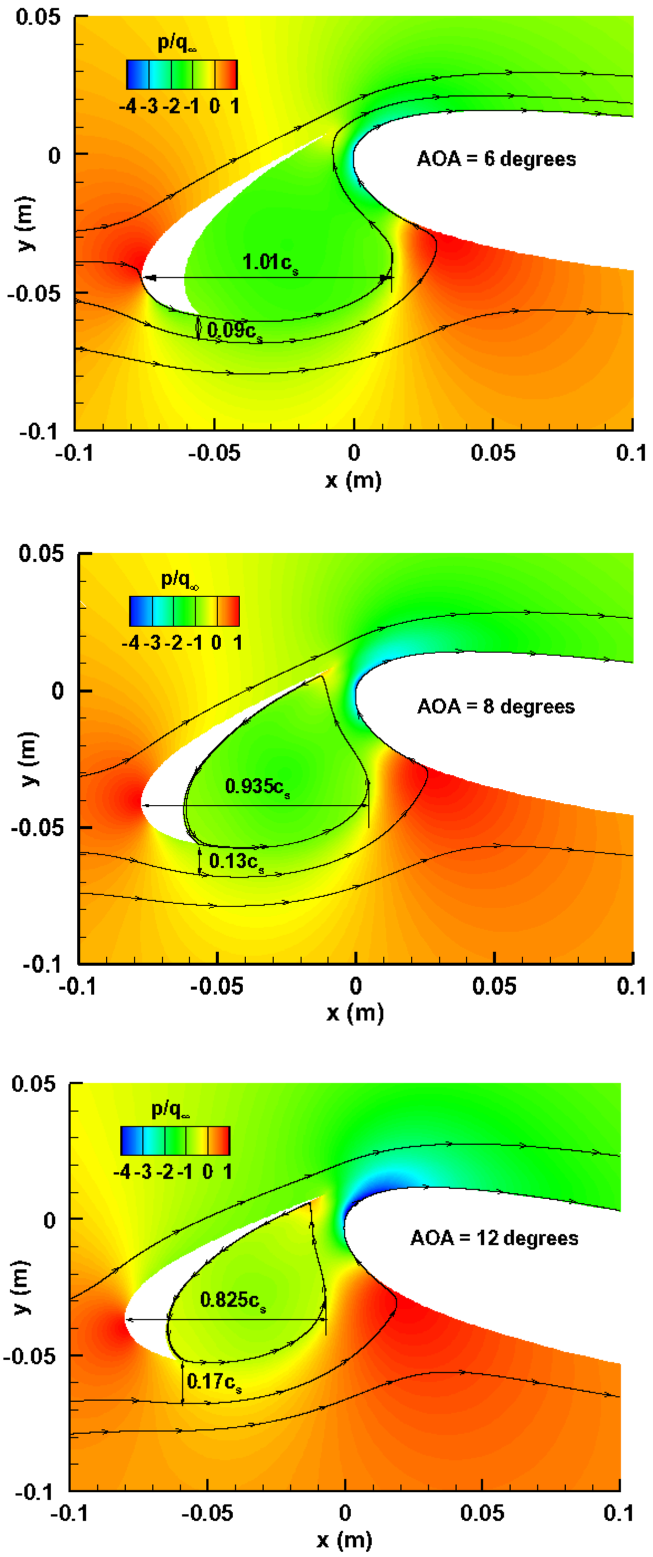

Figure 2.8: Computed mean flow field around the slat at AOAs = 6, 8 and 12 degrees at u_∞ = 25 m/s.

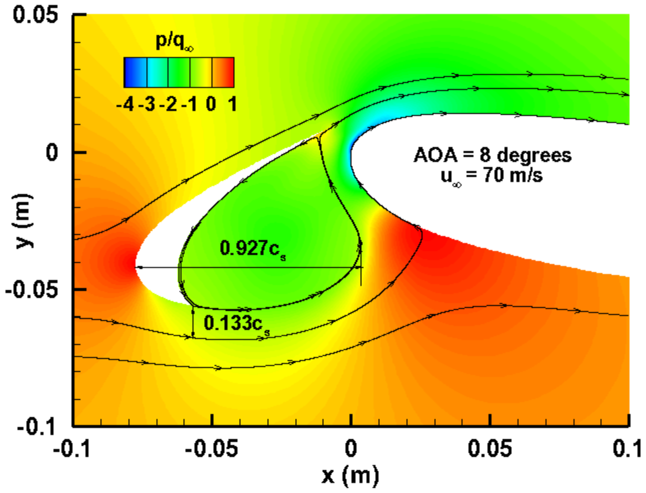

Figure 2.9: Computed mean flow field around the slat at AOA = 8 degrees and u_∞ = 70 m/s.

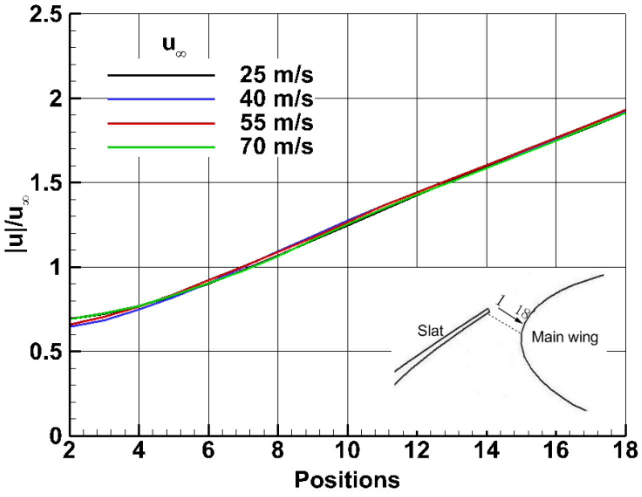

a) Velocity magnitude.

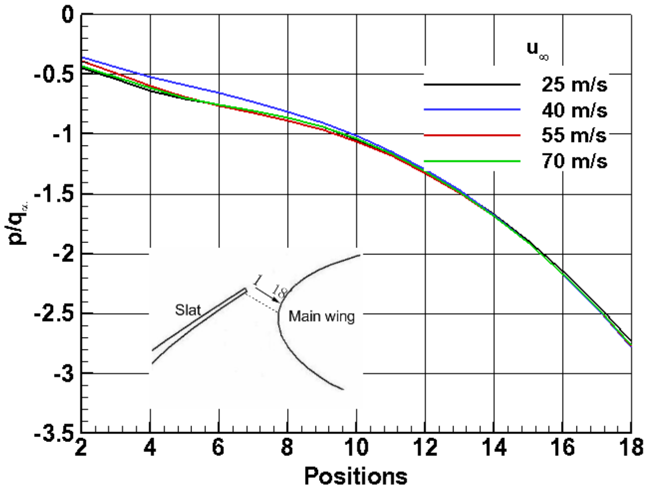

b) Static pressure.

Figure 2.10: Comparison of velocity magnitude and static pressure along the gap line at several freestream velocities.

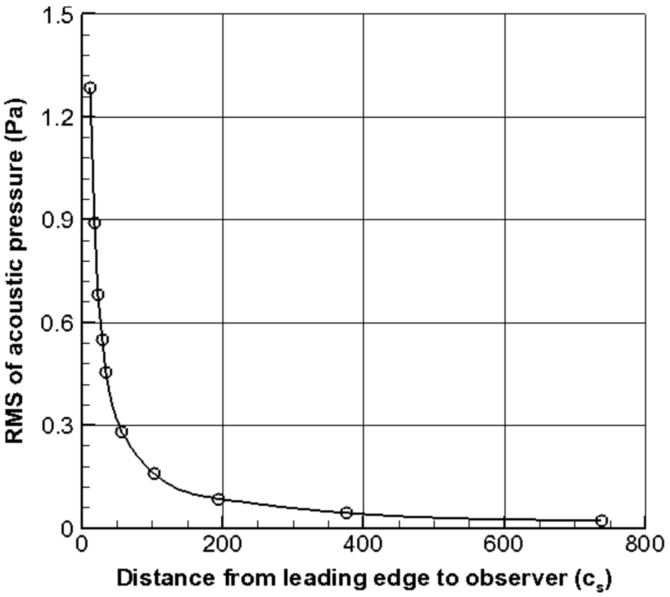

Figure 2.11: Relationship between the computed values of p'_{rms} and observer distances, where observation angle is 280 degrees, u_∞ = 25 m/s.

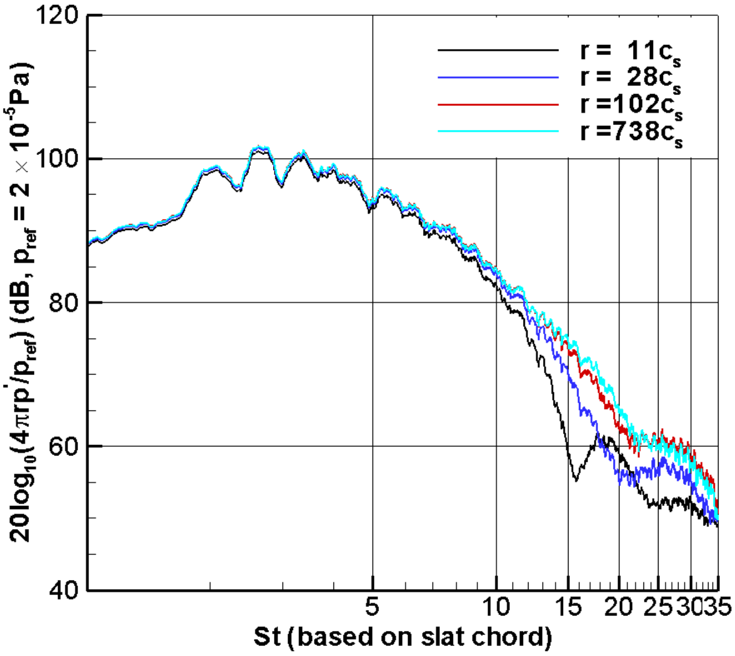

Figure 2.12: Comparison of SPLs at four distances, the observation angle is at 280 degrees, u_∞= 25 m/s.

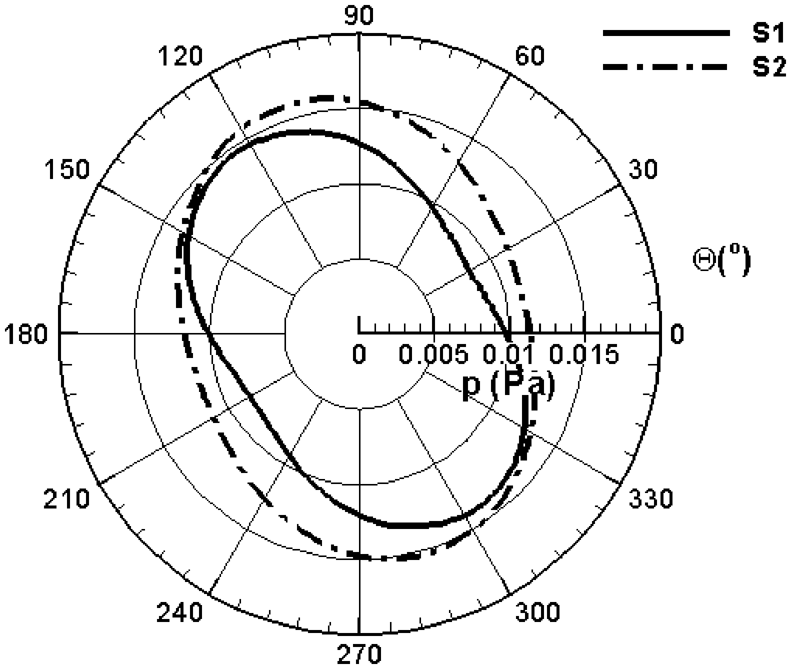

Figure 2.13: Comparison of directivities, solid line represents the values that are calculated over the blue solid line (shown in Figure 2.6), while the dotted line represents the values that are calculated over the solid and dotted lines. The distance *r* is 738c_s and u_∞ = 25 m/s.

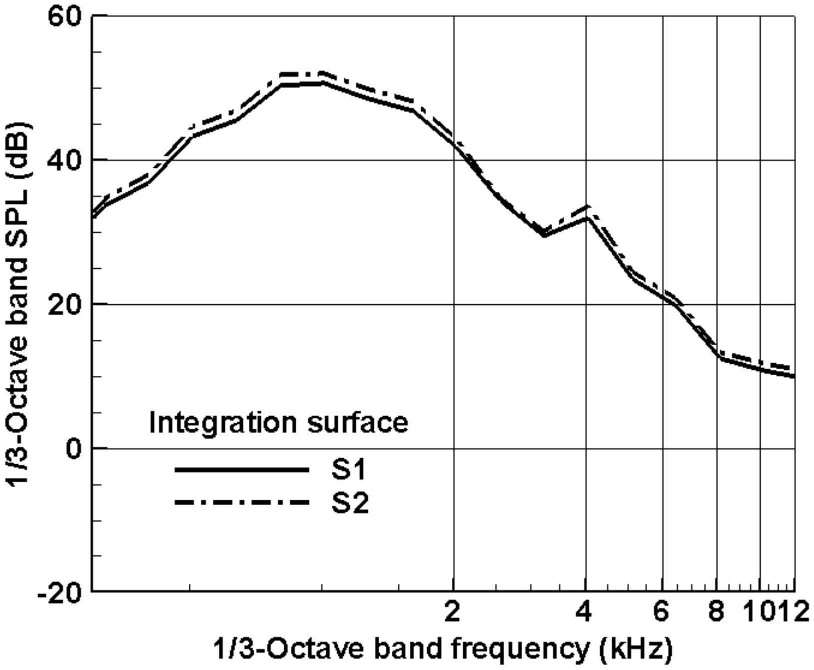

Figure 2.14: Comparison of 1/3 octave SPLs computed over surface S1 and S2 respectively at AOA = 8 degrees, u_∞ = 25 m/s.

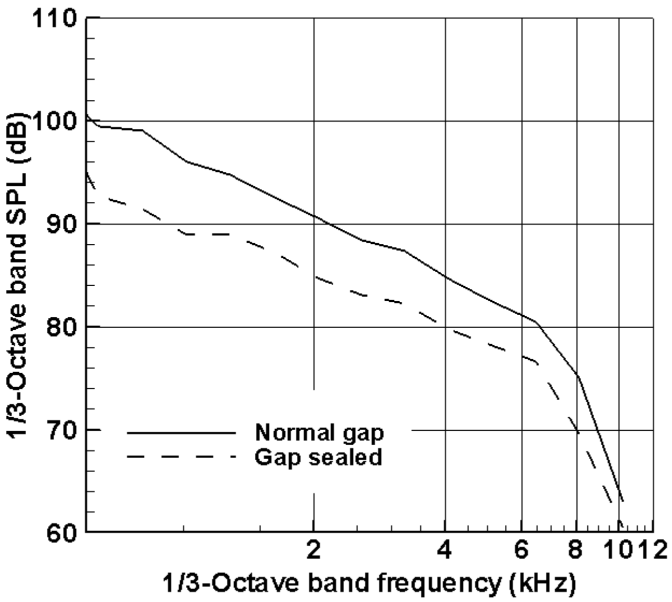

Figure 2.15: Comparison of 1/3 octave SPLs measured in the near-field between a normal and a sealed gap at AOA = 8 degrees, u_∞ = 25 m/s.

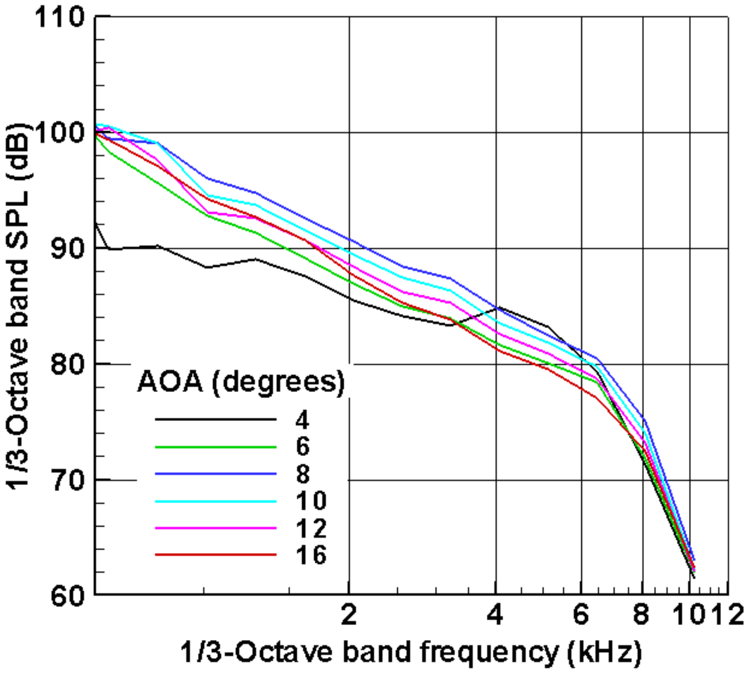

Figure 2.16: Comparison of 1/3 octave SPLs in the near-field at various AOAs and u_∞ = 25 m/s.

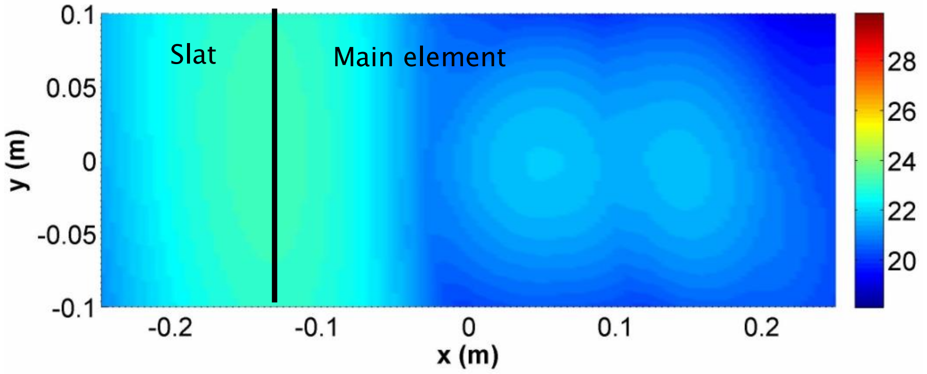

a) AOA = 6 degrees, *f* = 1.6 kHz.

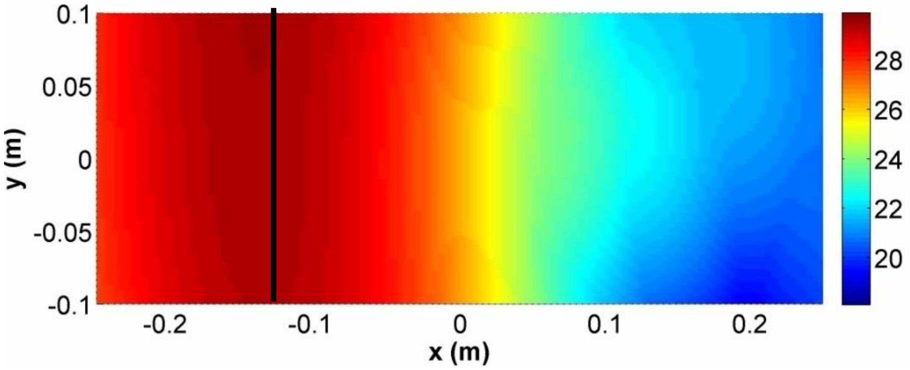

b) AOA = 8 degrees, *f* = 1.6 kHz.

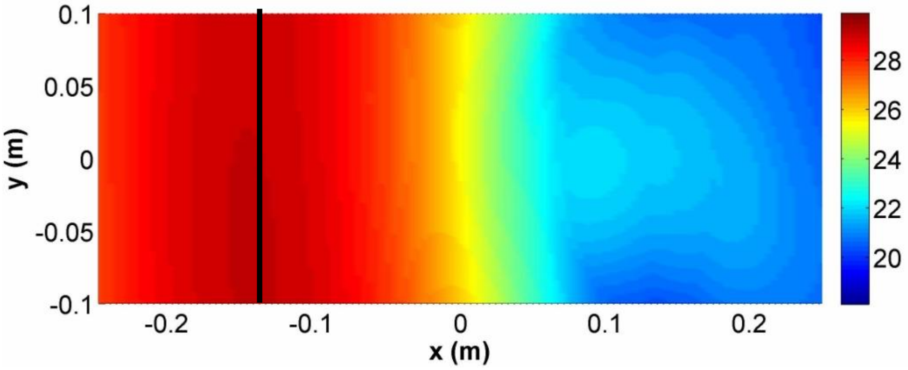

c) AOA = 10 degrees, *f* = 1.6 kHz.

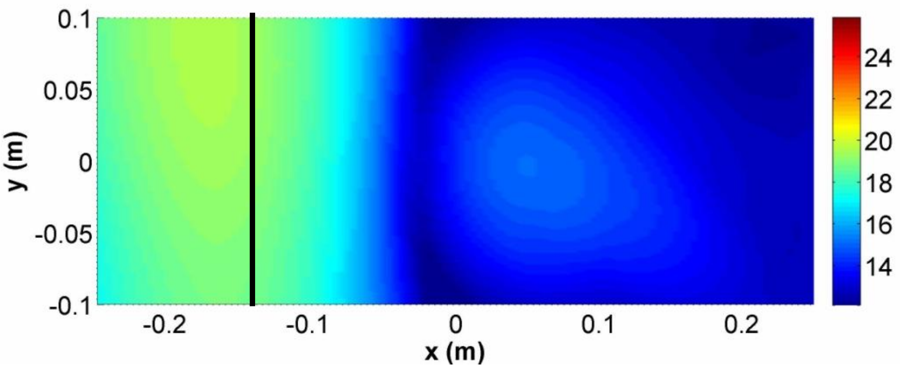

d) AOA = 6 degrees, *f* = 2.5 kHz.

Figure 2.17: Acoustic PSD images measured by phased microphone array.

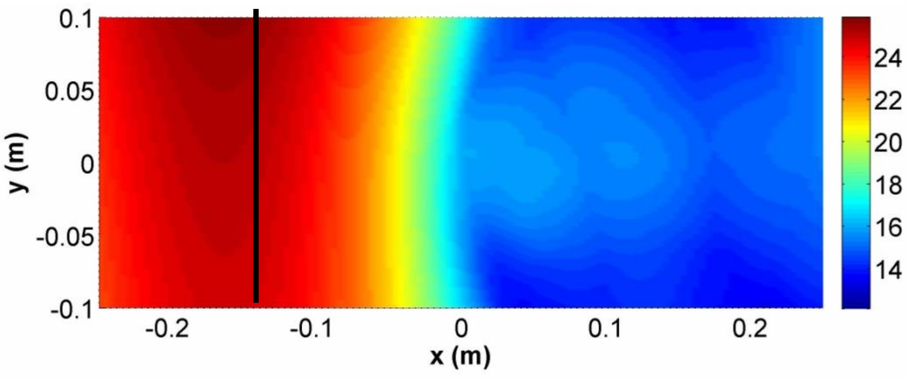

e) AOA = 8 degrees, *f* = 2.5 kHz.

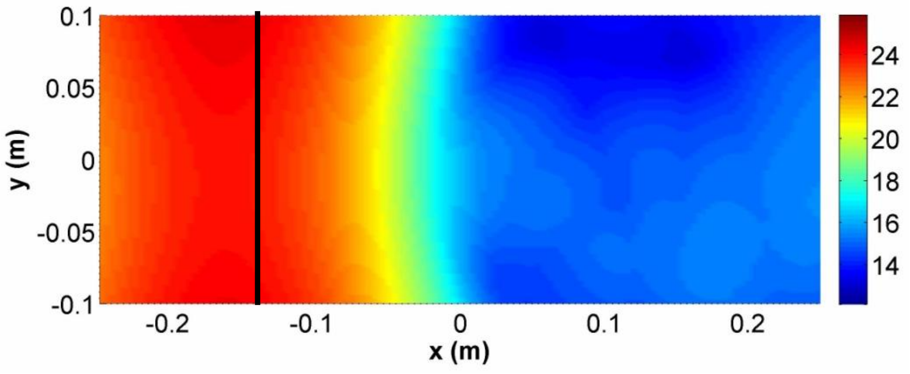

f) AOA = 10 degrees, *f* = 2.5 kHz.

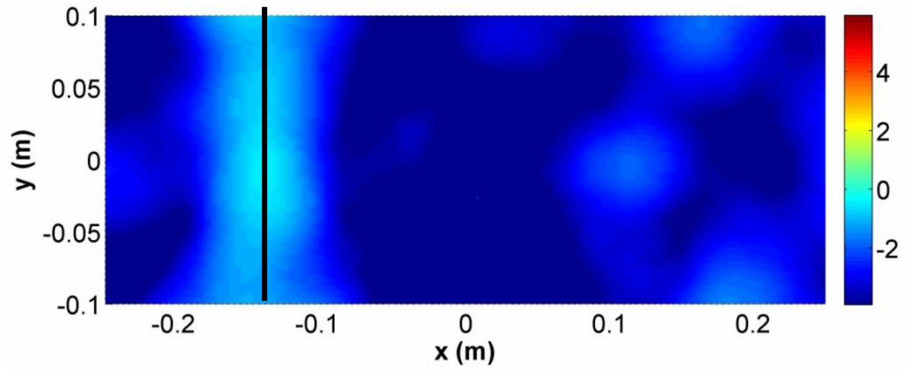

g) AOA = 6 degrees, *f* = 4 kHz.

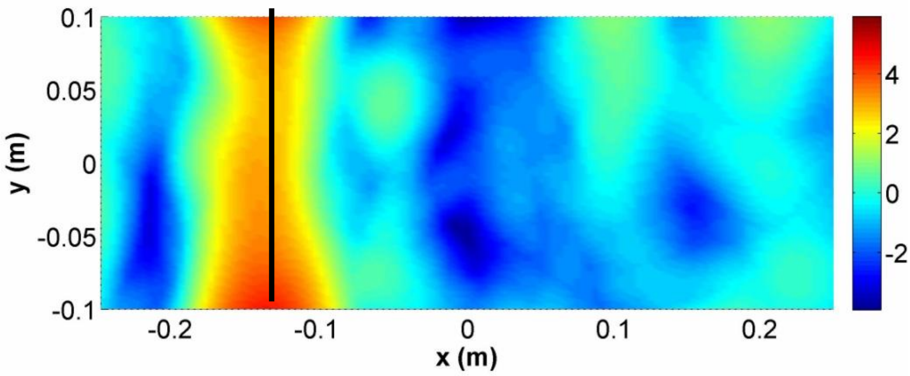

h) AOA = 8 degrees, *f* = 4 kHz.

Figure 2.17: Acoustic PSD images measured by phased microphone array.

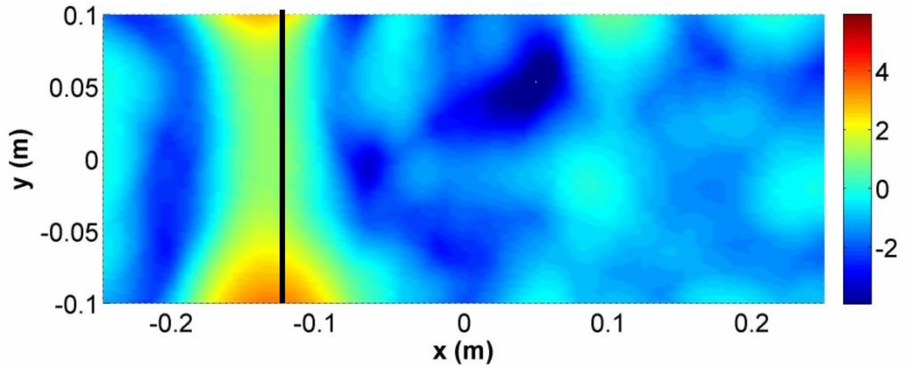

i): AOA = 10 degrees, *f* = 4 kHz.

Figure 2.17: Acoustic PSD images measured by phased microphone array.

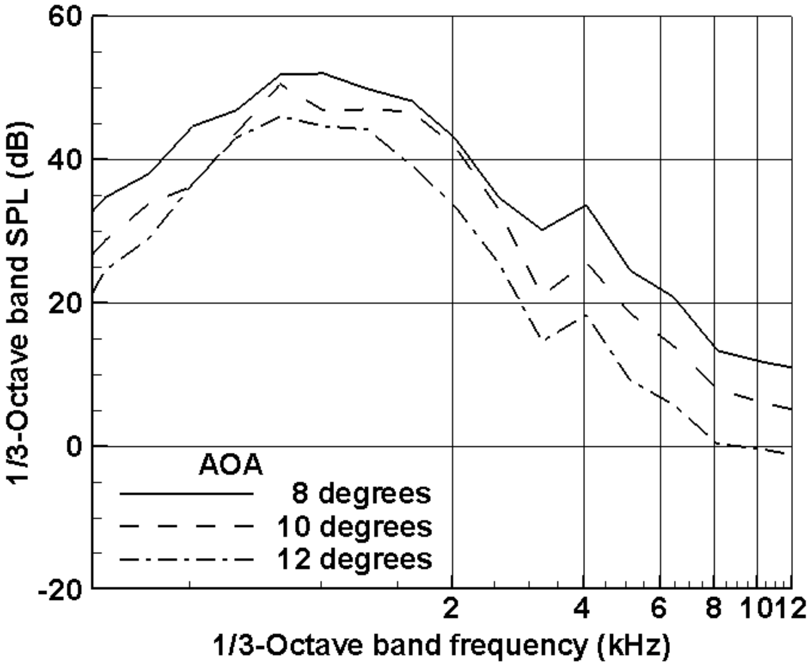

Figure 2.18: Computed noise SPL at various AOAs, $u_\infty = 25$ m/s, $r = 738\ c_s$.

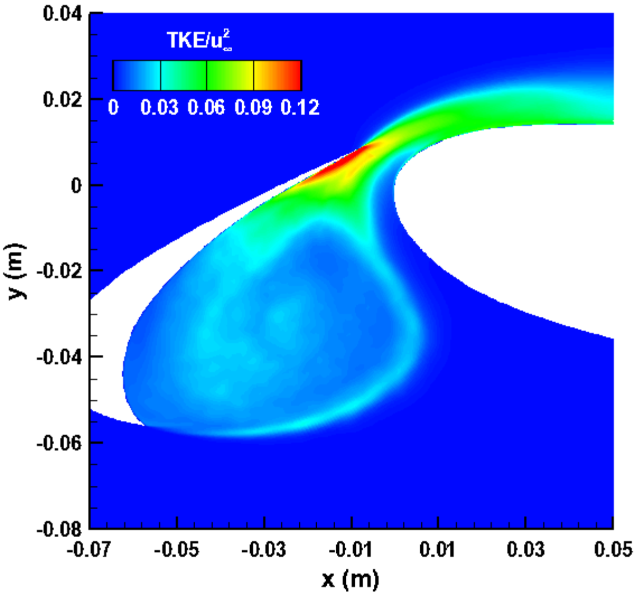

a) AOA = 8 degrees.

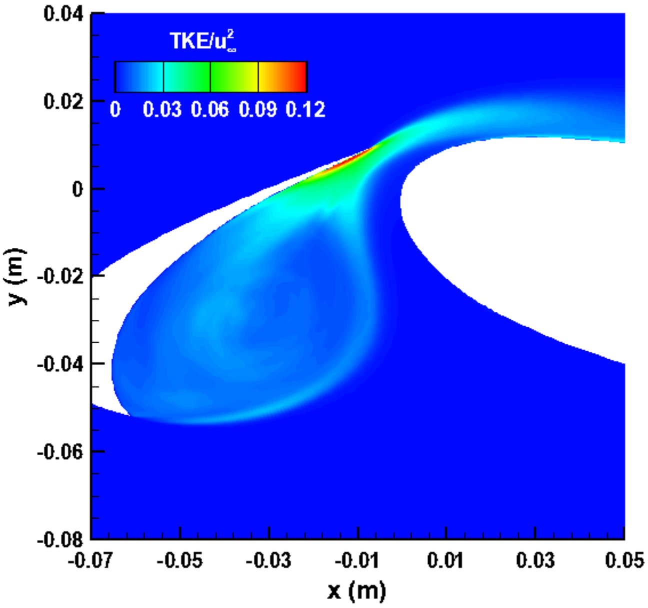

b) AOA = 12 degrees.

Figure 2.19: Comparison of computed TKE at AOA = 8 and 12 degrees, u_∞ = 25 m/s.

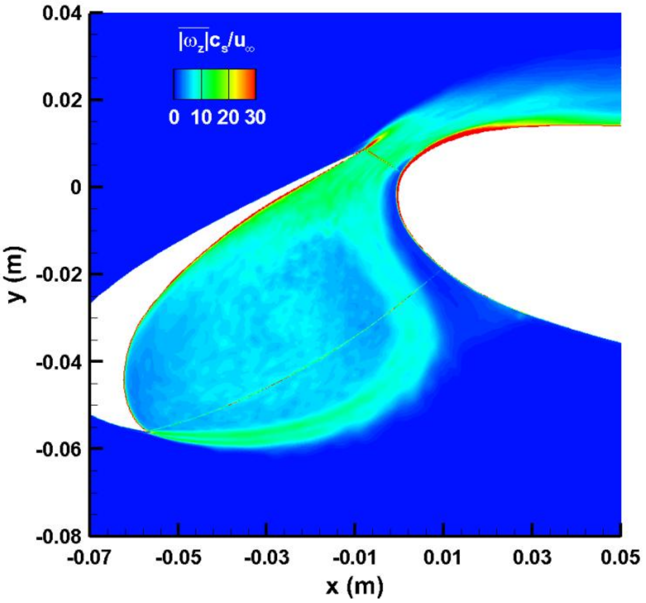

a) AOA = 8 degrees.

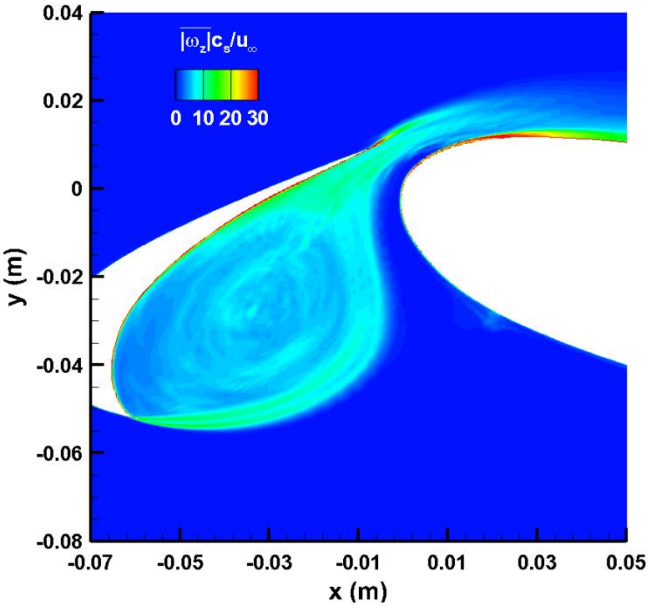

b) AOA = 12 degrees.

Figure 2.20: Comparison of computed $\overline{|\omega_z|}$ at AOA = 8 and 12 degrees, u_∞ = 25 m/s.

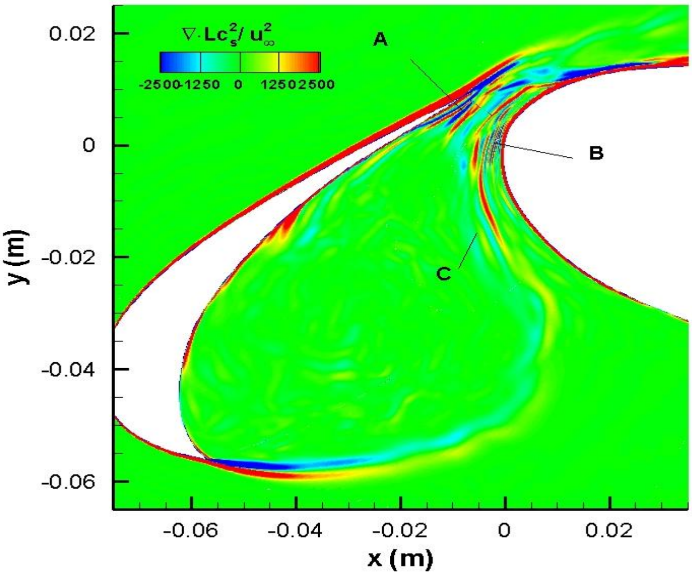

Figure 2.21: Computed instantaneous $\nabla \cdot L$ at AOA = 8 degrees, u_∞ = 25 m/s.

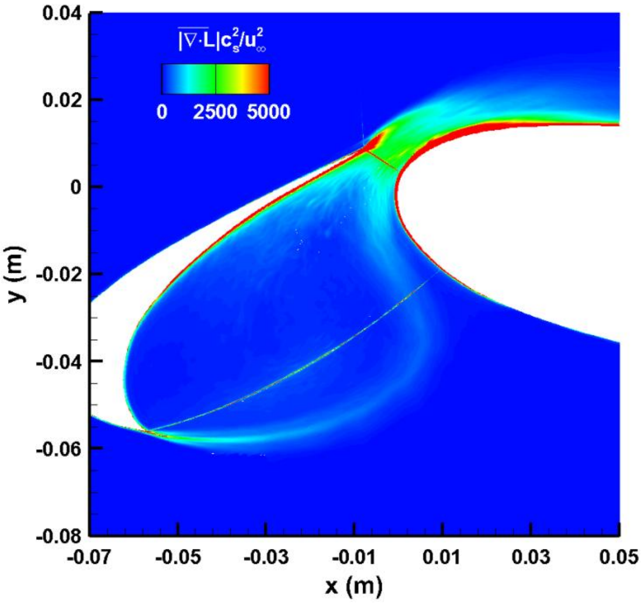

a) AOA = 8 degrees.

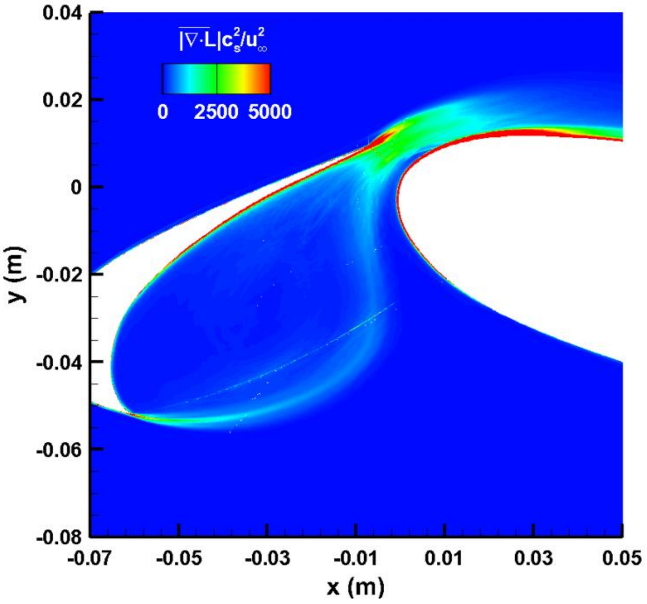

b) AOA = 12 degrees.

Figure 2.22: Comparison of computed $\overline{|\nabla \cdot L|}$ at AOA = 8 and 12 degrees, u_∞ = 25 m/s.

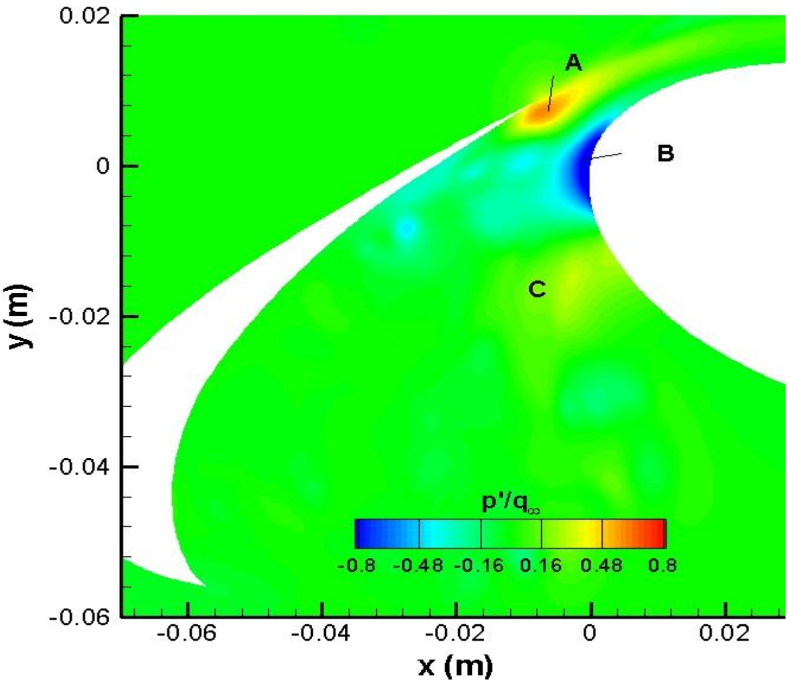

Figure 2.23: Instantaneous fluctuating pressures in the vicinity of the slat at AOA = 8 degrees, u_∞ = 25 m/s.

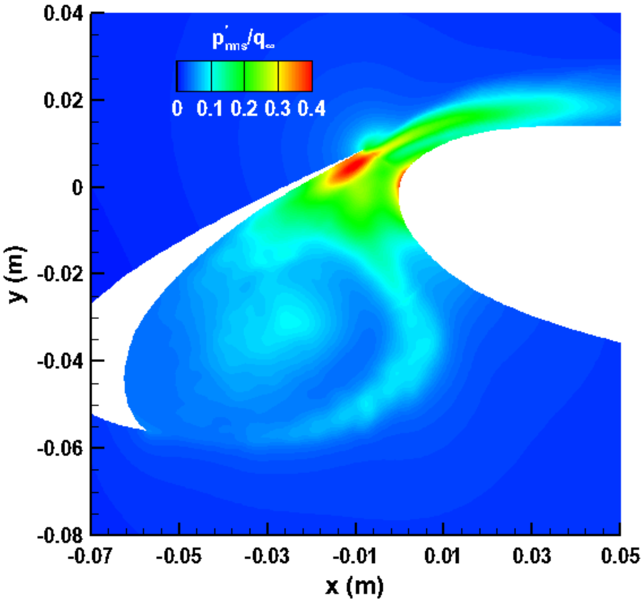

a) AOA = 8 degrees.

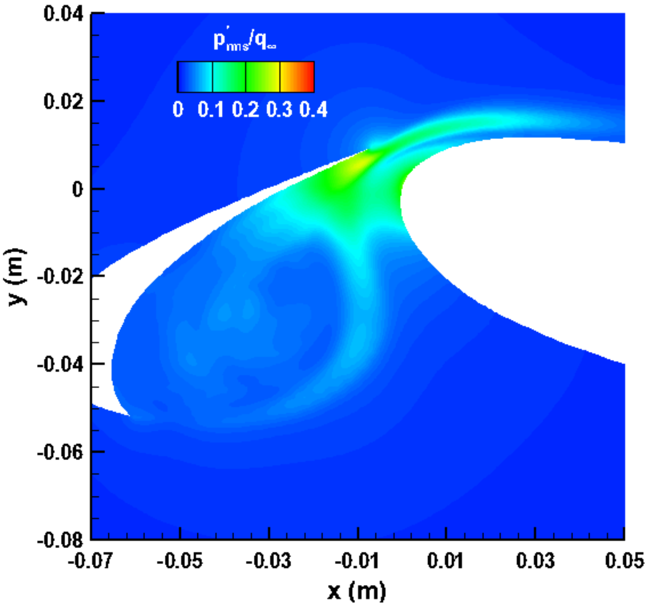

b) AOA = 12 degrees.

Figure 2.24: Comparison of computed p'_{rms} at AOA =8 and 12 degrees, u_∞= 25 m/s.

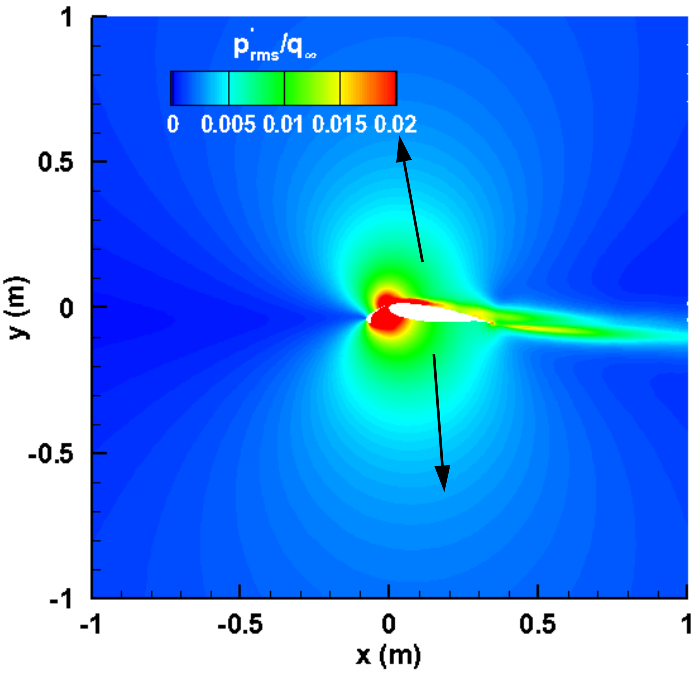

Figure 2.25: computed values of p'_{rms} in far-field at AOA =8 degrees, u_∞ = 25 m/s.

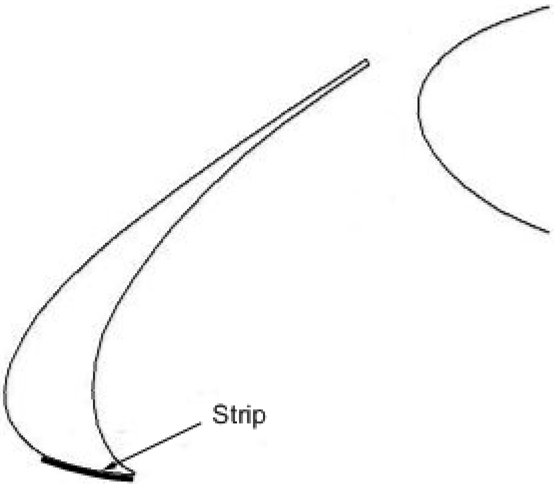

Figure 2.26: Schematic of the location of the mounted strip, wherein the strip had a thickness of 1 or 2 mm and a width of 10 mm.

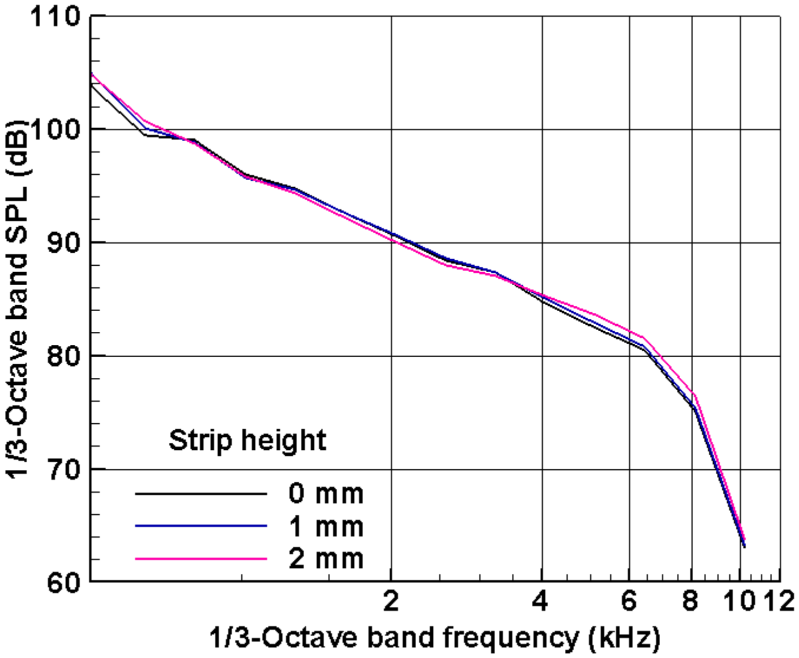

Figure 2.27: Effect of strip on the slat noise at AOA = 8 degrees, u_∞ = 25 m/s.

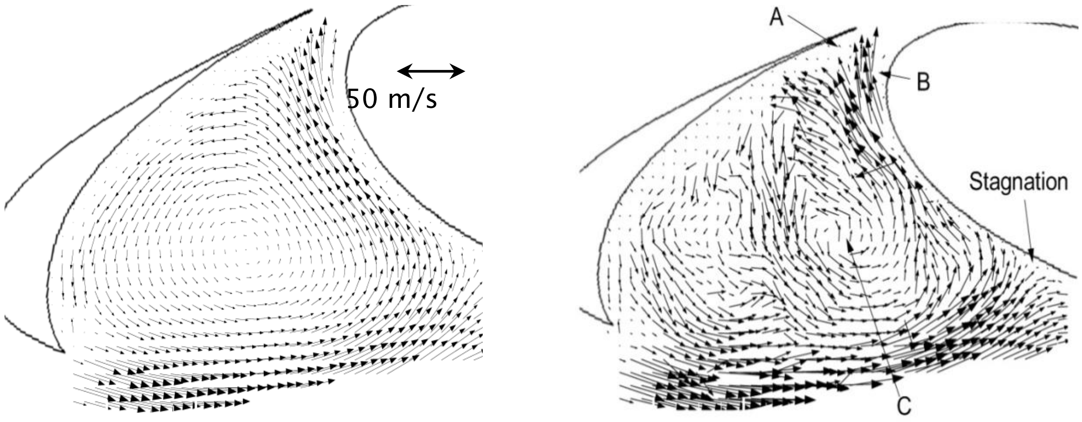

a) Mean velocity field.

b) Instantaneous velocity field.

Figure 2.28: Velocity fields in the vicinity of the slat at AOA = 8 degrees, u_∞ = 25 m/s.

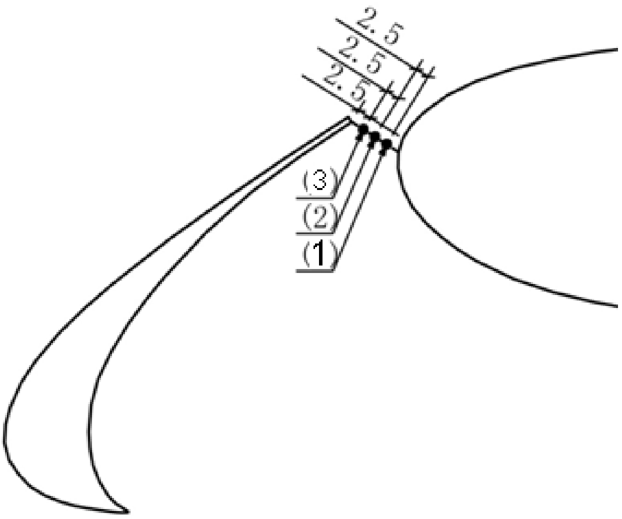

Figure 2.29: Hot-wire measurement positions. The dimensions are in mm.

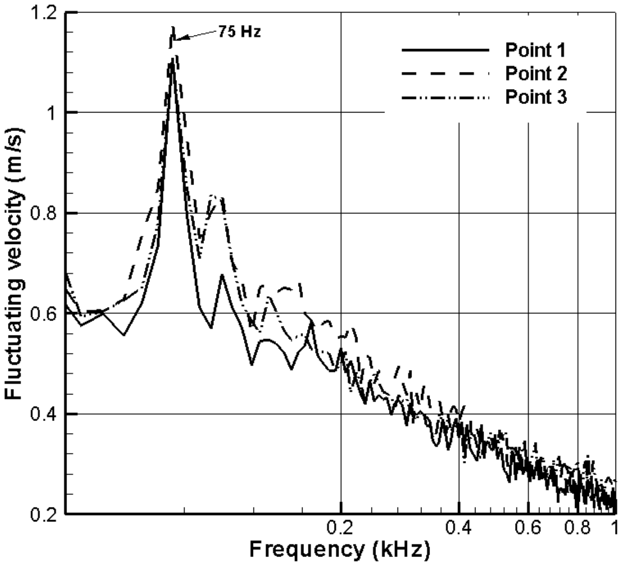

Figure 2.30: Fluctuating velocity spectrum in gap region at AOA = 8 degrees, u_∞ = 25 m/s.

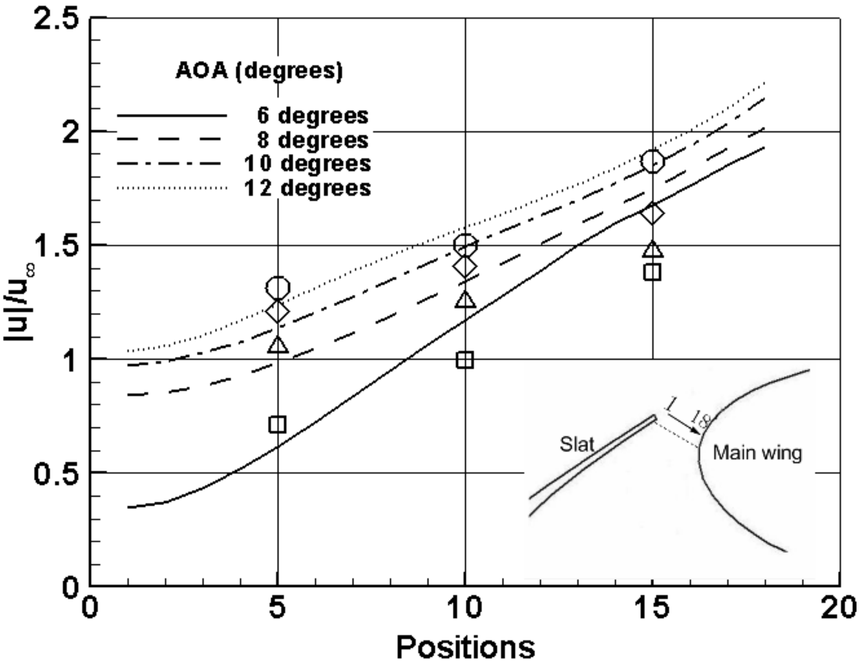

Figure 2.31: Absolute velocities at monitored positions at various AOAs, u_∞ = 25 m/s, the symbols are experimentally measured values with, □ : AOA = 6 degrees, Δ: AOA = 8 degrees, ⋄: AOA = 10 degrees, ○ : AOA = 12 degrees.

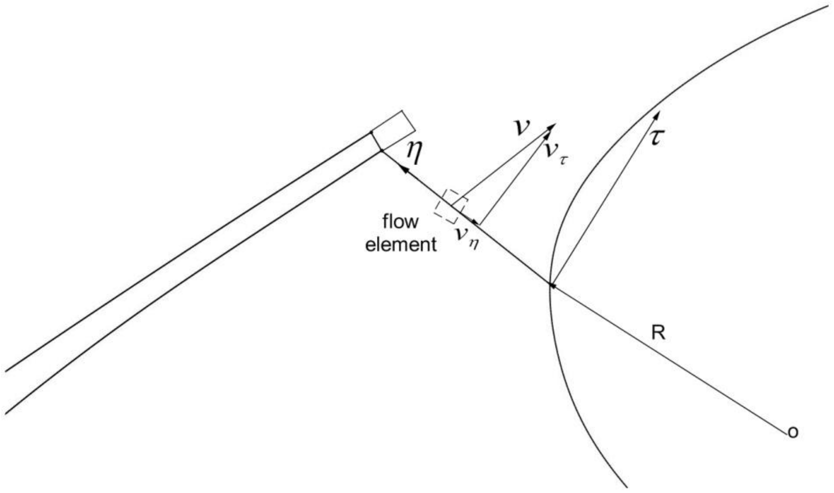

Figure 2.32: Local coordinates for the expression of flow in the slat gap region.

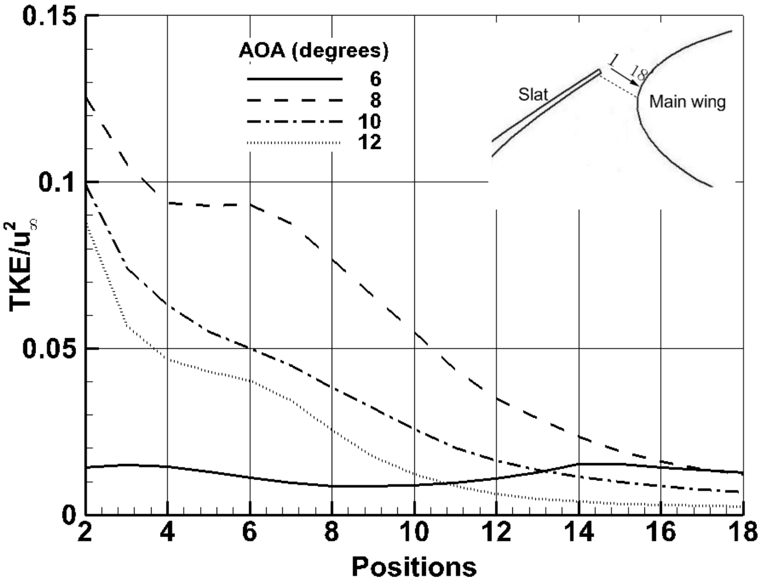

Figure 2.33: RMS of velocities at monitored positions at various AOAs, u_∞ = 25 m/s.

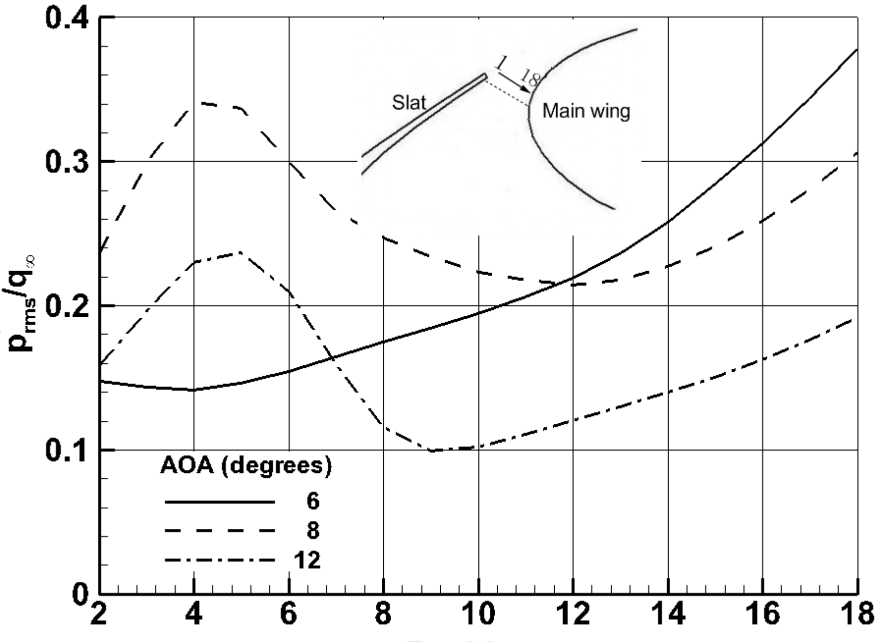

Figure 2.34: Comparison of p'_{rms} along the gap line at various AOAs.

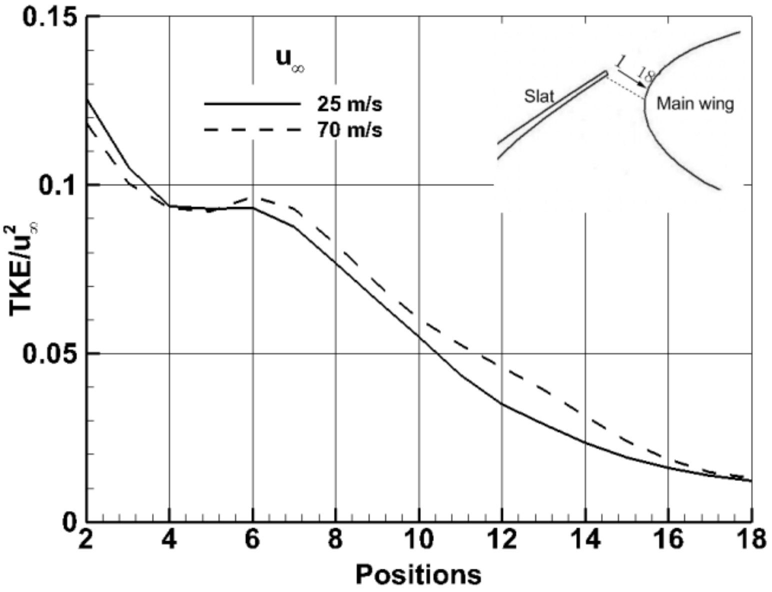

Figure 2.35: Comparison of computed TKE between u_∞ = 25 and 70 m/s at AOA = 8 degrees.

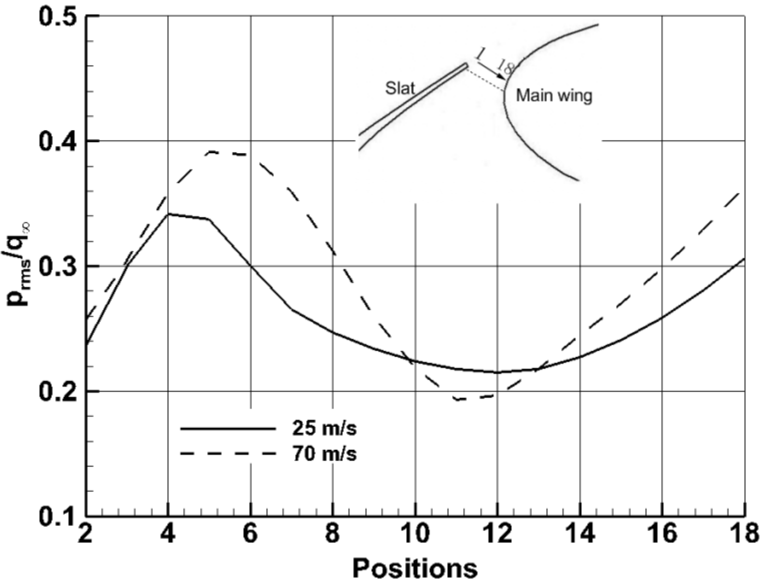

Figure 2.36: Comparison of computed p'_{rms} non-dimensionalized by q_∞ between u_∞ = 25 and 70 m/s at AOA = 8 degrees.

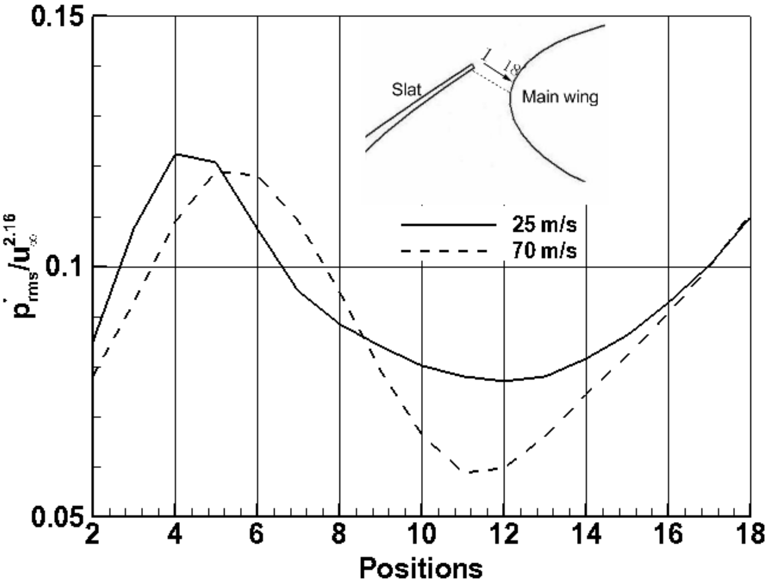

Figure 2.37: Comparison of computed p'_{rms} non-dimensionalized by$u_\infty^{2.16}$ between u_∞ = 25 and 70 m/s at AOA = 8 degrees.

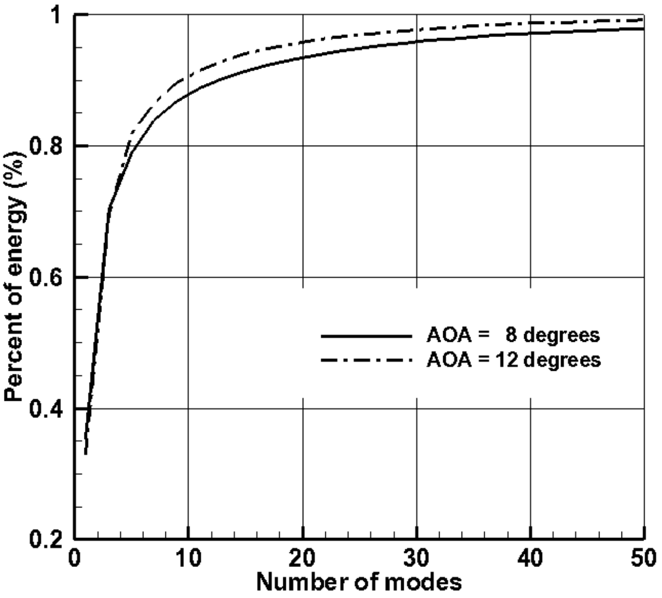

Figure 2.38: Comparison of cumulative 'energy' between AOA = 8 and 16 degrees, u_∞ = 25 m/s.

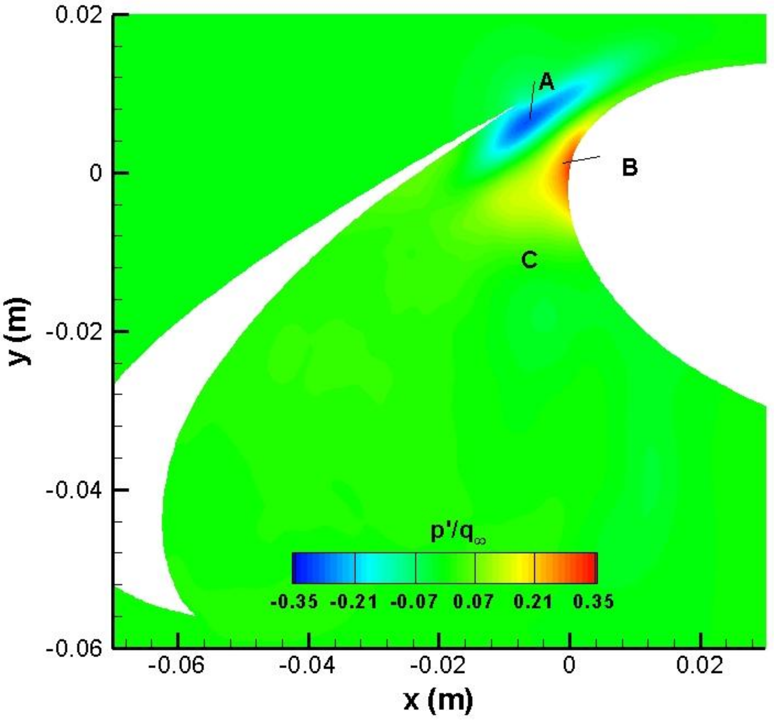

Figure 2.39: Instantaneous fluctuating pressure of the first mode at AOA = 8 degrees, u_∞ = 25 m/s.

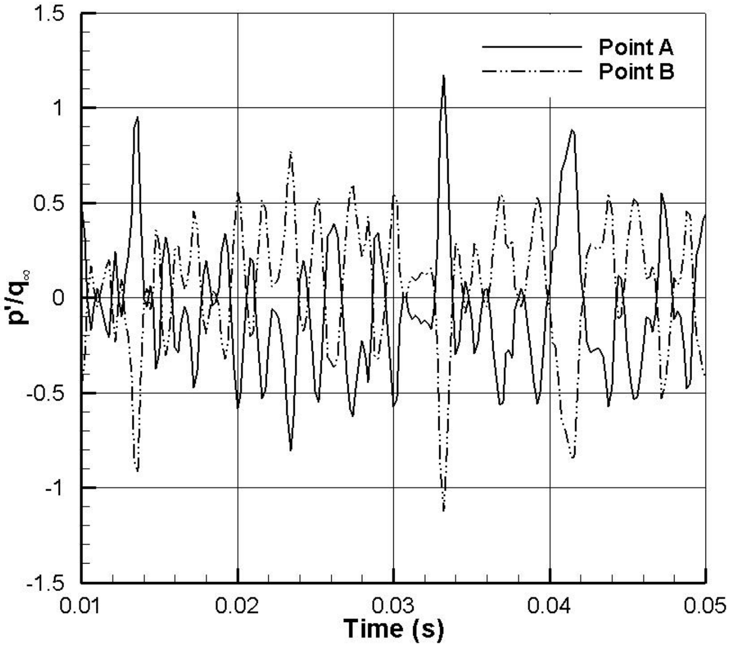

Figure 2.40: Time history of fluctuating pressure of the first mode at AOA = 8 degrees, u_∞ = 25 m/s.

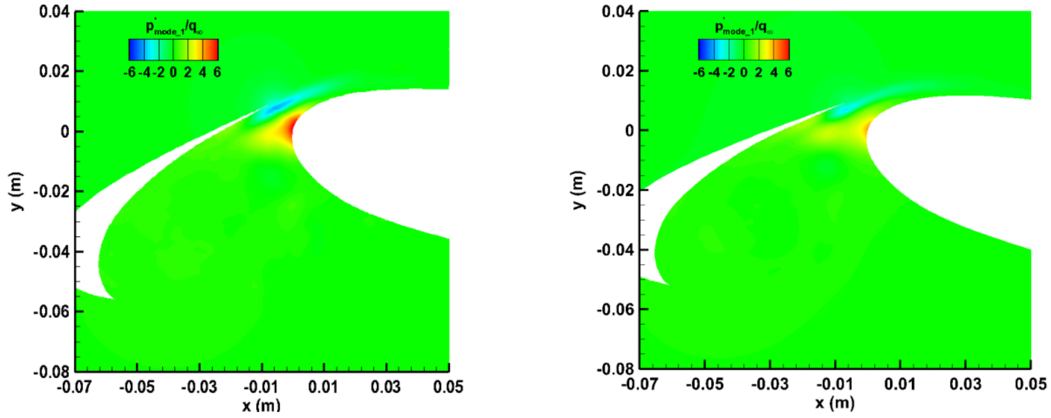

Mode 1 Mode 1

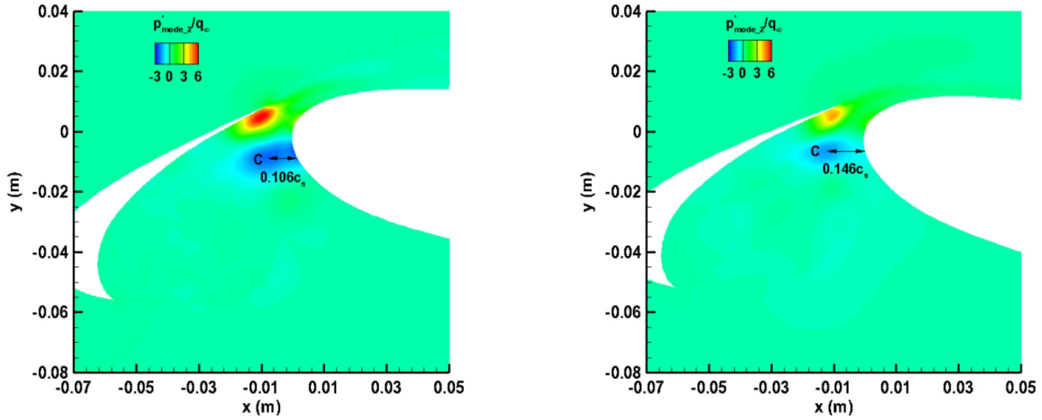

Mode 2 Mode 2

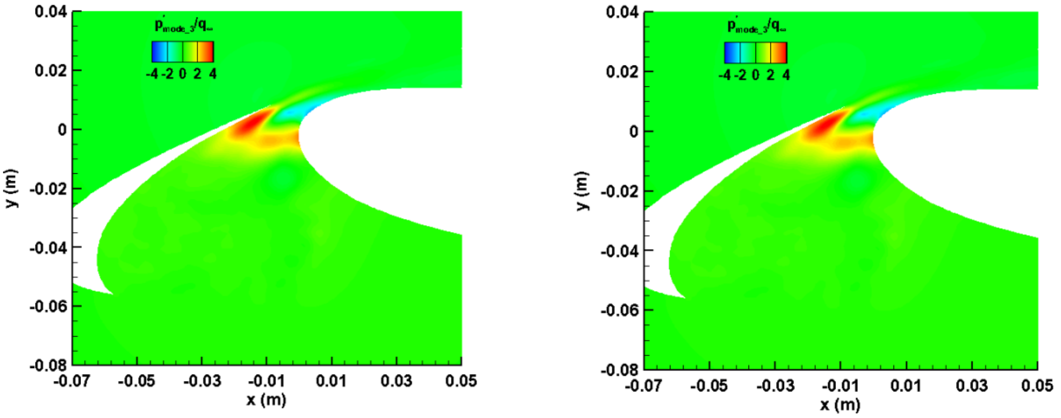

Mode 3 Mode 3

Figure 2.41: Comparison of modes of fluctuating pressure at AOA = 8 and 12 degrees, u_∞ = 25 m/s.

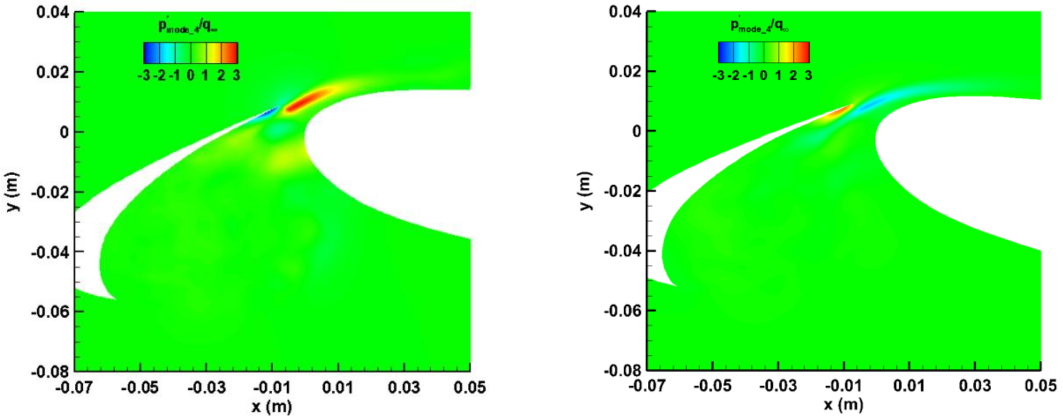

Mode 4

AOA = 8 degrees.

Mode 4

AOA = 12 degrees.

Figure 2.41: Comparison of modes of fluctuating pressure at AOA = 8 and 12 degrees, u_∞ = 25 m/s.

Chapter 3

Slat Noise Reduction Using Air Blowing

The slat has been described as being one of the main contributors to airframe noise in the approach-to-landing phase[5, 20]. Slat noise represents a complex aeroacoustic problem and the underlying mechanisms have been extensively explored in the past. Due to the complexity of the slat noise generation, not all of the technologies developed provided a breakthrough in terms of noise reduction as some also resulted in a degradation of the lift performance[25]. Imamura *et al.*[35] tested several kinds of cove fillers, which filled the slat cove to form a streamlined cove surface, the results showed that the filler could reduce the noise significantly. Similar work conducted by Khorrami and Lockard[32], demonstrated that the slat noise could be reduced by attaching an extended seal to the slat cusp. These two approaches reduced the slat noise by reducing the vorticity intensity in the free shear layer between the cove vortex and the slat gap flow[31]. Chow *et al.*[22] demonstrated that rows of brushes attached to the upper slat trailing edge could lead to a significant far-field noise reduction, mainly for lower frequencies. Soderman *et al.*[20] showed that applying a serrated trailing edge to the slat was also an effective method. When a portion of the surfaces of the slat cove and main element were covered with an acoustic liner, Ma and Zhang[37] showed that the slat broadband noise could be reduced by at least 2 dB.

As discussed in Chapter 2, it was suggested that the intermittently generated vortical structures in the slat cove contributed to the slat noise generation. Based on the POD of the pressure fluctuations in the vicinity of the slat, the second mode showed that the pressure fluctuations in the reattachment region and the interaction region were spatially cross-related. If the pressure fluctuations in the reattachment region were regarded as the dominant noise source, the slat noise could be alleviated by reducing the pressure fluctuations in the interaction region. In addition, the size of the circulation region plays a crucial role in the interaction; a smaller size corresponds to a weaker interaction. Furthermore the size of the circulation region is related to the mean velocity in the gap region, with a higher mean velocity corresponding to a smaller size. The mean velocity in the gap region gradually increased from the trailing edge of the slat to the leading edge of the main element, and the lowest velocity occurred close to the trailing edge. The above mentioned relationships led to the idea that the slat noise could be attenuated by increasing the velocity close to the trailing edge. The complete logic with respect to this idea is as follows. The increased velocity close to the trailing edge of the slat leads to the velocity in the entire slat gap region increasing. Consequently, the size of the circulation region is reduced. This result in the interaction between the shear layer and the flow convected from the stagnation line on the main element becoming weak. A weak interaction corresponds to less vortical structures being generated in the interaction region. Hence pressure fluctuations tend to be less in the same region. Due to the spatial correlation between the pressure fluctuations in the interaction region and in the reattachment region, the pressure fluctuations in the reattachment region tend to also be low. Because the pressure fluctuations in the reattachment region are the dominant noise source, the slat noise becomes less due to the decrease in these pressure fluctuations. This idea was numerically tested and proven to be effective in reducing the slat noise. To implement this method, air was blown out from a portion of the slat suction surface near the trailing edge. This led to an increase of the mean velocity in the slat gap region. In this Chapter, this method of air blowing is introduced, followed by a comparison between the slat noise levels both in the absence of and in the presence of the air blowing. Secondly, the values of the various variables, e.g., the TKE and pressure fluctuations, are compared. Finally, the underlying mechanisms which govern the reduction of the slat noise are discussed.

3.1 Setup

The geometric size of the model, the numerical techniques and the integration surfaces used in the solution of the FW-H equation are the same as those introduced in Chapter 2. Figure 3.1 schematically shows the configuration of the air blowing technique. Air was uniformly blown out from a fractional surface of the slat near the trailing edge. The angle between the air blowing vector and the surface of the slat was set to 30 degrees. There are two considerations in the choice of the angle. One is that the wing's performance cannot be degraded by the airblowing. Airblowing in upstream direction is unavoidably to cause flow separation, and then degrade the wing's performance. Another is that airblowing in a direction tangent with the surface of the slat is not easily implemented in practice. The air blowing was simulated by setting a boundary profile in the Fluent software. The boundary profile had a length of 10 mm, corresponding to $0.11c_s$. This length should be large sufficiently to provide adequate momentum to effectively affect the flow. It can be seen later that the airblowing can indeed significantly change the flow near the trailing edge of the slat. The disadvantage of a large length is more energy consumed. By contrast, short length needs less energy. Therefore, an optimized length should be adopted to compromise the positive effectiveness of the airblowing with energy needed. The velocity magnitude of the air blowing was set to 0, 20 and 60 m/s respectively. The velocity, v_j, were set to 25 m/s. If momentum coefficient is defined as $c_\mu = {v_j^2 b}\Big/{(\frac{1}{2}u_\infty^2 c_s)}$, where *b* is the length of the airblowing profile. The momentum coefficients are 0, 0.0145, 0.131

corresponding to v_j = 0, 20 and 60 m/s respectively. The AOA was set to 8 degree. As discussed in Chapter 2, the interaction becomes the most intensive at this angle. Since one aim of the research is to test whether the airblowing can suppress the interaction effectively, it is expected that an evident outcome can be achieved at this degrees.

3.2 Results and Discussions

3.2.1 Mean Aerodynamic Features

Table 3.1 shows the effects of the air blowing on the aerodynamic performance of the wing. The lift coefficients increase by 8.6 and 34.4 percent as the velocity magnitude of the air blowing is set to 20 m/s and 60 m/s respectively. The drag coefficients drop significantly. Figure 3.2 shows the comparison of the mean flow field amongst the three cases corresponding to v_j = 0, 20 and 60 m/s respectively. Figure 3.3a shows a close-up view of the velocity near the trailing edge of the slat. It can be seen that the blowing air results in significant alteration of flow direction near the trailing edge. Figure 3.3b shows the comparison of mean velocity distribution along the monitoring line (shown in Figure 3.3a), wherein the monitoring line with a length of approximately 6 mm (corresponding to $0.068c_s$) is perpendicular to the surface of the slat, and 20 monitors are evenly collocated along the line. No obvious difference in the velocity distributions can be seen as the monitor number is larger than 7, but significant change near the trailing edge. In the absence of the airblowing, the velocity close to the surface is around zero, this is the requirement of no-slip boundary condition. According to the results, the airblowing with velocity magnitude of 25 m/s significantly alters the flow velocity profile of the boundary layer, wherein the flow velocity close to the surface equals to approximately 25 m/s, which is identical to airblowing velocity magnitude. In addition, the velocity gradient in the boundary layer becomes small. In the case of v_j = 60 m/s, the flow velocity near the surface is increased significantly and much larger that the freestream velocity. Several features can be observed from Figure 3.2. Firstly, the cusp channel width increases with v_j. The width is $0.13c_s$ at v_j = 0 m/s, 0.143cs at v_j = 20m/s and $0.18c_s$ at 60 m/s. As discussed in Chapter 2, a wider channel corresponds to a higher mean velocity in the slat gap region. Secondly, according to the comparison of the mean velocity along the gap line for the three cases (shown in Figure 3.4), the mean velocity associated with v_j = 60 m/s case is the highest, followed by the v_j = 20 m/s case. Therefore, the air blowing is effective in increasing the velocity in the slat gap region. Meanwhile, the velocity slopes have not been altered by the air blowing. That is required by Equation (2.21). Thirdly, in the presence of the air blowing, the static pressures along the gap line drop significantly. The increase in lift force can be attributed to this pressure drop. Because of the pressure drop close to the leading edge of the main element, the suction force (normal to the surface of the main element) is increased. Finally, the air blowing had an obvious effect on the size of the circulation region. In this study, the size of the circulation region was measured by the distance from the leading edge of the slat to the vertex of the shear layer, and non-dimensionalized by the slat chord. It can be seen that the size decreases with the magnitude of v_j, wherein the sizes are $0.935c_s$, $0.907c_s$ and $0.835c_s$ at v_j = 0, 20 and 60 m/s respectively. Figure 3.6 shows the relationship between the cusp channel width and the size of the circulation region, and the size decreases linearly with the channel width. As mentioned above, the size of the circulation region has a close relationship with the slat noise level; a small size corresponds to a low slat noise level. Therefore it is expected that the slat noise can be successfully attenuated by air blowing.

3.2.2 Effects of Air Blowing on Slat Noise Level

Figure 3.7 shows the comparison of the 1/3 octave band SPLs for the three cases. The observer was located at an observation angle of 280 degrees and away from the model by $738c_s$. The highest level appears at a frequency of approximately 1 kHz, corresponding to a *St* number of 3.5. This *St* number exceeds the value of 2, at which the highest level should occur[25]. According to the results, the slat noise is slightly attenuated at frequencies lower than 0.6 kHz. Within the frequency range of 0.6 kHz to 2 kHz, the air blowing has no obvious effect on the slat noise. However above a frequency of 2 kHz, the slat noise is significantly attenuated. This is especially so at a frequency of 4 kHz, where a reduction of approximately 5 dB corresponding to the v_j = 20 m/s case, and approximately 10 dB corresponding to the v_j = 60 m/s case, is evident. It can also be seen that the reduction associated with the v_j = 60 m/s case is larger than that associated with the v_j = 20 m/s case throughout the entire frequency range.

Nonetheless, an issue arose when comparing the noise levels between the v_j = 60 m/s case and the AOA = 12 degrees case (shown in Figure 2.18). The main features of the mean flow field in the v_j = 60 m/s case, including the cusp channel width and size of the circulation region, are nearly identical to those associated with the AOA = 12 degrees case. However the slat noise level at AOA = 12 degrees is significantly lower than that at v_j = 60 m/s. This is suspected to be resulting from the air blowing inducing other noise sources and will be discussed further later.

3.2.3 Effects of Air Blowing on Slat Noise Sources

The slat noise sources can be represented by several physical variables, such as $|\omega_z|$, $|\nabla \cdot L|$, TKE and p'_{rms}. Figures 3.8 and 3.9 show the comparisons of the values of $|\omega_z|$ and $|\nabla \cdot L|$ for the three cases. The values of $|\omega_z|$ and $|\nabla \cdot \mathrm{L}|$ in the wake of the trailing edge of the slat are obviously higher in the presence of the air blowing. This results from the fact that the velocities increase and sharper velocity gradients are produced in the wake of the trailing edge. Consequently, the values of $|\omega_z|$and $|\nabla \cdot L|$ increase. Nonetheless, those increased values do not correspond with a decreased noise level. Figure 3.10 shows the comparison of the TKE values in the vicinity of the slat and Figure 3.11 shows the comparison of TKE values along the gap line at AOA = 8 degrees and u_∞ = 25 m/s. The TKE values are reduced significantly due to the air blowing with v_j = 60 m/s, while only slightly altered with v_j = 20 m/s. Comparing the slat noise level with the alteration of the TKE values, a clear relationship between them cannot be figured out.

Figure 3.12 shows the comparison of the values of p'_{rms} in the vicinity of the slat, and Figure 3.13 shows the comparison of the p'_{rms} values along the gap line for the three cases. The values of p'_{rms} near the trailing edge of the slat are slightly increased using v_j = 60 m/s, while no obvious effects are seen at v_j = 20 m/s. The values are lower in the v_j = 60 m/s case from the 6th monitor to the 18th monitor (corresponding to the leading edge of the main element) and from the 14th monitor to the 18th monitor in the v_j = 20 m/s case. Comparing the alteration of the slat noise level and the p'_{rms} values, it is found that the alterations are tightly related. The peak of the slat noise level at the frequency of 1 kHz is slightly increased, while the peak of the p'_{rms} values at around the 4th monitor is also slightly increased in the v_j = 60 m/s case. In addition, the slat noise levels at other frequencies are reduced, while the p'_{rms} values from the 6th monitor to the 18th monitor reduce too.

It has been shown that the locations of noise sources indicated by the variables, TKE, $\overline{|\omega_z|}$, $\overline{|\nabla \cdot L|}$ and p'_{rms} are different at some extend. The values of $\overline{|\omega_z|}$and $\overline{|\nabla \cdot L|}$ in the wake of the trailing edge of the slat in the case of v_j = 60 m/s are obvious higher than those in the absence of the airblowing. As shown in Figure 3.3b, large velocity gradient is generated at around the 7th monitor. This leads to high values of $\overline{|\omega_z|}$ and $\overline{|\nabla \cdot L|}$ in the wake of the trailing edge. However, since the distance from the surface of either the slat or the main element to the positions where high values of $\overline{|\omega_z|}$and $\overline{|\nabla \cdot L|}$ appear is large, the noise level is low. Because even the variable, $\overline{|\omega_z|}$ or $\overline{|\nabla \cdot L|}$, can be regarded as representative of noise sources, the large distance from any surface renders them behave like a quadruple source rather than a dipole. By contrast, high values of TKE appear merely in the attachment region, and high values of p'_{rms} in the attachment region and the region near the leading edge of the main element. It is suggested that the variables of $\overline{|\nabla \cdot L|}$, $\overline{|\omega_z|}$ are not suitable for addressing the noise sources, because the calculation of $\overline{|\nabla \cdot L|}$, $\overline{|\omega_z|}$ involves the mean values which are indirectly related with the noise generation. It is suggested that the variable p'_{rms} is the most suitable for addressing noise sources, because it has direct relationship with the noise in far-field. According to the contrast between the slat noise level in the far-field and the p'_{rms} values in the near-field, two conclusions can be derived:

a) The p'_{rms} values provide a more reasonable representation for the slat noise level than the variables of $|\omega_z|$, $|\nabla \cdot \mathrm{L}|$ and TKE.

b) The peak of the slat noise level at low frequencies (around 1 kHz in the study) in the far-field is related to the pressure fluctuations near the trailing edge of the slat.

3.2.4 Role of Air Blowing in Slat Noise Reduction

Two issues arise from the preceding comparisons amongst the variables associated with the three cases. One is the mechanism by which the TKE values in the vicinity of the slat significantly decrease in the case of v_j = 60 m/s. Another is that the peak of the p'_{rms} value near the trailing edge of the slat cannot be suppressed in the presence of the air blowing, although the main features of the mean flow field associated with the case of v_j = 60 m/s are nearly identical with those in the case of AOA = 12 degrees.

Figure 3.14 shows the POD basis functions of the pressure fluctuations in the vicinity of the slat at AOA = 8 degrees and u_∞ = 25 m/s associated with the cases of v_j = 20 and 60 m/s. It is found that the first mode associated with the case of v_j = 60 m/s is significantly altered when compared with that corresponding to the case of AOA = 8 degrees in the absence of the air blowing. According to the results, the pressure dipole, which occurs in the slat gap region, is suppressed due to the air blowing. As discussed in Chapter 2, the pressure dipole contains a significant portion of the energy of the pressure fluctuations. It can be conjectured that intense velocity fluctuations should be produced when the pressure dipole is active. Since the pressure dipole is suppressed in the case of v_j = 60 m/s, the velocity fluctuations should be correspondingly decreased (shown in Figure 3.11). No obvious alteration can be seen for the first mode in the case of v_j = 20 m/s when compared with the case of v_j = 0 m/s. Correspondingly, the difference of the TKE values between the cases of v_j = 0 and 20 m/s (shown in Figure 3.11) is not obvious. Therefore, the alteration of the TKE values associated with various v_j is related with the first mode of the pressure fluctuations.

For the second mode, the pressure fluctuations associated with the case of v_j = 60 m/s are slightly increased (shown in Figure 3.14). As representatives, the highest values of p'_{rms} in the interaction regions are -2.14, -1.62 and -2.24 corresponding to AOA = 8 or 12 degrees and v_j = 60 m/s respectively. The value in the case of AOA = 12 degrees is much lower than the others, while the slat noise level in the far-field at AOA = 12 degrees is much lower than the others too. It has been shown that the slat noise level in the far-field has a close relationship with the pressure fluctuations in the reattachment region, and the pressure fluctuations in the reattachment region and in the interaction regions are spatially cross-related. Therefore, the slat noise level is related with the values of p'_{rms} in the interaction region associated with the second mode. For example, the highest values of p'_{rms} in the interaction region are -2.14 and -2.24 corresponding to the cases of AOA = 8 degrees and v_j = 60 m/s respectively, whilst the highest noise level at a frequency of around 1 kHz, corresponding to the case of v_j = 60 m/s, is slightly higher than that corresponding to the case of AOA = 8 degrees (shown in Figure 3.7). Provided that the highest p'_{rms} value in the interaction region is regarded as a reference for the interaction intensity, the interaction is seen to be most intense in the case of v_j = 60 m/s, followed by the case of AOA = 8 degrees, and weakest in the case of AOA = 12 degrees. That is not expected; the interaction was expected to be weakened by the air blowing.

As mentioned above, the size of the circulation region has an important effect on the interaction. The size determines the position where the interaction occurs. As the position moves away from the surface of the main element, the interaction becomes weak. As shown in Figure 3.14 associated with the mode 2, the interaction position in the case of v_j = 20 m/s has no obvious alteration when compared with the case of AOA = 8 degrees (shown in Figure 2.38), but the position of the highest value near the trailing edge moves slightly away from the surface of the slat cove (shown in Figure 3.13). This results in a readable reduction in the slat noise. It is known that a noise source radiates weak noise when positioned away from a solid surface. In the case of v_j = 60 m/s, the interaction position moves to a distance of $0.12c_s$ away from the surface of the main element, or $0.106c_s$ in the absence of the air blowing. The alteration of the interaction position is as expected. However the highest value of the p'_{rms} in the interaction region is not decreased by the air blowing. This is assumed to result from the fact that the mean pressure in the slat gap region in the case of v_j = 60 m/s is much lower than that associated with the case of AOA = 12 degrees, whilst the mean velocity in the gap region is far higher. If the pressure fluctuations are non-dimensioned by the local dynamic pressure (for example, the dynamic pressure at the 10th monitor), the non-dimensioned values of p'_{rms} associated with the three cases of AOA = 8 and 12 degrees and v_j = 60 m/s are 1.37, 0.763 and 0.614 respectively. The latter two values are close, and much lower than the former. In this respect, the interaction is seen to be suppressed by the air blowing.

3.3 Summary

Air blowing employed on the suction surface of the slat near the trailing edge was numerically tested. Several conclusion can be derived according the results:

a) The wing performance can be improved using the airblowing, wherein the lift of the wing is increased by approximately 34 percent, whilst drag is decreased by approximately 271 percent when the airblowing velocity magnitude is set to 60 m/s.

b) The size of the circulation region in the slat cove can be obviously reduced using the airblowing, and the flow velocity through the gap increased.

c) The computed results show that the slat noise levels over most of the frequencies, especially above a frequency of 2 kHz (corresponding to a *St* number of approximately 5), are attenuated using the air blowing. A higher velocity magnitude of air blowing achieves higher noise reductions in the slat noise. However the peak of the slat noise spectrum, which appears at a frequency of around 1 kHz, is not attenuated.

d) The TKE values in the reattachment region decreased significantly when a high velocity magnitude of the air blowing was used. That effect resulted from the suppressed first mode of the pressure fluctuations. Although the non-dimensionalized pressure fluctuations (based on the local dynamic pressure) indicated that the interaction is weakened by the air blowing, the peak of the magnitude of the pressure fluctuations was not obviously reduced. This leads to the peak of the slat noise level not being attenuated.

Table 3.1: Effects of air blowing on the lift and drag coefficients

v_j (m/s)	c_l	$\Delta c_l/c_l$(%)	c_d	$\Delta c_d/c_d$ (%)
0	1.688	0	0.0725	0
20	1.836	8.6	0.0017	97.6
60	2.268	34.4	-0.124	271

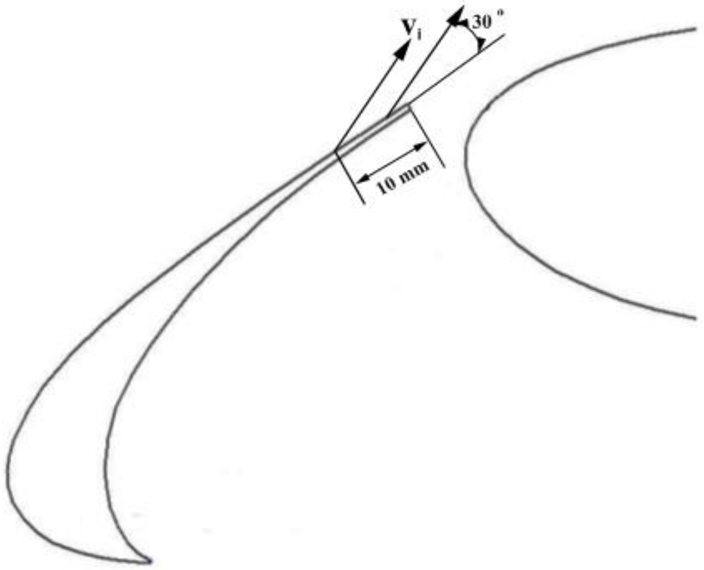

Figure 3.1: Schematic of the air blowing onto the surface of slat.

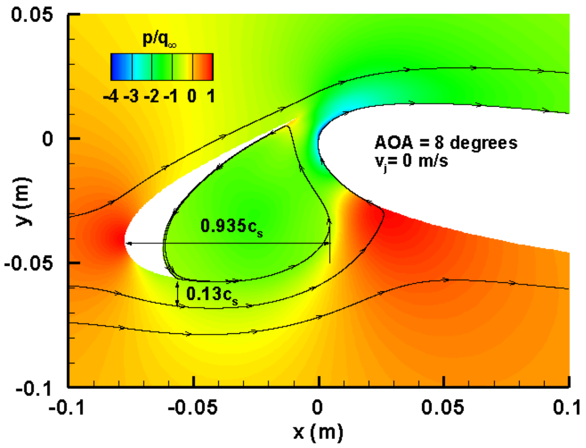

a) v_j = 0 m/s.

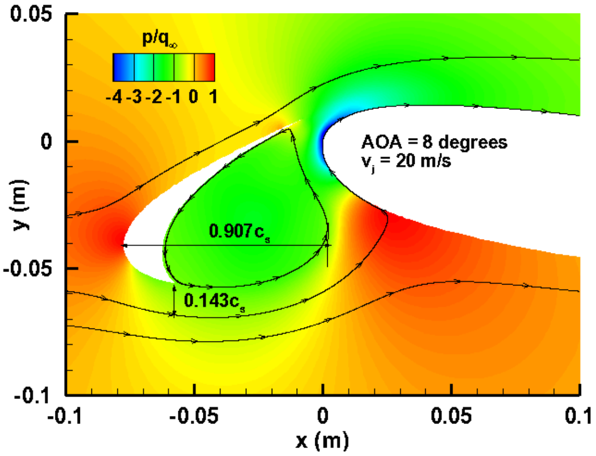

b) v_j = 20 m/s.

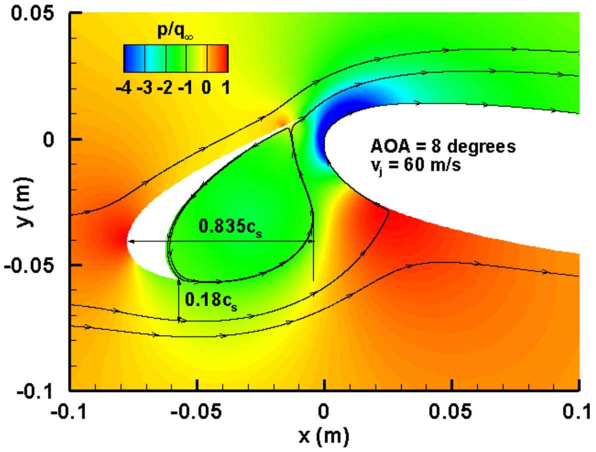

c) v_j = 60 m/s.

Figure 3.2: Size of circulation region and width of flow channel associated with various velocity magnitudes of air blowing at AOA = 8 degrees, u_∞ = 25m/s.

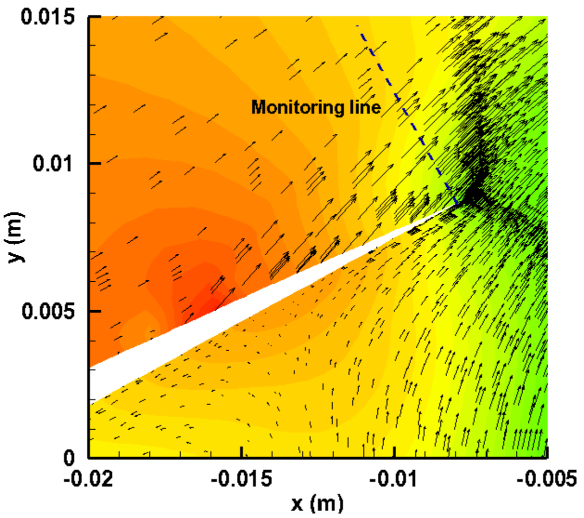

a) Close-up view of the velocity near the trailing edge, the first monitor is located close to the surface.

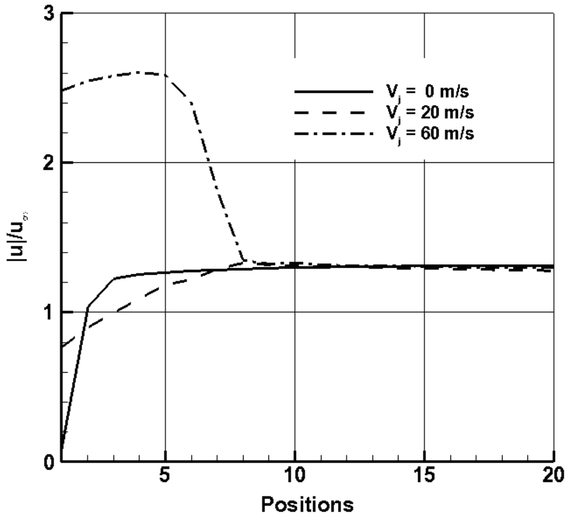

b) Comparison of mean velocity distribution along the monitoring line.

Figure 3.3: Close-up view of the velocity near the trailing edge of the slat and the comparison of mean velocity distribution along the monitoring line at various airblowing velocities.

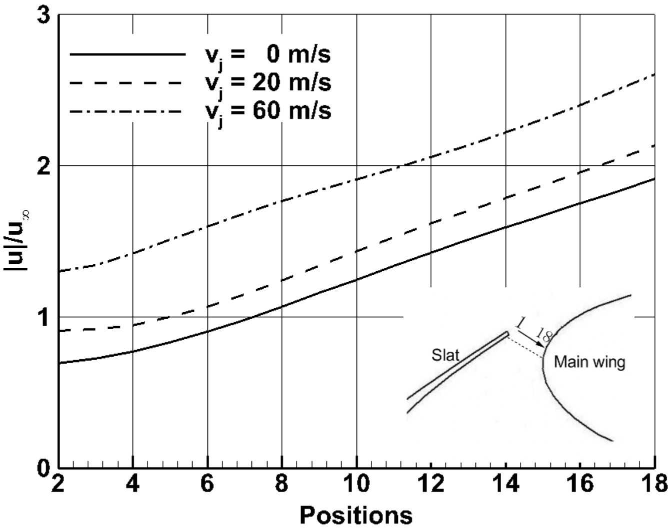

Figure 3.4: Comparison of mean velocities along the gap line amongst various air blowing velocities at AOA = 8 degrees, u_∞ = 25m/s.

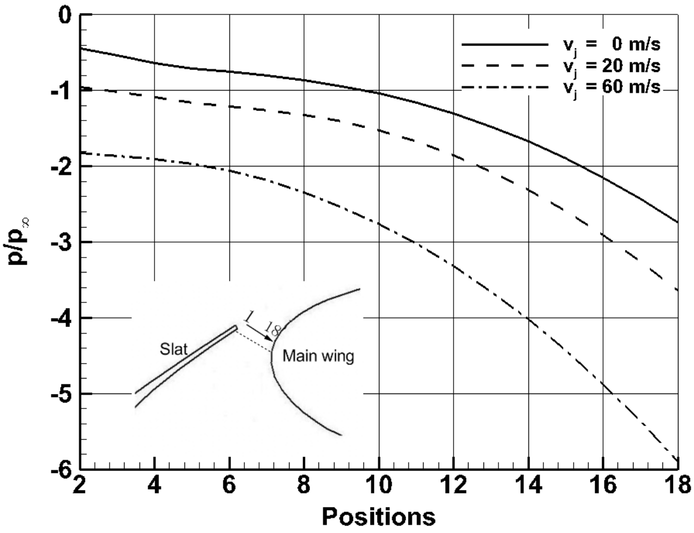

Figure 3.5: Comparison of mean static pressure along the gap line amongst various air blowing velocities at AOA = 8 degrees, u_∞ = 25m/s.

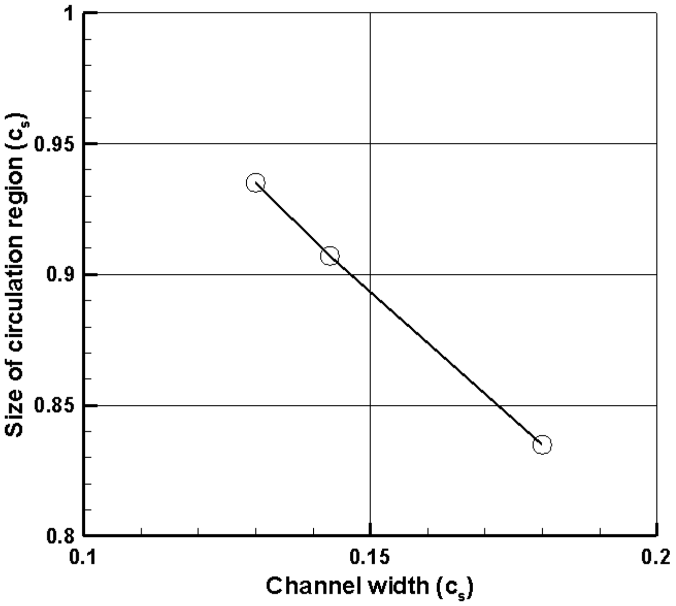

Figure 3.6: Relationship between the cusp channel width and the sizes of the circulation region.

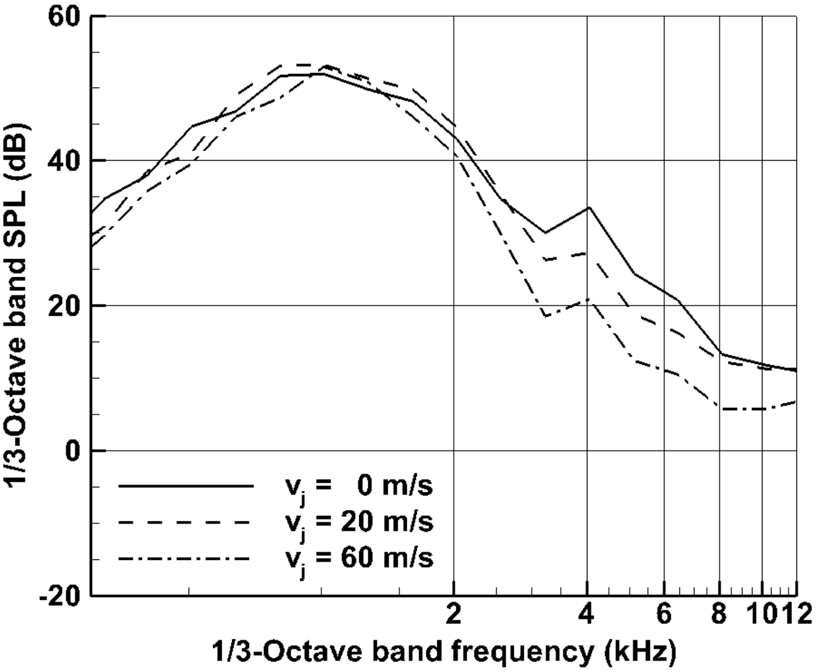

Figure 3.7: Comparison of 1/3 octave band SPLs at various blowing velocities.

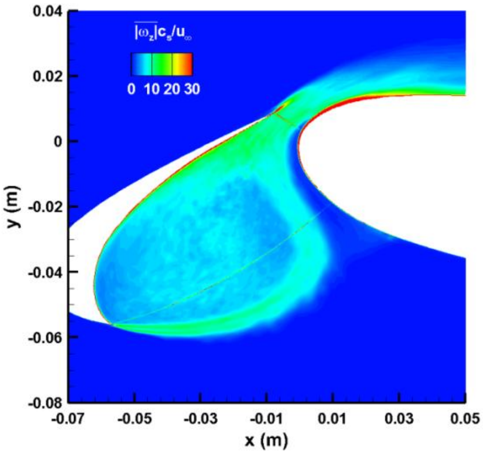

a) v_j = 0 m/s.

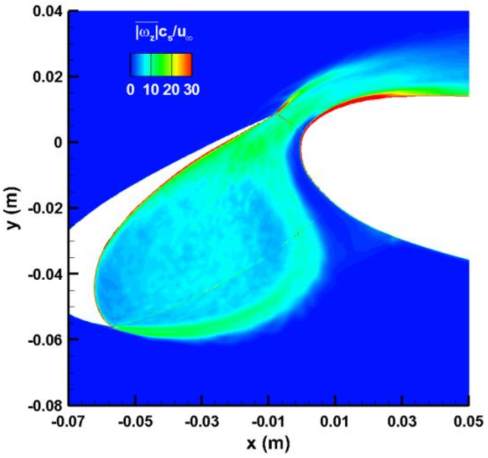

b) v_j = 20 m/s.

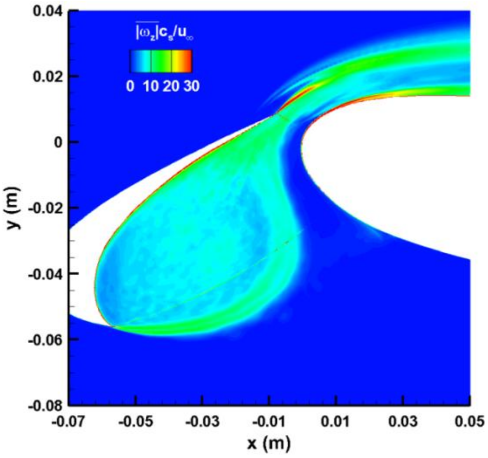

c) v_j = 60 m/s.

Figure 3.8: Comparison of $|\omega_z|$ amongst various blowing velocities cases at AOA = 8 degrees, u_∞ = 25m/s.

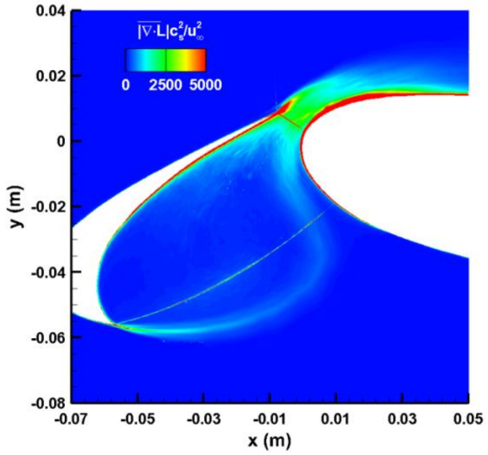

a) v_j = 0 m/s.

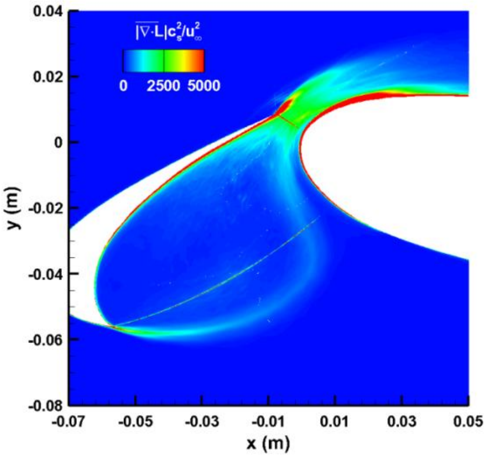

b) v_j = 20 m/s.

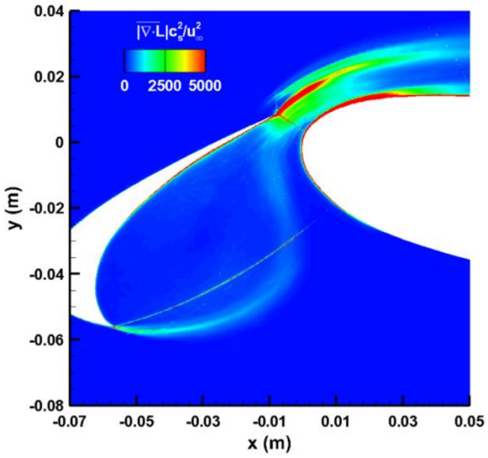

c) v_j = 60 m/s.

Figure 3.9: Comparison of $|\nabla \cdot L|$ amongst various blowing velocities cases at AOA = 8 degrees, u_∞ = 25m/s.

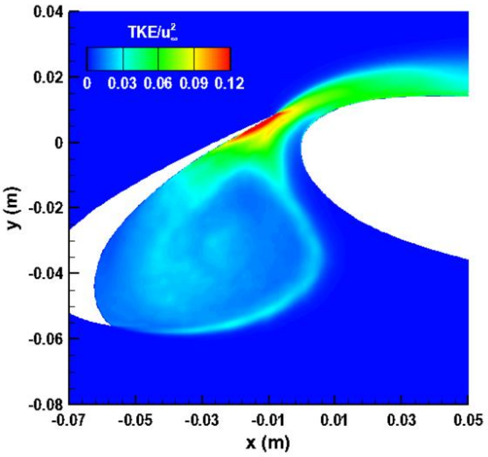

a) v_j = 0 m/s.

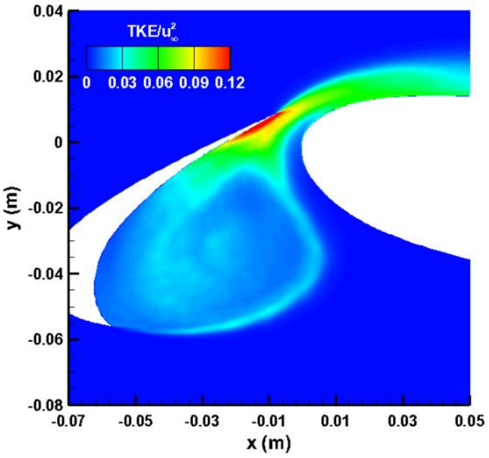

b) v_j = 20 m/s.

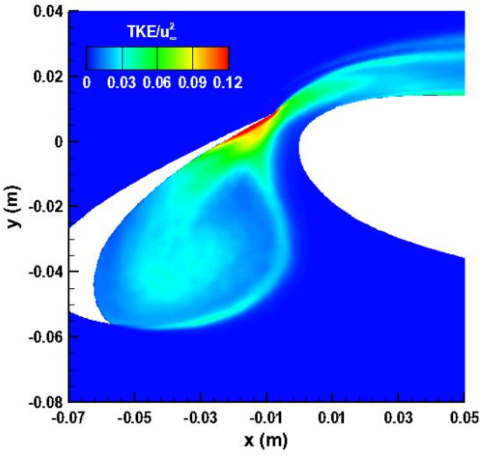

c) v_j = 60 m/s.

Figure 3.10: Comparison of TKE amongst various blowing velocities cases at AOA = 8 degrees, u_∞ = 25m/s.

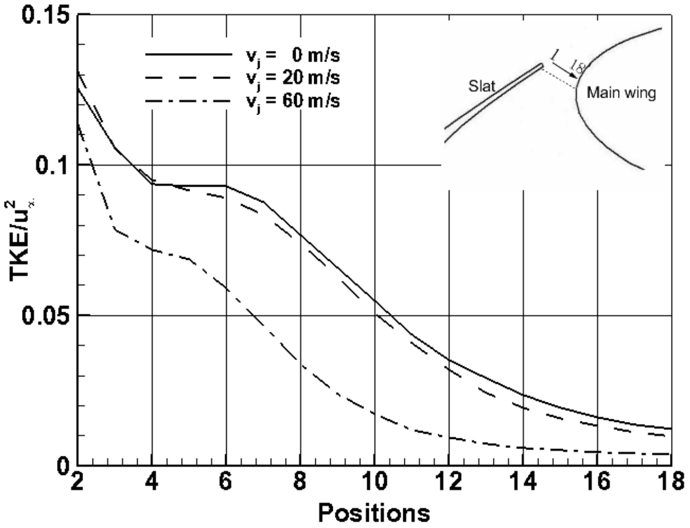

Figure 3.11: Comparison of TKE values along the gap line amongst various blowing velocities cases at AOA = 8 degrees, u_∞ = 25m/s.

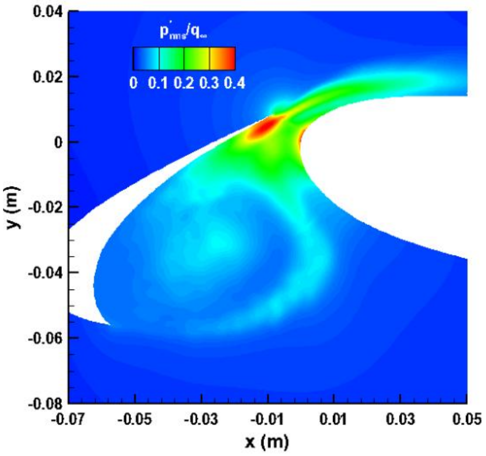

a) v_j = 0 m/s.

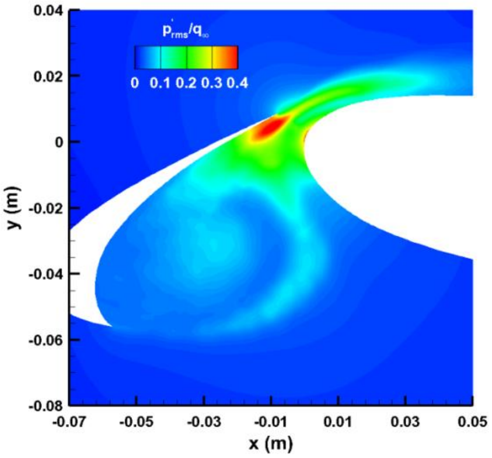

b) v_j = 20 m/s.

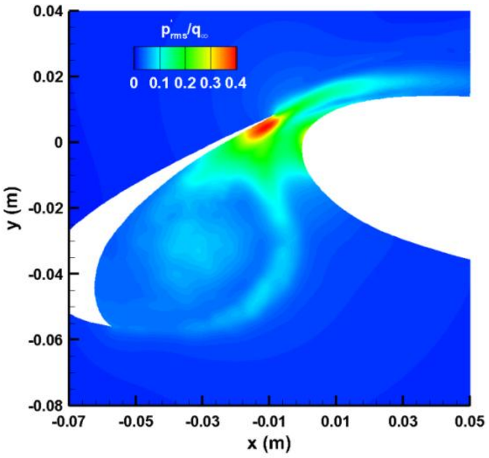

c) v_j = 60 m/s.

Figure 3.12: Comparison of p'_{rms} amongst various blowing velocities cases at AOA = 8 degrees, u_∞ = 25m/s.

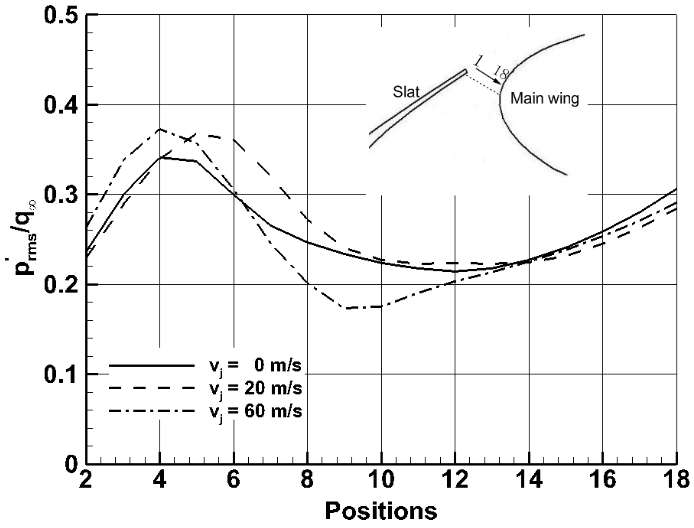

Figure 3.13: Comparison of p'_{rms} values along the gap line amongst various blowing velocities cases at AOA = 8 degrees, u_{∞} = 25m/s.

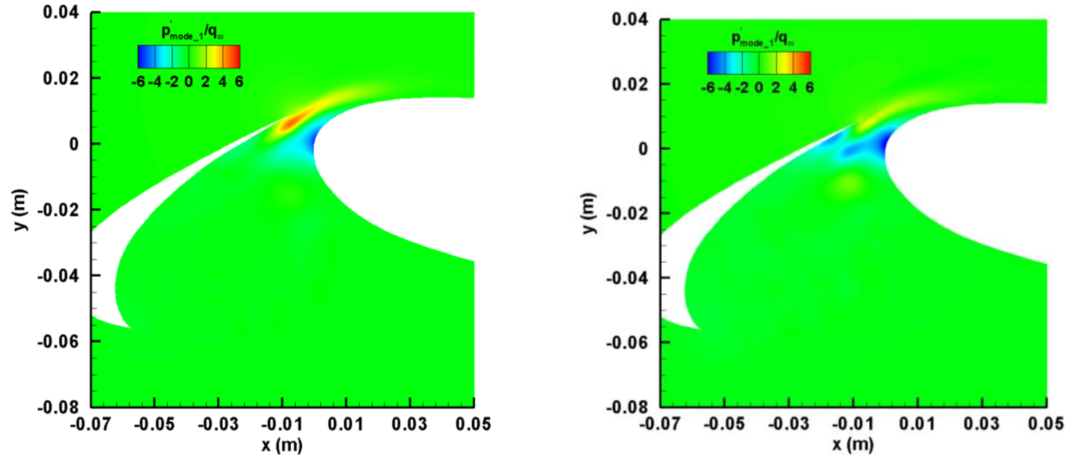

Mode 1 Mode 1

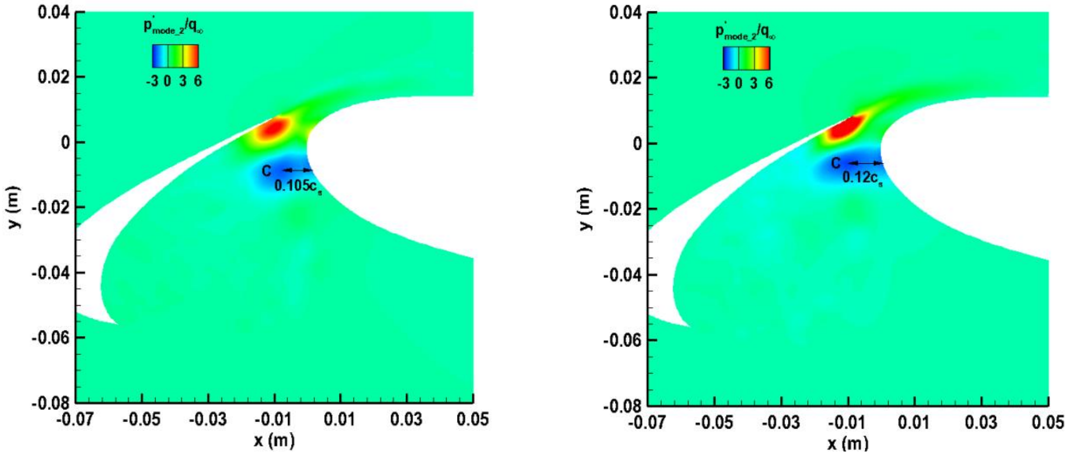

Mode 2 Mode 2

Figure 3.14: Comparison of basis function of pressure fluctuation between the cases of v_j = 20 m/s and v_j = 60 m/s at AOA = 8 degrees, u_∞ = 25m/s.

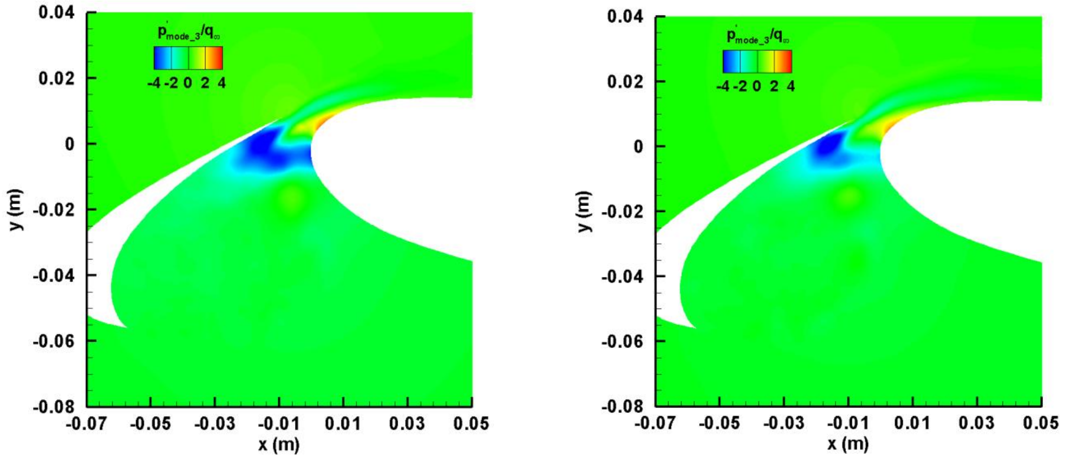

Mode 3 Mode 3

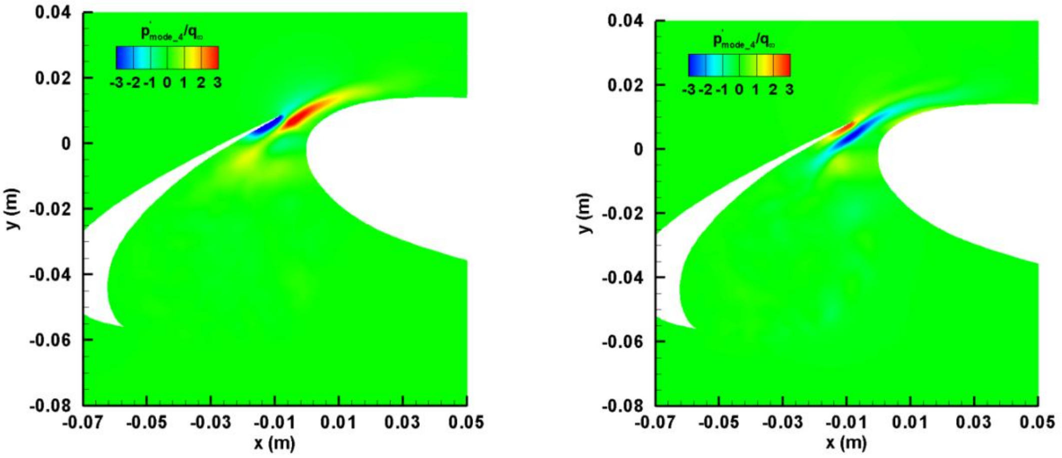

Mode 4
a) v_j = 20 m/s.

Mode 4
b) v_j = 60 m/s.

Figure 3.14: Comparison of basis function of pressure fluctuation between the cases of v_j = 20 m/s and v_j = 60 m/s at AOA = 8 degrees, u_∞ = 25m/s.

Chapter 4

Slat Noise Reduction with a Leading Edge Strip

4.1 Introduction

Based on the understanding of the slat noise generation discussed in Chapter 2, a passive method of attenuating slat noise was proposed. It has been shown that the interaction between the shear layer shedding off the slat cusp and the flow convected from the stagnation line on the main element dominates the generation of slat noise. This approach, wherein a strip was mounted on the pressure surface of the main element close to the interaction region, was expected to weaken this interaction. Consequently, the slat noise could be attenuated. The method was both numerically and experimentally investigated.

In the experiment, the AOA was set to 8 degrees and the freesteam velocity was set to 25 m/s, which corresponded to a *Re* number of approximately 5.7×10^5 (based on the main element chord). Microphone measurements showed that the inclusion of the strip led to a significant attenuation of slat noise in both the near- and far-field. The fluctuating velocity spectrum measured by a hot-wire anemometer in the slat gap region showed that the peak of the fluctuating velocity spectrum, which occurred at a frequency of 75 Hz, disappeared. The numerical results show that the values of TKE, vorticity, Lamb vector and the pressure fluctuations all decreased when the strip was attached. Furthermore the modes of the POD of the pressure fluctuations showed the first mode, corresponding to the pressure dipole in the gap region, and the second mode, corresponding to the interaction, were both suppressed when the strip was included. However the strip also resulted in a slight reduction in the aerodynamic lift force.

4.2 Setup

The model used during testing was the same one as shown in Figure 2.1. To reduce the slat noise, a strip was mounted on the main element surface near the leading edge (shown in Figure 4.1). The influence of the strip location was also examined. For the first position, the distance in the chord direction from the leading edges of the main element to the strip was 3.5 mm (corresponding to approximately $0.04c_s$). The distances for the second and third positions corresponded to $0.091c_s$ and $0.142c_s$ respectively. The strip had a width of 10 mm and the height was adjustable. The span of the strip was identical to that of the main element. The AOA was set to 8 degrees and the freesteam velocity was set to 25 m/s, which corresponded to a *Re* number of approximately 5.7×10^5 (based on the main element chord).

The acoustic experiments were conducted in the anechoic chamber at the University of Southampton. The chamber measures 9.15 m × 9.15 m × 7.32 m without wedges, and free-field conditions exist at frequencies above 80 Hz. The chamber is equipped with a jet nozzle with a height of 540 mm and a width of 350 mm. The maximum attainable wind velocity is approximately 31 m/s. A Behringer ECM 8000 microphone was used to measure the far-field noise. Figure 4.2 shows the microphone measurement setup. The distance between the microphone and the slat model was 2.5 m, which corresponded to a distance of $28.4c_s$ or to 7.35 wavelengths of 1 kHz sound wave, and the observation angle was 280 degrees. The slat noise was measured by this microphone at a sampling rate of 30 kHz and a sampling time of 16 s. The microphone signal was pre-amplified and filtered before being converted to a digital signal by a dSPACE A/D converter, where the filter had a low pass frequency of 9.5 kHz.

The setup of the numerical simulation was the same as that introduced in Chapter 2. Figure 4.3 shows the grids in the vicinity of the slat for the numerical simulation. A strip with a height of 2 mm situated at the first position was plotted in the grids. The far-field noise was calculated by an integral solution of the FW-H equation and the corresponding integration surfaces are shown in Figure 2.6.

4.3 Results and Discussions

The flow features in the wake of the stripe was first checked. Figure 4.4 presents the comparison of the mean velocity and the TKE values along the monitor line (shown in Figure 4.3) between with and without the strip. The monitor line, which is located on the mid-span plane, has a length of approximately 4 mm (corresponding to $0.045c_s$) and is perpendicular to the surface of the main element. The distance from the trailing edge of the strip to the monitor line is around 4 mm. 20 monitors in total are uniformly collocated on the monitor line. As shown in Figure 4.4, in the case of inclusion of the strip, the mean velocities at monitors from 2 to 8 are decreased significantly, especially the case for the monitors close to the surface of the main element. This results from flow separation at the trailing edge of the strip, and a 'dead' flow region is formed in the wake of the strip. A peak of TKE value appears at 5th monitor. It is assumed that a free shear is shed from the trailing edge of the strip. However, the shear layer is intrinsically unstable, and quickly rolls up into discrete vortex. Consequently, large TKE values are generated on the path of the free shear moving.

4.3.1 Mean Aerodynamic Features

The computed lift coefficient was 1.68 without the strip and 1.51 with the strip at AOA = 8 degrees and u_∞ = 25 m/s. The inclusion of the strip resulted in a lift coefficient drop of approximately 10 percent. So clearly the mounted strip adversely affects the aerodynamic performance of the wing.

Figure 4.5 shows the comparison of the computed mean velocity field around the slat. It is clear that, due to the strip, the size of the circulation region becomes larger and the width of the cusp flow channel is reduced. The two sizes tended towards those associated with the case of AOA = 6 degrees. As discussed in Chapter 2, the slat noise level became low as the size of the circulation region was either larger or smaller than the size at AOA = 8 degrees. Therefore, it was expected that the slat noise level could be alleviated with the inclusion of the strip.

Figure 4.6 shows the comparison of the computed mean velocity and static pressure along the gap line. The mean velocities close to the slat decreased due to the strip but the velocity slope remained unchanged. However the mean velocities close to the main element decreased significantly and the trend was changed. Meanwhile, it could be observed that the velocity slope in the presence of the strip was significantly different from that associated with the case of AOA = 6 degrees. This implies that in the case with the strip attached, a typical circulation region still existed. This is unlike the case at AOA = 6 degrees where the circulation region was not formed. The mean static pressures close to the slat were not affected in any obvious way. But the mean static pressures close to the main element increased significantly. The increase of the static pressures close to the main element inevitably led to the loss of the leading edge suction force, and consequently resulted in the drop of the lift coefficient.

4.3.2 Effects of the Strip on Slat Noise

Effect of strip position

The measurements were conducted in the anechoic chamber, the velocity of the freestream was set to 25 m/s and the AOA was set to 8 degrees. Figures 4.6a and 4.6b illustrate the reductions in the slat noise in the one-third octave bands in the far- and near-fields respectively due to the strip. In this instance, the strip had a height of 2 mm and a width of 10 mm. The strip, at all three positions, reduced the far-field slat noise level by approximately 1-4 dB in a frequency range from 0.2 kHz to 2.5 kHz. However, above a frequency of 2.5 kHz the reduction was no longer present. By contrast, the strip resulted in an obvious reduction throughout the entire frequency range in the near- field. The reason for this difference is that the far-field microphone measures the noise generated by the entire wing, while the near-field microphone is dominated by the noise generated in the vicinity of the slat. Therefore, the reduction in the near-field provides a better insight into the effect of the strip, although the reduction in the far-field is the main goal in attenuating slat noise. According to the measurements, the noise in the far-field has its peak at a one-third octave frequency of 400 Hz, which corresponds to a *St* number of 1.4 based on the slat chord. This value is within the range of *St* numbers reported in both model and full-scale studies of slat noise[31].

Effect of Strip Height

Figures 4.8a and 4.8b show the effect of strip height on the slat noise in the near- and far-field respectively, with the strip located at position 2. The far-field noise could be reduced by the strip at frequencies less than 2.5 kHz. However, above this frequency the noise attenuation was not obvious. This phenomenon is particularly evident with a strip height of 3 mm. According to the measurements in the far-field (shown in Figure 4.8b), a higher strip could achieve a larger reduction.

4.3.3 Effects of the Strip on Slat Noise Sources

Figures 4.9 and 4.10 show the comparisons of the computed values of $\overline{|\omega_z|}$ and $\overline{|\nabla \cdot L|}$ in the vicinity of the slat between the 'inclusion' and 'exclusion' strip cases. The only obvious difference between the two cases is that significantly higher values appear in the wake of the strip. This resulted from the fact that high velocity gradients are generated in the wake of the strip. If the two variables can represent the noise sources of the slat, the flow in the wake should be a dominant noise source and the slat noise level in the presence of the strip should be higher than that in the absence of the strip. However, this does not agree with the experimental measurements, in which the noise level in the presence of the strip was lower. As discussed in Chapter 2, the two variables could not directly represent the strength of the noise sources. Figure 4.11 illustrates the comparison of the computed TKE values in the vicinity of the slat and Figure 4.12 shows the values along the gap line. It can be observed that the TKE values in the reattachment region decreased significantly, while a peak again appeared at around the 6th monitor. Although large values of $\overline{|\omega_z|}$ and $\overline{|\nabla \cdot L|}$ appear in the wake of the strip, the TKE values in the wake of the strip are not large when compared to the values in the reattachment region. Nonetheless, in terms of the values of $\overline{|\omega_z|}$ and $\overline{|\nabla \cdot L|}$, the flow in the wake of the strip is the dominant noise source. However, the values of TKE indicate the flow in the reattachment region is the dominant noise source. The locations of the noise sources indicated by these variables are thus not in accordance. Therefore, attention should be paid to the variables used to represent the noise sources, especially when more than one potential noise source simultaneously exists in one domain.

Figure 4.13 shows the comparison of the values of p'_{rms} along the gap line and Figure 4.14 shows the comparison of the values of p'_{rms} in the vicinity of the slat. In both cases, either absence or presence of the strip, large values appear in the reattachment region and in the region close to the leading edge of the main element. The values associated with the strip attached case are obviously lower than those in the case without the strip. The peak of the values in the absence of the strip appears at the 5th monitor, compared to the 6th monitor in the presence of the strip. This means that the noise source is deviated away from the cove surface due to the strip. It is known that a noise source near a solid surface is a better acoustic radiator than that away from a solid surface. Therefore, the slat noise level was attenuated by the strip owing to two facets: that the p'_{rms} values decrease and that the peak of the values deviates away from the cove surface.

Pressure fluctuations modes

The pressure fluctuations in the vicinity of the slat in the presence of the strip were decomposed using the POD techniques. Figure 4.15 shows the comparison of eigenvalues of the first 30 modes. The values before the 15th mode all decrease significantly. For example, the eigenvalue of the first order reduces from 2.4×10^{10} to 1.2×10^{10}. This means that the energy contained in the first mode in the presence of the strip is only half of that in the absence of the strip. Figure 4.16 shows the comparison of the time history of the pressure fluctuations of the first mode at point A (shown in Figure 4.14b). It can be seen that the most intense pressure fluctuations are suppressed due to the strip, and the non-dimensionalized p'_{rms}value decreases from 0.36 to approximately 0.20.

Figure 4.17 shows the comparison of the first four basis functions associated with the cases with and without the strip. It can be observed that the first basis functions associated with the two cases display similar behaviour. However, the values in the presence of the strip are lower than the results without the strip, and the large values near the trailing edge of the slat are further from the surface when compared with the case with the strip. The second basis function is obviously altered when the strip is attached. In the absence of the strip, the pressure fluctuations in the reattachment region and the interaction region are spatially cross-related. However in the presence of the strip, the spatial cross-relation is interrupted by the strip. This can be confirmed by the following evidence. Firstly, the values of the pressure fluctuations in both the reattachment region and the interaction region decrease due to the strip. Secondly, the position corresponding to the highest value in the interaction region is slightly moved away from the surface of the main element due to the strip; $0.106c_s$ in the absence of the strip and $0.113c_s$ in the presence of the strip, as shown in Figure 4.17. Finally, in the second mode associated with the case with the strip, the largest negative value of the pressure fluctuation occurs near the leading edge of the main element rather than in the interaction region. The reduced values of the pressure fluctuation in the interaction region indicate that the strength of the interaction becomes weak. It has been discussed previously that the intermittently generated vortical structures and the flow oscillation in the slat cove are the consequence of this interaction. In view of the oscillation system, the flow oscillation in the slat cove behaves as a self-sustained system when no external forces act on it. As sufficient disturbances generated by the strip externally act on the system, the system turns into a forced oscillation system and its oscillation becomes weak. This is the crucial role of the strip in the reduction of the slat noise. The third and fourth basis functions in the presence of the strip are no longer similar to their counterparts according to the results shown in Figure 4.17. However, the underlying mechanisms are not yet fully understood.

Velocity fluctuations in the gap region

Figure 4.18 illustrates the comparison of the fluctuating velocity spectrum measured using the hot wire anemometer at point 3 (shown in Figure 2.29) between the cases of absence and presence of the strip. It can be seen that the strip suppresses the fluctuating velocity peak appearing in the spectrum at a frequency of 75 Hz. The fluctuating velocities at other frequencies are decreased as well. The experimental measurements are in accordance with the computed results (shown in Figure 4.1), wherein the computed results show that the TKE values close to the cove surface decrease due to the strip. Although the variables of TKE and velocity fluctuation are not the same, both can represent the fluctuating component in velocity. The disappearance of the peak implies that the pressure dipole, which occurs in the gap region, is suppressed due to the strip.

4.4 Summary

A strip mounted on the pressure surface of a main element was experimentally proven to be an effective method for reducing the broadband slat noise at an angle of attack of 8 degrees and a freestream velocity of 25 m/s. The position and height of the strip had an influence on the reduction to some extent. The computed results show that the mean flow fields associated with the two cases, the absence and presence of the strip, were similar but the size of the circulation region was slightly increased by the addition of the strip. The static pressure near the leading edge of the main element also increased due to the strip. This led to a reduction in the lift coefficient of approximately 10 percent. The pressure fluctuations in the vicinity of the slat were significantly decreased by the strip. The POD analysis of the pressure fluctuations showed that the values of the first basis function decreased. This implied that the pressure dipole, which occurs in the slat gap region, was suppressed. The second basis function was also fundamentally altered by the strip. This implied that the

intermittently generated vortical structures and the flow oscillation in the slat cove were suppressed too. The flow oscillation in the slat cove can be regarded as a self-sustained system containing multiple modes when no external forces act on it. As sufficient disturbances externally acted on the system, the system turned into a forced oscillation system and its oscillation became weak. Consequently, the slat noise level was attenuated.

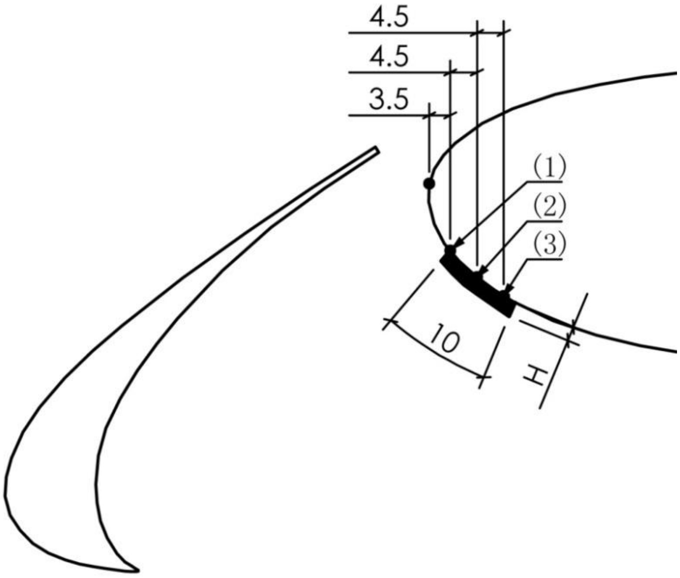

Figure 4.1: Three positions of the strip. The dimensions are in mm.

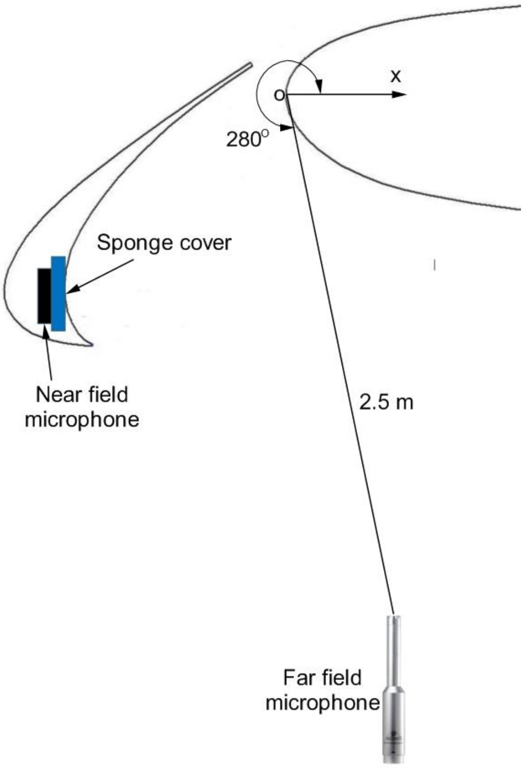

Figure 4.2: Positions of the near-field and far-field microphones.

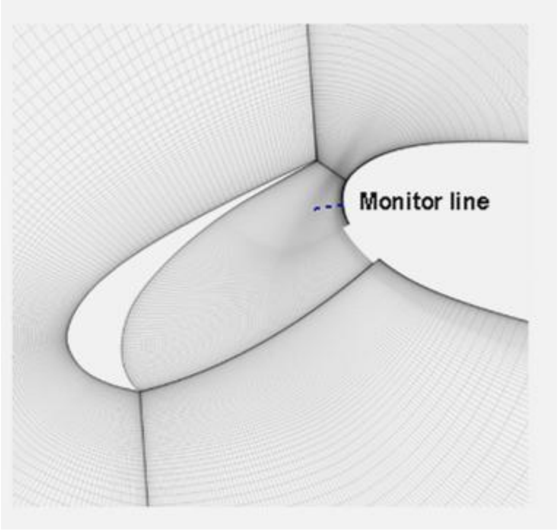

Figure 4.3: Grids in the vicinity of the slat, 20 monitors with equal spacing are collocated along the monitor line which is on the mid-span plane.

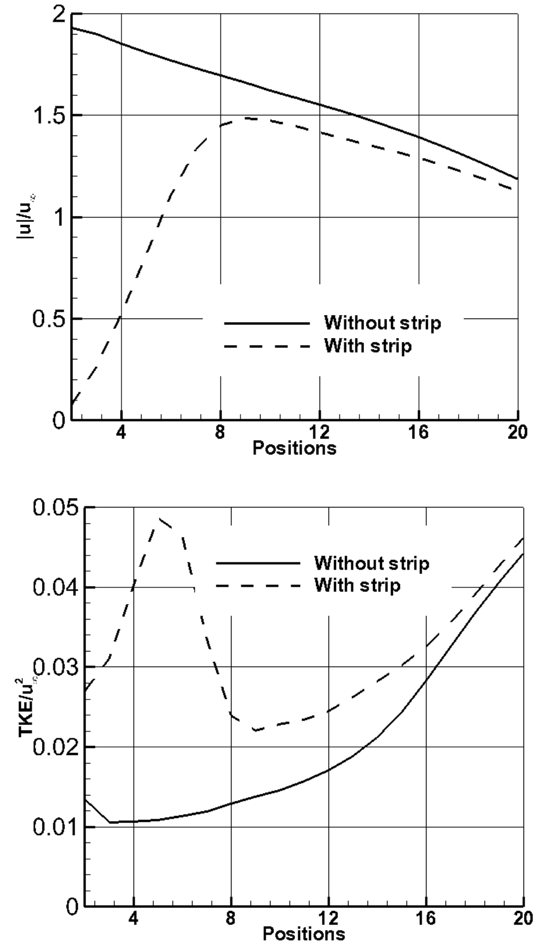

Figure 4.4: Mean and TKE distribution along the monitor line (shown in Figure 4.3). The 1st number index is close to the surface of main element.

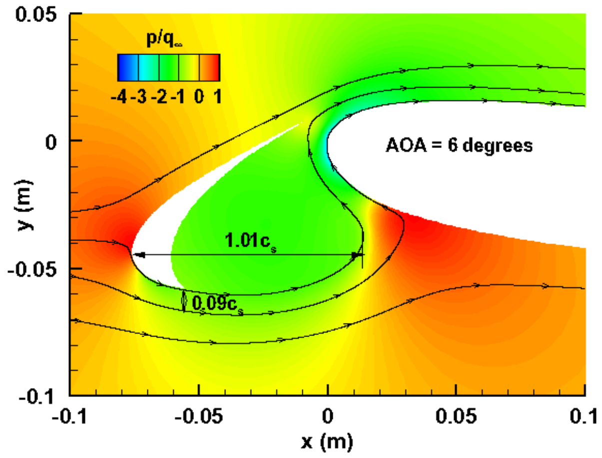

a) AOA = 6 degrees.

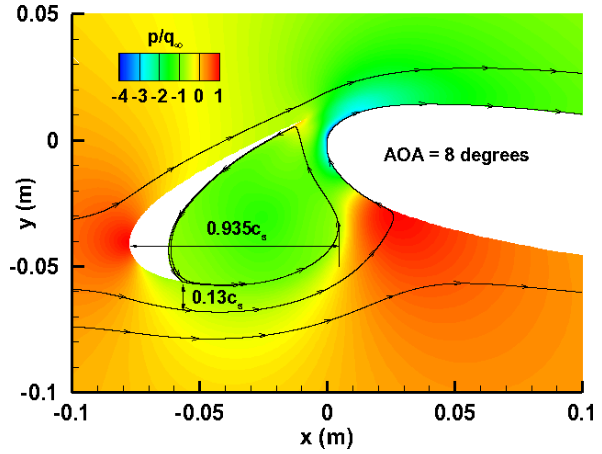

b) AOA = 8 degrees in the absence of strip.

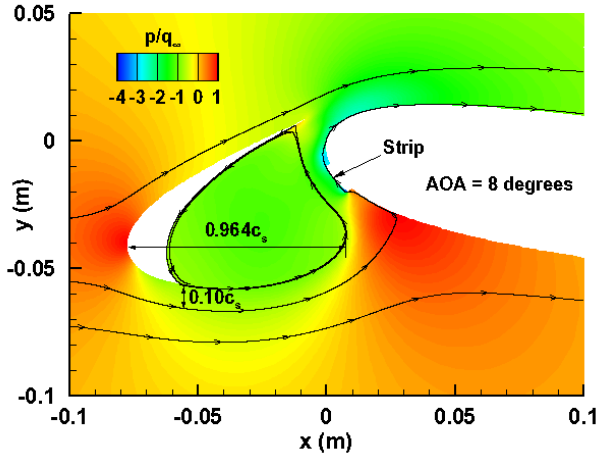

c) AOA = 8 degrees in the presence of strip.

Figure 4.5: Comparison of computed mean velocity and static pressure around the slat at u_∞ = 25 m/s.

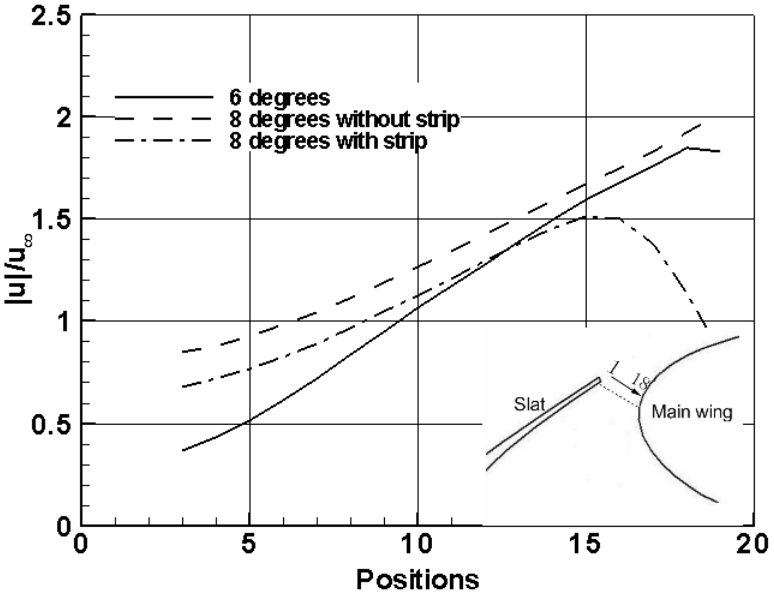

a) Mean velocity magnitude along the gap line.

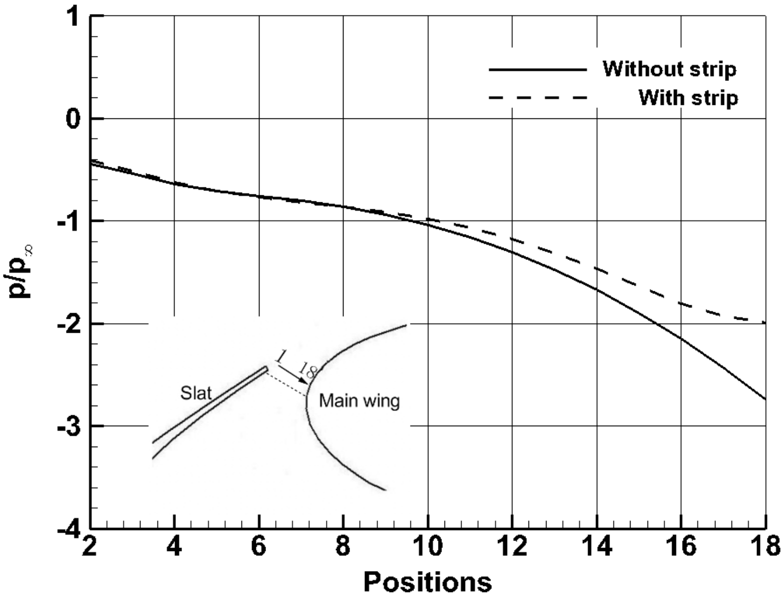

b) Mean static pressure along gap line.

Figure 4.6: Computed mean velocity magnitude and static pressure along the gap line at AOA = 8 degrees, u_∞ = 25 m/s.

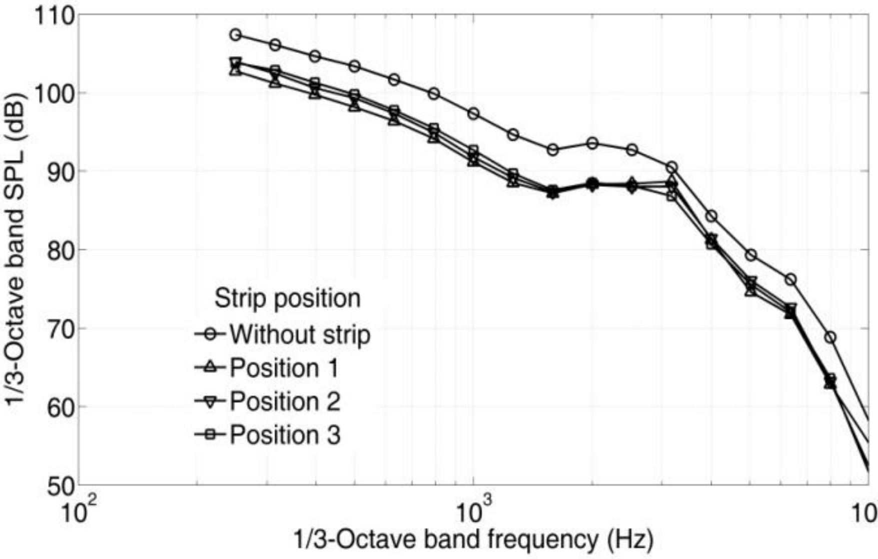

a) Near-field microphone.

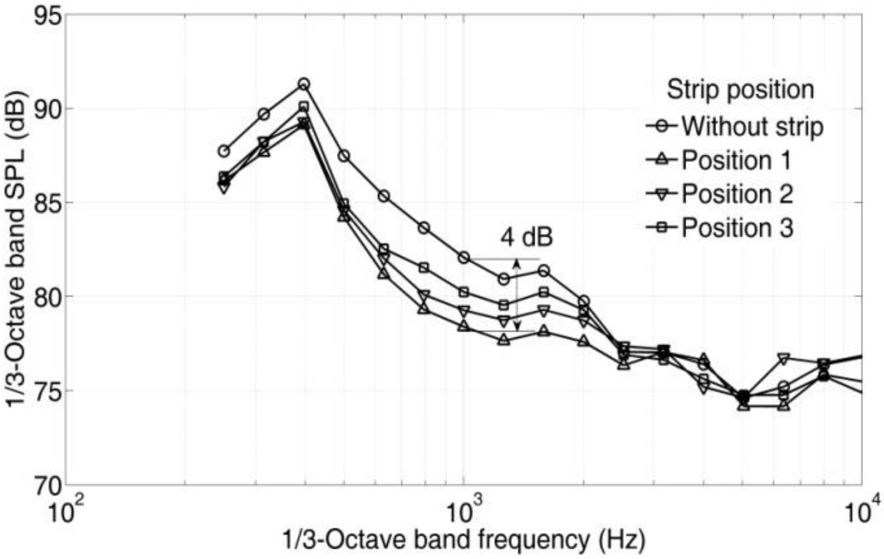

b) Far-field microphone.

Figure 4.7: Effects of strip positions on slat noise. Strip height = 2mm, AOA = 8 degrees, u_∞ = 25 m/s.

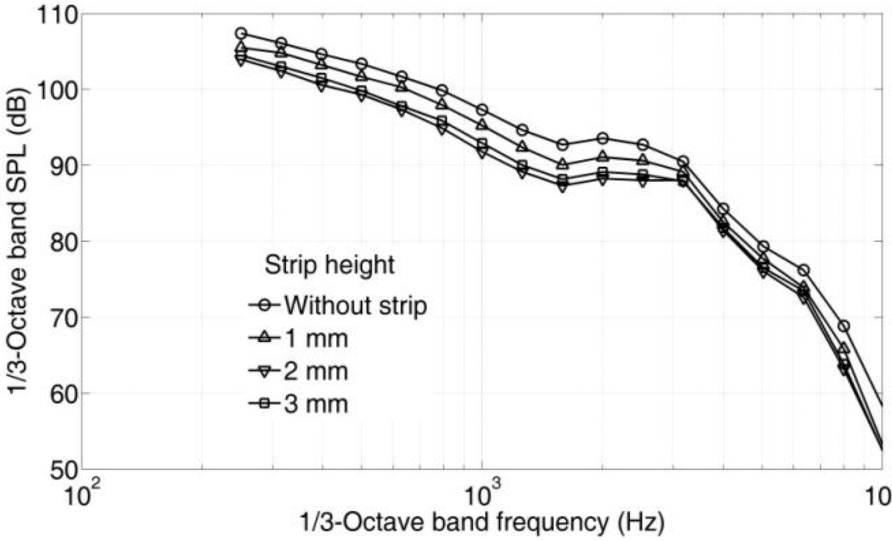

a) Near-field microphone.

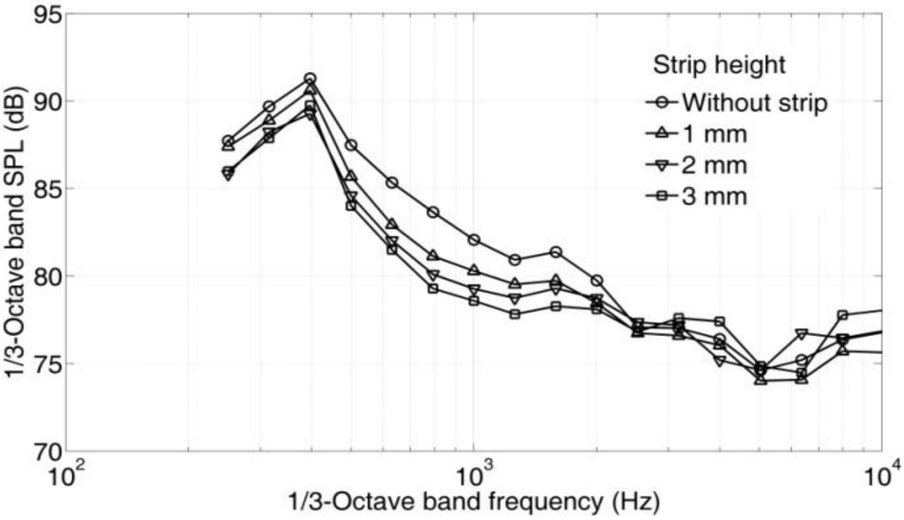

b) Far-field microphone.

Figure 4.8: Effect of strip height on slat noise reduction at AOA = 8 degrees, u_∞ = 25 m/s. Strip at position 2.

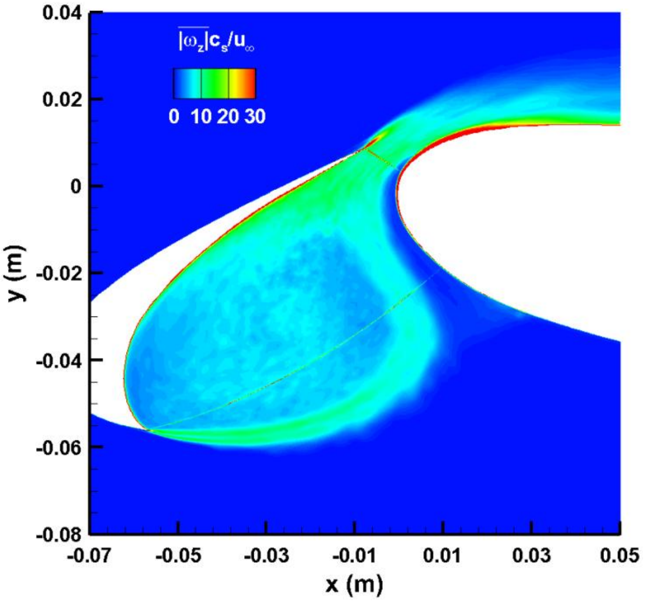

a) In the absence of strip.

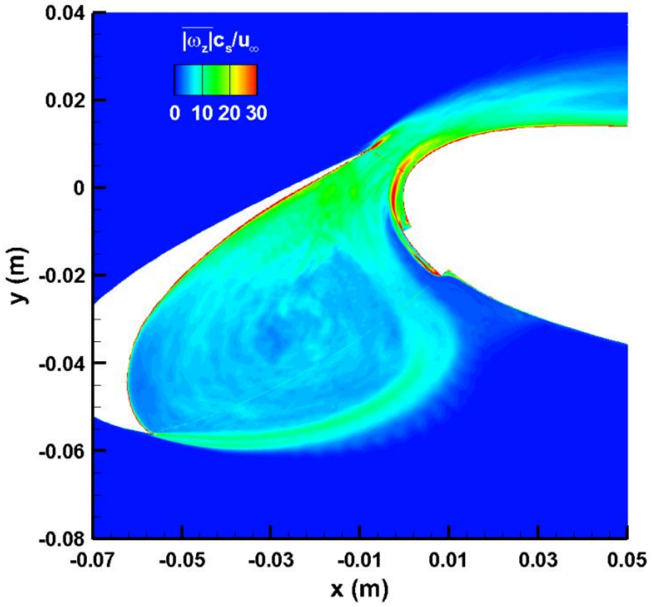

b) In the presence of strip.

Figure 4.9: Comparison of $\overline{|\omega_z|}$ values in the absence and presence of strip at AOA = 8 degrees, u_∞ = 25 m/s.

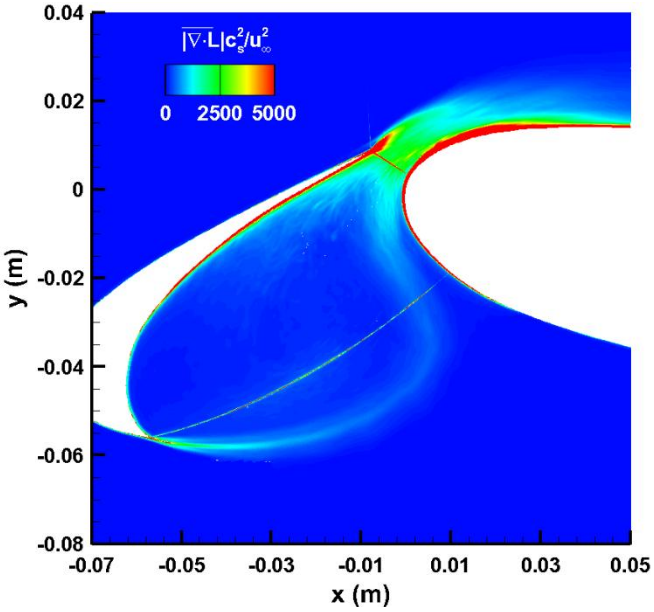

a) In the absence of the strip.

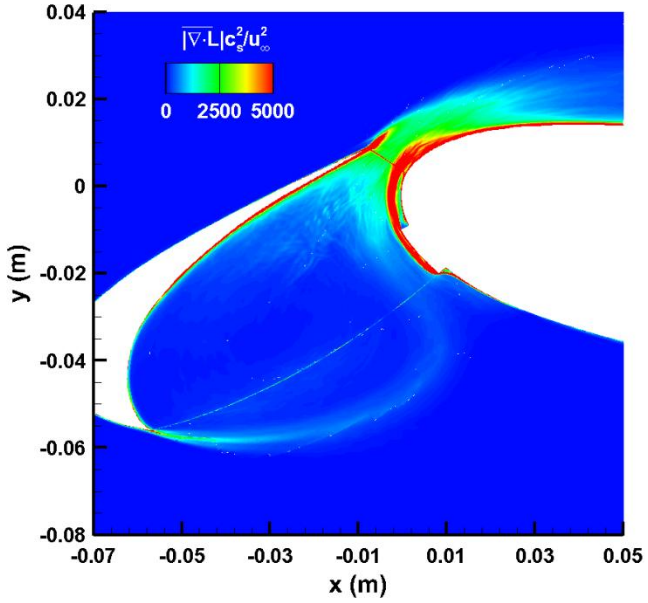

b) In presence of the strip.

Figure 4.10: Comparison of $\overline{|\nabla \cdot L|}$ values in the absence and presence of the strip at AOA = 8 degrees, u_∞ = 25 m/s.

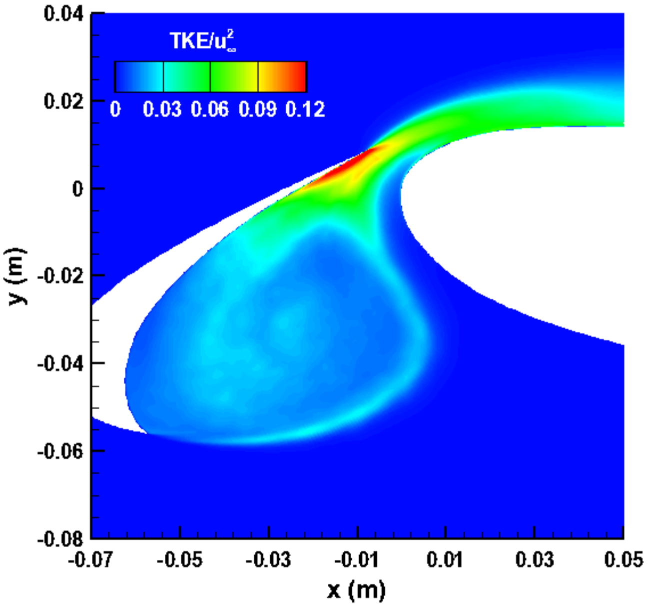

a) In the absence of the strip.

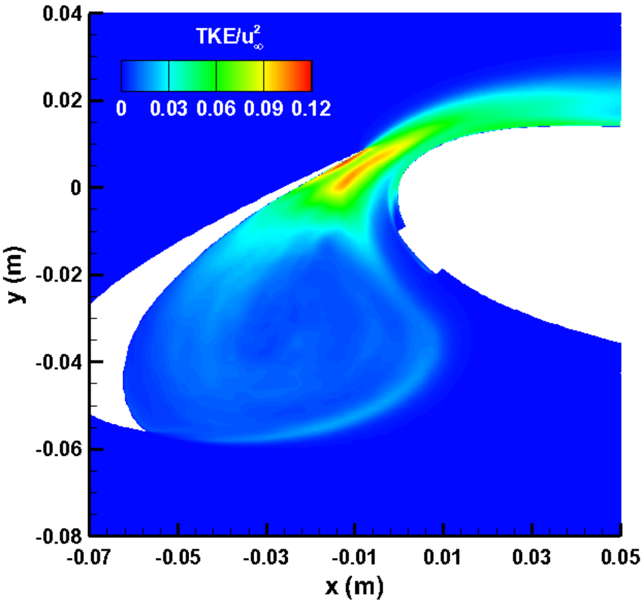

b) In the presence of the strip.

Figure 4.11: Comparison of mean TKE values in the absence and presence of the strip at AOA = 8 degrees, u_∞ = 25 m/s.

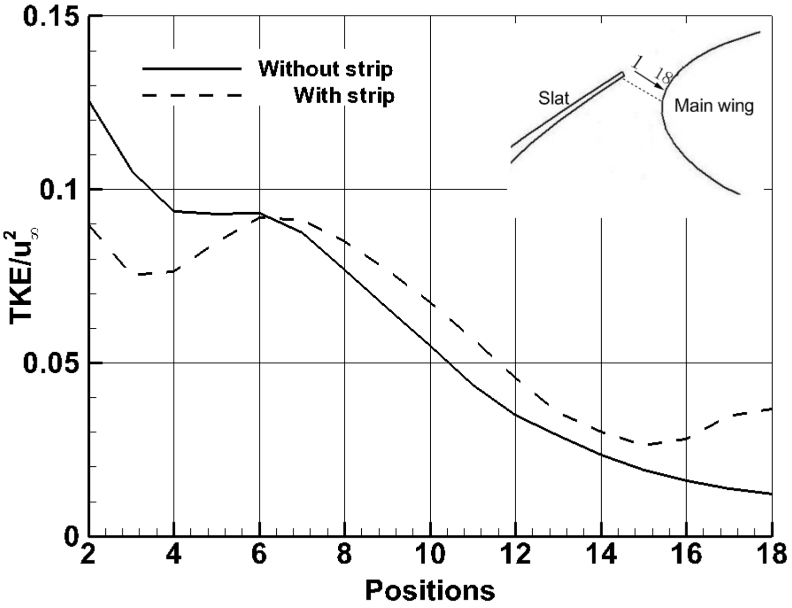

Figure 4.12: Comparison of mean TKE values along the gap line at AOA = 8 degrees, u_∞ = 25 m/s.

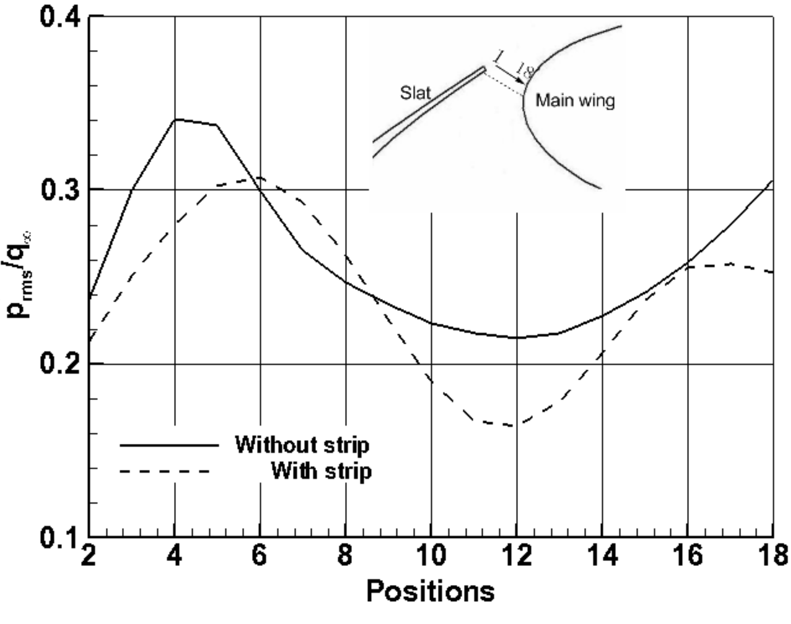

Figure 4.13: Comparison of p'_{rms} values along the gap line at AOA = 8 degrees, u_∞ = 25 m/s.

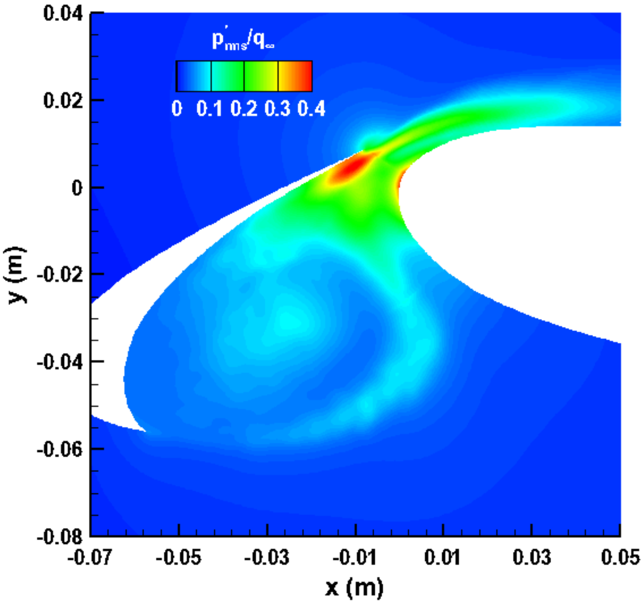

a) In the absence of the strip.

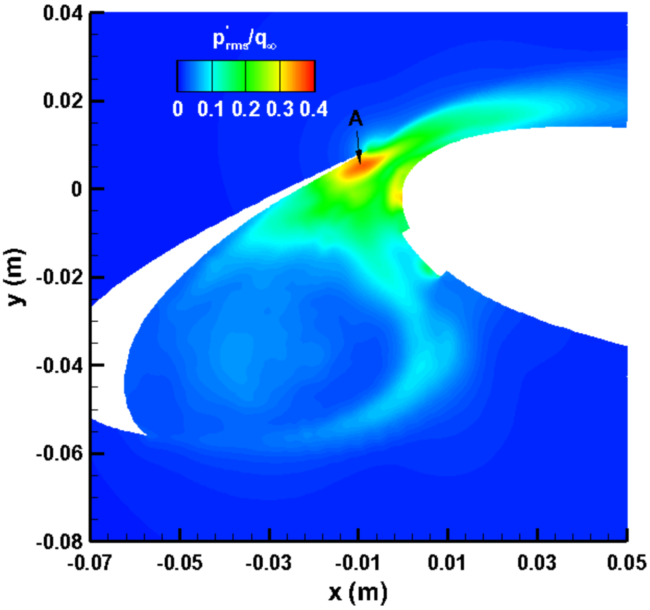

b) In the presence of the strip.

Figure 4.14: Comparison of p'_{rms} values in the absence and presence of the strip at AOA = 8 degrees, u_∞ = 25 m/s.

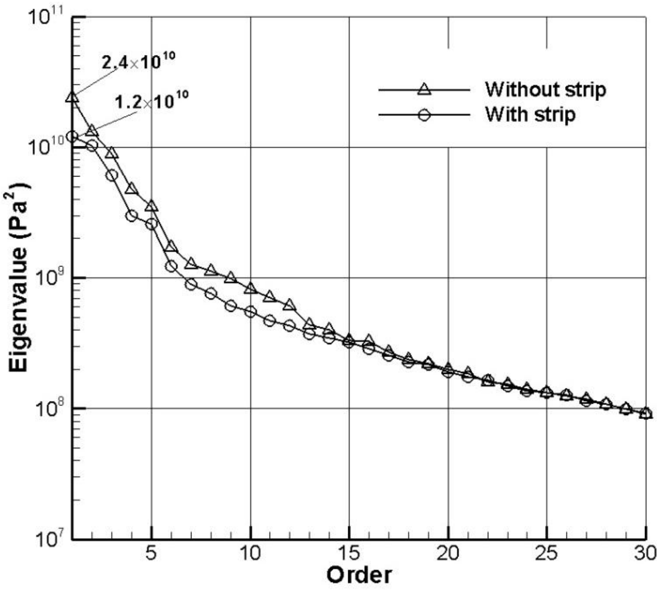

Figure 4.15: Comparison of eigenvalues of the first 30 modes in the absence and presence of the strip at AOA = 8 degrees, u_∞ = 25 m/s.

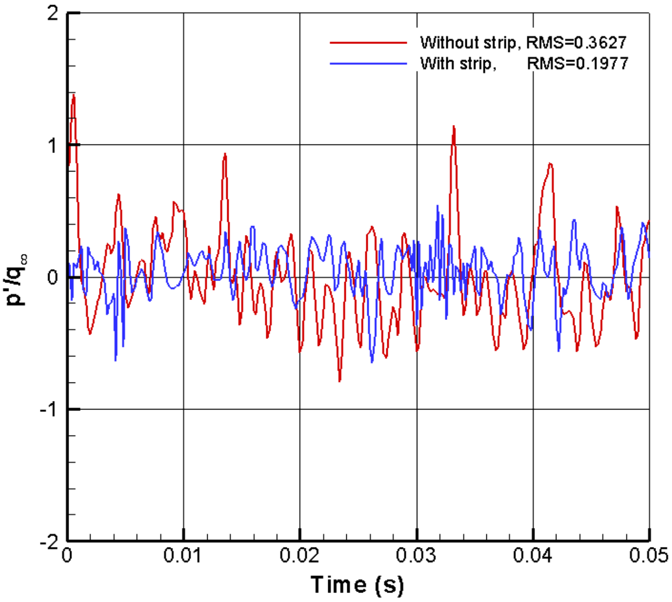

Figure 4.16: Comparison of pressure fluctuations of the first mode at point A (shown in Figure 4.13).

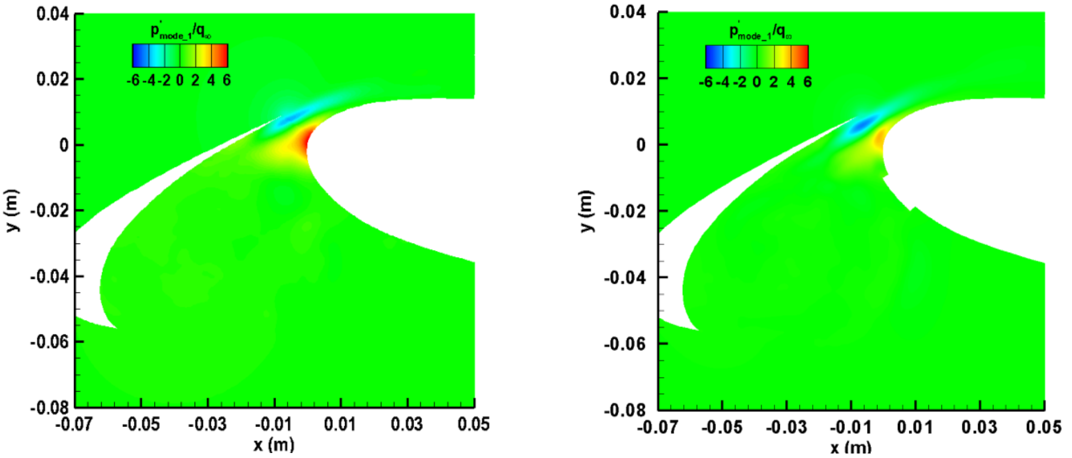

Mode 1 Mode 1

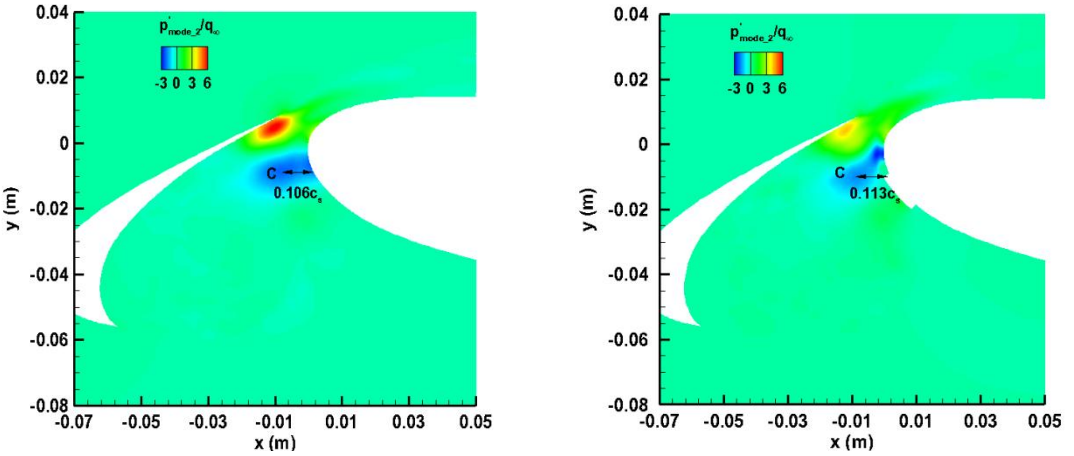

Mode 2 Mode 2

Figure 4.17: Comparison of the basis functions of pressure fluctuations in the absence and presence of the strip at AOA = 8 degrees, u_∞ = 25 m/s.

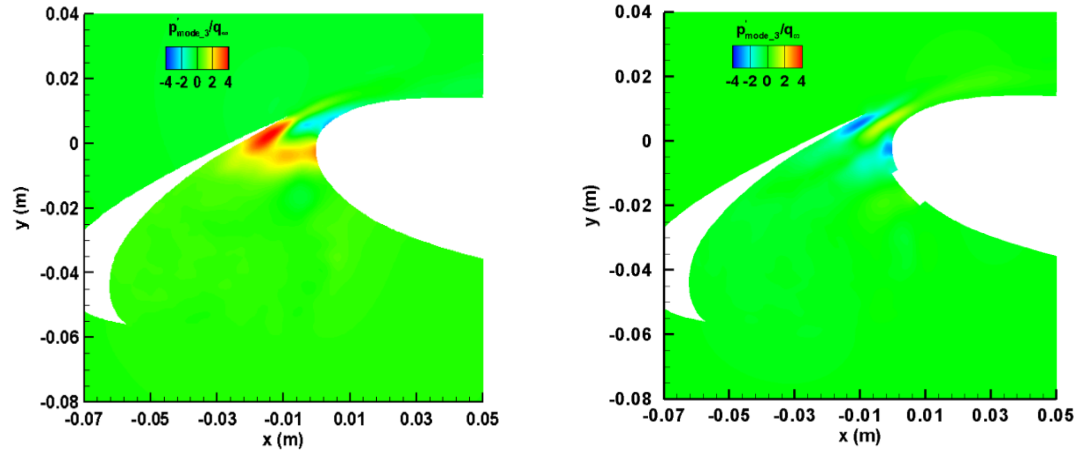

Mode 3 **Mode 3**

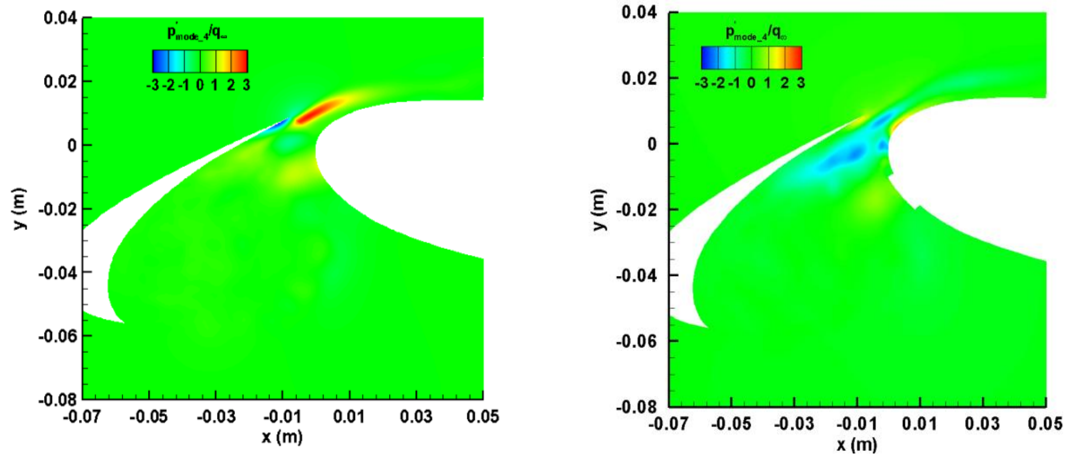

Mode 4 **Mode 4**

a) In the absence of strip. **b) In the presence of strip.**

Figure 4.17: Comparison of the basis functions of pressure fluctuations in the absence and presence of the strip at AOA = 8 degrees, u_∞ = 25 m/s.

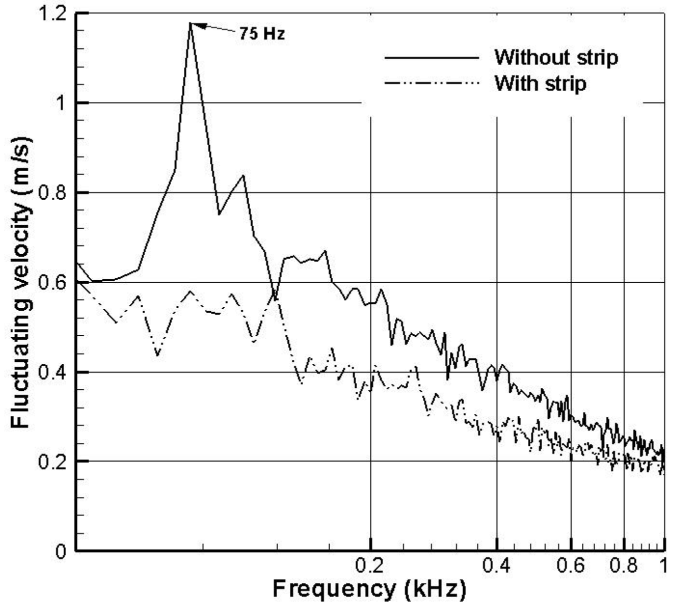

Figure 4.18: Comparison of fluctuating velocity spectrum at AOA = 8 degrees, u_∞ = 25 m/s, position 2 (shown in Figure 2.29).

Chapter 5

Active Control of Slat Noise Using Plasma Actuators

5.1 Introduction

Plasma actuator: Current developments in the design of aerodynamic vehicles demand increasingly more efficient techniques in terms of flow control. The sliding discharge design of the plasma actuator was first developed for laser-pumping application[79]. Zouzou *et al.*[80] and Louste *et al.*[81] then adapted it to atmospheric pressure. The single dielectric barrier discharge (SDBD) actuator has been widely explored over the past decade because of the advantages it offers. The main advantage of a plasma actuator is that it directly converts electric energy into kinetic energy without any moving parts. This renders the actuator structurally simple. Another advantage is that the response time is short and can be employed in a real-time control. However, the plasma actuator has its disadvantages, for example, low efficiency of energy conversion and low authority when regarded as an actuator [82-84]. Figure 5.1 schematically shows an SDBD actuator system, which mainly consists of two electrodes, one exposed and the other coated. The exposed electrode is directly exposed to the air and the coated electrode is encapsulated by a dielectric layer. The material of the dielectric layer can be Teflon, kapton, glass, ceramics or Plexiglas with thickness of 0.1 mm to a few mm[85]. If an alternating current (AC) driven by a sufficiently high voltage is supplied to the electrodes, the ambient air over the exposed electrode will become weakly ionized and cold plasma will be generated. Because of the asymmetric electric field generated by the electrodes, the ionized air results in a body force vector that then acts on the ambient air. This body force is the mechanism for active flow control[86-87]. Several variables have been found that affect the size of the body force. Orlov[88] suggested that the body force was proportional to the power dissipated by the actuator. Enloe *et al.*[89] gave the relationship of $P_{plasma} \propto V_{ac}^{3.5}$ for an actuator with a thin dielectric layer, where P_{plasma} is the consumed power and V_{ac} is the AC voltage applied on the actuator. Whereas Pons *et al.*[90] suggested

$$P_{plasma} \propto f(V_{ac} - V_0)^n, \qquad 2 < n < 3 \tag{5.1}$$

where V_0 is the threshold voltage and f is the AC frequency. The body force generated by the actuator is always proportional with the dissipated power. Besides the dissipated power, the body force also depends on several other factors including the dielectric material. For instance, Forte *et al.*[91] indicated that the body force increased with the thickness of the dielectric layer. Santhanakrishnan and Jacob[92] recommended that the dielectric layer should be several millimetres thick and have a low dielectric constant. With regards to the electrode configuration, Forte *et al.*[91] found that the overlap W_g (shown in Figure 5.1) only had a slight effect on the maximum body force as $0 < W_g/W_c < 2$, where equal to zero or a few mm[85]. W_c is the width of the coated electrode. However, Mereau[85] stated that the overlap had an obvious effect on the ionized-wind velocity. In Mereau's experiment, a 2 mm thick Plexiglas plate was used, and the electrodes had a width of 5 mm. The voltage applied on the electrodes was 20 kV and the driving frequency was 700 Hz. The results showed that the maximum ionized-wind velocity was achieved at an overlap of 5 mm. Mereau suggested that the electric field may fall down and the space charge could not anymore to move towards the downstream electrode as the overlap is bigger. In addition, the width of the coated electrode also has obvious effect on the ionized-wind velocity[85]. As the width is smaller than 20 mm, the velocity increases with the width, and then reaches a plateau. This results from that ions can be accelerated for a longer distance if the coated electrode is wider. However, the plasma self-sustaining cannot expand more than around 20 mm. The best configuration of a plasma actuator is that the overlap equal to 0 mm and the width of the coated electrode is 20 mm or overlap 5 mm and coated electrode 15 mm.

Orlov and Corke[93] indicated that the optimal AC frequency should be determined by the capacitance of the dielectric layer. Thomas *et al.*[94] investigated the relationship between the body force and the driving frequency, wherein the dielectric layer has thickness of 6.35 mm. The results showed that the lowest maximum body force was achieved at the driving frequency of 8 kHz, while highest at 1 kHz. The achievable maximum body force is decreased with the driving frequency increasing. At a fixed dissipated power, if the current is too large, the voltage will decrease and the body force will decrease.

When a plasma actuator is used in flow control, especially in dynamic flow control, the dynamic features (response time, bandwidth etc.) are important considerations. For a plasma actuator, during the positive half of the AC cycle (the voltage on the exposed electrode is higher than that on the coated electrode), electrons are released from the exposed electrode and move toward the dielectric layer. Within the negative half of the cycle, electrons are supplied by the discharged dielectric layer and move toward the exposed electrode. In addition, during the positive half cycle, the plasma contains a set of microdischarges, while more homogeneous during the negative half cycle. This demonstrates that the plasma is different during the two half cycle. The time scale of the process, at atmospheric pressure, occurs within a few tens of nanoseconds[86]. Orlov *et al.*[95] proposed a model which was concerned with the time-dependent body force produced by a plasma actuator

$$f_b^*(t) = -\left(\frac{\varepsilon_0}{\lambda_D^2}\right)\varphi(t)E(t) \tag{5.2}$$

where $f_b^*(t)$ is the body force, ε_0 is the permittivity of free space, $\varphi(t)$ and $E(t)$ are the electric potential and electric field respectively, and λ_D is called the Debye length, which is the characteristic length for electrostatic shielding in a plasma. By modeling the process of plasma generation, it was found that the dominating frequency of the body force was twice that of the plasma working frequency.

As previously mentioned, the application of the plasma actuator in flow control has been widely explored. Chuan *et al.*[96] showed that a SDBD actuator mounted on the leading edge of an airfoil effectively delayed flow separation and increased the lift-to-drag ratio. Similar results were also reported in other studies[97-98]. The application of the SDBD is not restricted to just aerodynamic purposes. For instance, the SDBD actuator has also proven effective in attenuating flow-induced noise[99-102]. Seraudie *et al.*[103] stated that boundary layer flow on a plate could be stabilized by a SDBD actuator and consequently transition was delayed.

Flow feedback control: Feedback control has been widely applied to industrial applications in recent decades due to its ability to provide improved stability and robustness yet remain simple to use. From the aerodynamic aspect, many studies have focused on the feedback control of cavity flow. This is because of its physical clarity and the resulting potential to use the applications in practice. Cattafesta *et al.*[104] proposed a detailed classification of cavity flow control within which feedback controls were further categorized into two schemes, quasi-static controls and dynamic controls. In some cases the features of an actuator, especially the bandwidth, determine which control scheme is preferable. Cattafesta and Williams[105] suggested that the ratio between the time scales of the actuator's and the plant's oscillations are an important parameter. In other words, if the time scale of the actuator's action is much longer than that of the plant oscillation, the plant should be controlled using a quasi-static approach[106]. If the time scales are comparable then dynamic feedback is suitable. However, if the time scale of the actuator is substantially shorter, the plant should be controlled by a high-frequency control. High-frequency control has been proven to be an effective approach in suppressing the broadband noise of a weapons bay[107] or the tonal noises of a cavity[108]. However the underlying mechanism of high-frequency control is still under debate. There are various approaches for constructing feedback modes to suppress the flow oscillations of a cavity, including heuristic control, adaptive control, model-based control etc.[105-106, 109-115].

Slat noise: As introduced in Chapter 1, it is generally agreed that slat noise is broadband in nature and, in some cases, superimposed by tonal components. Roger and Perennes[27] claimed that one of the slat tones shared the same mechanism as the cavity tones. Their experiment was conducted on a 1/11 2D scaled wing. One of the most prominent features in the experiment was the generation of narrow-band noise. The frequency of the narrow-band noise agreed well with the frequency predicted using the Rossiter formula[23-24, 34-35]. The other two tonal components are assumed to be generated near the slat cusp due to the coherent laminar flow separation. The high frequency tone is generated on the slat suction surface due to the Tollmien–Schlichting boundary layer instabilities.

This study aimed to attenuate slat noise using plasma actuators and consisted of several stages. Firstly, the mechanism of the tonal noise was experimentally and computationally investigated. Secondly, it was shown that slat noise could be significantly attenuated using a plasma actuator in an open loop setup. Finally a mathematic model, which described the slat plant, was identified using a system identification technique. Based on this model, a Linear-Quadratic-Gaussian (LQG) servo controller was constructed and tested.

5.2 Setup

5.2.1 Experimental model and wind tunnel tests

The model is the same as the one described in Chapter 2 and its sizes are shown in Figure 2.1. The experiment was conducted in the ISVR DARP anechoic chamber at the University of Southampton, which is described in Chapter 3. Figure 5.2 shows the slat model mounted in the chamber. In the experiment, the AOA of the main element was set to 4 degrees and the freestream velocity was set to 25 m/s, which corresponded to a *Re* number of approximately 5.7×10^5 (based on the main element chord). According to the results shown in Chapter 2, the intensive tonal noise merely appears at AOA = 4 degrees. Since the aim of the research is to suppress the tonal component using plasma actuator, it is natural to set the AOA to 4 degrees .to obtain a clear effect.

5.2.2 Instruments

Figure 5.3 illustrates the instruments that were employed in the experiment. The hardware mainly consisted of a high performance PC with a dSPACE system (Make: DS1104), a plasma power supply and two microphones. The high performance PC and dSPACE system performed in real time receiving feedback signals and calculating control inputs using the integration of Matlab/Simulink and dSPACE ControlDesk. The tasks of D/A (Digital-to-analogue converter) and Pulse Width Modulation (PWM) were performed by dSPACE. The strength of the plasma was regulated by DC voltage or the duty cycle of the PWM. In the experiment, the DC voltage was fixed at 30 Volts (V) and the driving frequency of the plasma generation was fixed at 12.5 kHz. Two microphones were employed to measure the noises in the near- and far-field respectively. The main features of the two microphones (Make: Bruel & Kjaer 4948 and Behringer ECM 8000) were described in Chapter 3. The A/D converter has the following features:

- 16-bit resolution;
- ±10 V input voltage range;
- ± 5mV offset error;
- ± 0.25% gain error;
- > 80 dB (at 10 kHz) signal-to-noise ratio (SNR).

Plasma actuator: Figure 5.4 schematically illustrates the primary electric circuit of the plasma actuator used in the research. The circuit mainly consists of a wave generator, electric switch, voltage transformer, direct current power, and electrodes. The wave generator is responsible for generating a waveform signal at a proper frequency, which equates to the plasma driving frequency. The electric switch serves as a DC-AC convertor and provides sufficient power to the voltage transformer. The voltage transformer increases a low voltage (several tens of volts) to a high voltage (10-30 kV). The transformer used in the experiment had a transforming ratio of 500. This supplied a high AC voltage of 15 kV to the plasma electrodes, as the DC voltage was fixed at 30 V. The plasma intensity, or the induced body force, can be regulated by the alteration of several parameters, e.g. the DC voltage, the driving frequency or the driving signal waveform. To expediently regulate the induced wind velocity using the dSPACE system, the plasma actuator was driven by a square waveform signal, in which the duty cycle was adjustable. The relationship between the induced velocity and the duty cycle was measured prior to the experiment. The thickness of the dielectric layer was 0.5 mm, the widths of the exposed and coated electrodes measured 5 mm and 10 mm respectively. The working frequency was set at 12.5 kHz. Figure 5.5a shows the relationship between the induced wind velocity and the duty cycle, wherein the induced velocity was measured at the location 4mm behind the trailing edge of the exposed electrode and 0.5 mm above the dielectric layer. It can be seen that the velocity increased linearly between a duty cycle of 0.23 to 0.43. Above this range the linear relationship was no longer present. Meanwhile, the dissipated power also presents a linear relationship with the duty cycle (shown in Figure 5.5b) as the value of duty cycle was lower than 0.4. The maximum induced velocity was 6.4 m/s at a duty cycle of 0.54. Figure 5.6 shows the velocity distribution around the exposed electrode, which was measured by PIV at rest medium. It can be seen that the upstream medium is deviated to the electrode, while the flow direction downstream is nearly parallel to the surface of the dielectric layer. The flow behind the plasma actuator behaves as jet with thin thickness. Since the jet flow is close to solid surface, it is expected that it can alter the velocity profile in flow boundary layer and infuse additional momentum into the boundary layer flow, and then change the flow features. Figure 5.7 shows an image as a plasma actuator working. Evenly blue light can be seen near the trailing edge of the exposed electrode. Some plasma filament also can be seen at some positions.

Two issues can result in a degraded signal-to-noise ratio. The first is the electromagnetic interference. Because the electrodes of the actuator are supplied with high frequency and high voltage current, intense electromagnetic waves are generated around the electrodes. This causes detrimental noise in the signal circuit. To solve the problem, all signal cables near the actuator were shielded using copper sheets. The second issue is ground interference. As shown in Figure 5.3, the plasma power supply was driven by the dSPACE system, so they share the same ground. It is well-known that a signal ground should be isolated from the grounding of a high power device. Otherwise the signal is unavoidably degraded by the interference. This issue can be addressed using an optocoupler. Figure 5.8 shows the electric circuit of the optocoupler used in the experiment; a high-linearity analogue optocoupler (Make: HCNR201) assumes the task of isolating the signal ground from the device ground. The HCNR201 consists of a high performance light-emitting diode (LED) which illuminates two closely matched photodiodes. The output photodiode produces a photocurrent that is linearly related to the light output of the LED. The LM339, which consists of four independent voltage comparators with an offset voltage specification as low as 2 mV, is responsible for shaping and amplifying the signal from the output of the HCNR201.

5.3 Features of Slat Tonal Noise

Figure 5.9 shows the SPL of the slat noise in the far-field at an AOA = 4 degrees, u_∞ = 25 m/s. The SPL decreases gradually within the frequency range of 0.28 kHz to 2.95 kHz, followed by a significant increase up to f = 4.4 kHz. Four obvious peaks, which correspond to four intense tonal noises, appear within the frequency range of 4.5 kHz to 6 kHz. However, at other AOAs larger than 4 degrees, tonal noises are not obvious. This is in accordance with the results[25]. Therefore, in the research the AOA was set to 4 degrees with the aim of suppressing the tonal components using the plasma actuator. As introduced in the preceding section, it is suggested that one kind of tonal noise shares the same mechanism as the cavity tones. However, the tones which present in this research are not governed by this mechanism. Firstly, the frequencies of the tones can be estimated in terms of the semi-empirical Rossiter formula[28]

$$f_n = \frac{u_\infty}{L_c}\frac{n-\gamma}{Ma + 1/_{\kappa}}, n = 1, 2, 3, \cdots \tag{5.3}$$

where *n* is an integer corresponding to the mode number; γ and κ are two empirical constants; u_∞ and *Ma* are the freestream velocity and *Ma* number respectively; and L_c is the length of the cavity. For a shallow cavity ($L_c/D > 4$, *D* is the depth of the cavity), κ = 0.57 and γ = 0.25, whereas κ = 0.57 for a deep cavity ($L_c/D < 2$). To estimate the tonal frequencies, only L_c and *D* are needed because the other parameters are already known. Figure 5.10 shows the distribution of the numerically simulated static pressure coefficient in the vicinity of the slat at AOA = 4 degrees, u_∞ =25 m/s. The details relating to the numerical simulation were presented in Chapter 2. Because at a low AOA a typical circulation region is not formed in the slat cove, the shear layer shedding off the slat cusp impinges on the main element. Therefore, as an approximation, the distance from the cusp to the stagnation line of the main element, rather than the trailing edge of the slat, is regarded as the length of the cavity, which measures 0.13 m and a depth, *D,* of 0.058 m. This yields a ratio of L_c/D of 2.24. Based on the above parameters, the estimated frequencies corresponding to the first four modes are: *f* = 82, 191, 301, 411 Hz, which are much lower than the measured tonal frequencies shown in Figure 5.9. Moreover, for cavity tonal noise the frequency interval between two successive modes remains constant and equal

$$f_{n+1} - f_n = \frac{u_\infty}{L_c} \frac{1}{Ma + {}^1\!/_\kappa}, n = 1, 2, 3, \cdots \tag{5.4}$$

Nonetheless, the frequency intervals of the peaks (shown in Figure 5.9) do not follow Equation (5.4). Therefore, it can be concluded that the tonal noises occurring in this experiment do not share the same mechanisms as the cavity tones.

To gain an insight into the mechanism of the slat tonal noise generation, a strip with a thickness of 0.5 mm was mounted at positions A, B, C, D (shown in Figure 5.11). The measurements showed that the tonal noise was suppressed only when the strip was positioned at location A. This means that the tones are closely related with the flow around the slat cusp rather than other parts of the slat. It is known that vortices can be shed off the slat cusp through the Kelvin-Helmholtz instability mechanism. To see whether the vortex shedding was directly responsible for the tones, a visualization experiment was conducted in the Plasma laboratory wind tunnel at the University of Southampton. In the experiment, a fast camera (Make: LaVision, Highspeedstar6) was employed to record the time-dependent images of the flow around the slat. The image sampling rate was 5000 frames per second and 500 images were captured over a period of 0.1 s. The AOA of the model and the freestream velocity equaled 4 degrees and 15 m/s respectively. One instantaneous image is shown in Figure 5.12. Vortices are clearly visible in the wake of the slat cusp, and the distance between two successive vortices (Δs) measures 5.5 mm approximately. The vortex shedding frequency f can be estimated in an approach outlined by Kaepernick *et al.*[116], that is

$$f = \frac{u_s}{\Delta s} \tag{5.5}$$

where u_s is the local flow velocity. According to Equation (5.5), the vortex shedding frequency from the slat cusp is

$$f \approx \frac{u_\infty}{\Delta s} = \frac{15}{0.0055} = 2.7\ k\mathrm{Hz} \tag{5.6}$$

The corresponding *St* number equals approximately 16 (based on the slat chord). This estimation is made at a freestream velocity of 15 m/s. For a flow with a freestream velocity of 25 m/s, the vortex shedding frequency can be estimated to be 4.5 kHz provided that the *St* number remains unchanged. This estimation is close to the frequency at which peak 1 appears (shown in Figure 5.9). Therefore, it is reasonable to assume that the slat tones have arisen from the shedding vortices. However, the strength of the tones is significantly high when compared with that of the broadband noise. This implies that a close-loop mechanism or a kind of standing wave exists to enhance the noise radiation. The wavelength of sound corresponding to a frequency of 5.6 kHz (peak 4 in Figure 5.9) is approximately 0.061 m, which is nearly half the distance between the slat cusp and the stagnation line (shown in Figure 5.10). This suggests that the tone corresponding to peak 4 is a kind of standing wave with two ends of the slat cusp and the stagnation line.

5.4 Open-loop Control Using a Plasma Actuator

As discussed above, the tonal noise is closely related with the vortices shedding off the slat cusp and can be attenuated by a strip mounted at position A (shown in Figure 5.11). Based on this knowledge, a plasma actuator was flush mounted on position A, the aim of which was to suppress the tone. Figure 5.13 demonstrates the noise reduction in the far-field at AOA = 4 degrees, u_∞ = 25 m/s. According to the measurements, the self-noise of the actuator appears nearly flat within the frequency range of 0.2 to 5 kHz and this is followed by a sharp peak at f = 5.8 kHz. The peak is regarded as the consequence of the first subharmonic of the plasma actuator, because the frequency of the peak is nearly half that of the driving frequency of the actuator. Above the frequency f = 5.8 kHz and until f = 9 kHz, the self-noise tends to increase with the frequency rise. Regarding the slat tonal peaks it can be seen that the first four peaks were significantly reduced. This was especially the case for the fourth peak in which a reduction of 24 dB was achieved. However, the actuator led to an obvious increase at the fifth peak. Lastly, it is observed that the noise within the frequency range of 1.5 to 4.5 kHz obviously increased, whereas the noise within the frequency of 0.825 to 1.5 kHz was attenuated. Taking a comparison of the effects between the duty cycle of 0.3 and 0.45, the latter shows a better effect, the noise within the frequency range of 0.825 to 9.5 kHz is less than that corresponding to the duty cycle of 0.3. Figure 5.14 shows the comparison of the RMS of acoustic pressure in the far-field at various duty cycles. The RMS experiences a rapid decrease as the duty cycle alters from 0 to 0.3. Nevertheless, a slow decrease appearing like an asymptote happens within the duty cycle range of 0.3 to 0.45.

5.5 Feedback Control of Slat Noise

As discussed in Section 5.4, open-loop control using a plasma actuator can reduce the slat noise, and a larger value of the duty cycle achieves a higher reduction of the slat noise. However, in some cases there is a need for a trade-off between the noise reduction and the power consumption. In addition, the system needs to be able to remain stable under various external disturbances. Under these circumstances, a feedback control system is more competent than an open loop control. As stated before, there are different types of feedback controllers in terms of the ratio of time scales between an actuator action and a plant oscillation, e.g. quasi-static, dynamic and high-frequency controls. However, there are a few limitations which prevent the plasma actuator from being a good dynamic feedback controller:

a) Unlike other kinds of actuators, the plasma actuator must be driven by a working frequency, which consequently defines the frequency of the dominant body force. In this study, the working frequency was 12.5 kHz, so the frequency of the dominant body force was 25 kHz[95], whilst the frequencies of the tonal peaks of the slat appeared below approximately 6 kHz. The time scale of the body force is substantially shorter than that of the slat tonal noises. Therefore a control under the authority of the plasma actuator can be classified as a high-frequency control. The high-frequency control has been proven effective in reducing both tonal and broadband noise[107-108]. However, there are still a number of uncertainties around high-frequency control, especially in engineering practice. Wiltse and Glezer[117] proposed that the high-frequency control resulted in enhanced energy transfer from the large to the small scales, and in a substantial increase in both the consumption and decay rate of the turbulent kinetic energy. Therefore, if the plasma actuator was regulated by a sinusoidal duty cycle with the time scale of the slat tones, the resulting driving signals to the plasma actuator would be the superimposition of the sinusoidal duty cycle and the driving signal (12.5 kHz square wave). The resulting body force generated by the actuator would be the superimposition of the two forces corresponding to the two signals. Hence, if the actuator is used in a control system it is difficult to discern which kind of control, the high-frequency control or the dynamic control, is dominant.

b) The efficiency of the plasma actuator (i.e. the ratio between the body force and the consumed power) mainly depends on the driving frequency. Even though the working frequency can be adjusted to be a comparable level as the slat tonal noise, the efficiency of the actuator may significantly decrease. One of the most important benefits presented by dynamic control is less power consumption. However, the decreased efficiency of the actuator can negate this benefit.

c) An actuator's self-noises are generated at the driving frequency and the harmonic and subharmonic frequency. If the driving frequency is comparable to the frequency of the slat tonal noise, discernment between the slat noise and the self-noise becomes difficult. Therefore, in this study, the driving frequency was increased as high as possible to avoid the frequency range of the measured slat noise.

d) The construction of a suitable mathematical model for the control of the slat noise is difficult. Firstly, because of insufficient knowledge about the process of slat tones generation, a physical-based mathematical model is unavailable at present. Secondly, it is imperfect to determine an empirical model using system identification techniques based on experimental input/output data. For instance, Cabell *et al.*[118] used a frequency-weighted Linear Quadratic Gaussian (LQG) model with one input and two outputs to describe a cavity flow, wherein the input corresponded to a synthetic-jet actuator and the outputs corresponded to two pressure sensors in the cavity. It was found that a model with very high order (150–200 states) was compulsory to describe the cavity flow, and the coherence between the input and output was low. This is suggested to arise from the existence of two loops, internal and external loops inside the feedback control. The internal loop is the well-known acoustic feedback loop, wherein the acoustic fluctuations originating at the trailing edge induce vortices to shed off the leading edge of the cavity. This loop dominates the cavity tones generation when under no external disturbance. The external loop is the dynamic control of the cavity flow using the synthetic-jet actuator. However, even in the presence of the external loop, the internal loop significantly affects the cavity flow. In this study, if the slat tonal noise is dynamically controlled using the plasma actuator, a model constructed using the system identification techniques will unavoidably have a similar issue with the cavity, which is the high order and low coherence between the input and output. To avoid the pitfalls mentioned above, in this study a quasi-static control was exploited to attenuate the slat noise. This control was also employed by Shaw and Northcraft[119] and Samimy *et al*[120] to suppress the cavity flow oscillation. However, it should be noted that, accompanied by the quasi-static control, the high-frequency control still takes part in the process due to the features of the plasma actuator

5.5.1 Choice of Time Scale

A simple mathematical model can be constructed according to the measurements (shown in Figure 5.14).

$$p_{rms} = k_p u_d + p_{rms\_o} \tag{5.7}$$

where p_{rms} denotes the RMS of the acoustic pressure, u_d is the value of the duty cycle, k_p is a constant and equal to approximately -0.06, and p_{rms_o} denotes the p_{rms} value as u_d = 0 and equals 0.72 in this study. The linear function approximately describes the relationship between the output (RMS of the acoustic pressure) and the input (duty cycle) as the values of the duty cycle are less than 0.3. If the p_{rms} value needs to be regulated to a given value, p_{rms_1}, which is within the range of 0.53 to 0.72, the corresponding value of the duty cycle can be set according to

$$u_{d\_1} = (p_{rms\_1} - p_{rms\_o)}/k_p \tag{5.8}$$

without disturbance, the p_{rms} value is retained at the given value. However, the p_{rms} value will deviate from the given value under disturbances. If the deviation of the p_{rms} value is measured as Δp_{rms}, the u_d value should be set to $u_{d\_1} + \Delta p_{rms}/k_p$ to get the p_{rms} value back to the given value. However, if the p_{rms} value is taken as the feedback signal, an issue associated with the time step arises. As shown in Figure 5.15, the p_{rms} values shown in Figure 5.14 are calculated over a rather long time segment of 16 s. A time step as long as 16 s is unacceptable for the feedback control of slat noise, a shorter time step is more practical. Nonetheless, it is well-known for any random signal that the calculation of an unambiguous RMS value demands sufficient sampling time. Figure 5.15 demonstrates how an RMS value depends on the sampling time, wherein the acoustic pressure was measured in the near-field at an AOA = 4 degrees and u_∞ = 25 m/s. It can be observed that the RMS converges only when the sampling time is sufficiently long, for example 5 s. A shorter sampling time would lead to uncertainty in the RMS values and uncertain feedback signals can lead to inappropriate command calculation, hence the feedback system works improperly. However, it is also important that the time step is sufficiently short to improve the performance of the system, for example, to enable a fast response to a given value or disturbance. The issue originating from uncertain feedback signals can be partially solved by using a proper algorithm, e.g. the Kalman filter. In this study, a time step of 0.2 s was employed, because this time step offered a compromise between the necessary quick time response of the system and the uncertainty of feedback signals. The disadvantageous consequences arising from the uncertainty of feedback signals can be improved by the following algorithm.

5.5.2 System Identification

A system identification algorithm, auto-regressive/exogenous-input (ARX), was employed to obtain the mathematical model of the slat noise generation. The algorithm is an input-output polynomial model with the structure:

$$A(q^{-1})y(t) = B(q^{-1})u_d(t - n_k) + \epsilon(t) \tag{5.9}$$

where $y(t)$ and $u_d(t)$ are the output and input at time *t* respectively, n_k denotes the input delay and $\epsilon(t)$ represents white noise disturbances. A and B are polynomials in the backwards shift operator q^{-1}

$$\begin{aligned} A(q^{-1}) &= 1 + a_1 q^{-1} + a_2 q^{-2} + \cdots + a_{na} q^{-na} \\ B(q^{-1}) &= b_1 q^{-1} + b_2 q^{-2} + \cdots + b_{nb} q^{-nb} \end{aligned} \tag{5.10}$$

where *na* is the number of poles and *nb* is the number of zeros plus 1. The model's parameters, A and B, can be estimated by minimizing the error between the model outputs and the measured outputs. Figure 5.16 shows the integrated plant which will be identified by the ARX algorithm. The integrated plant consists of the plasma actuator, the slat and the microphone. The input for the plant was the duty cycle and the output was the RMS of the acoustic pressure. w_i and w_b are the process and measurement noises respectively. To acquire the proper input/output data for the identification of the plant, the plasma actuator was driven by a random duty cycle (input) at a uniform time step of 0.2 s. The acoustic pressures in the near-field were measured simultaneously at a sampling rate of 20 kHz, which provided an ensemble consisting of 4096 samples for every time step of 0.2 s. The RMS of the acoustic pressure (output) was calculated over every time step. Finally, a set of data, which comprised of 600 input/output pairs, was used to identify the plant. By testing a variety of parameters inside the ARX algorithm, a model with *na* = 4, *nb* = 2 and n_k = 0 was found to optimally describe the plant. The numbers of *na* and *nb* not equalling unity indicated that the plant had dynamic features, because the past outputs and inputs affected the current outputs. The parameters *A* and *B* were

$$\begin{aligned} A(q^{-1}) &= 1 - 0.1295q^{-1} - 0.09174q^{-2} + 0.1074q^{-3} - 0.009056q^{-4} \\ B(q^{-1}) &= -14.91 + 2.908q^{-1} \end{aligned} \tag{5.11}$$

Figure 5.17 shows the comparison between the simulated and measured outputs. It can be observed that the magnitudes of the simulated outputs are much lower than those of the measured outputs although both have the same phases for most of the time.

For a real-time control system, a low-order model has many advantages over a high-order one, for example, a low-order model is often easier to analyze and much faster to simulate. The basic idea of order reduction is to replace the high-order model with a low-order one provided that the key features are retained. To verify whether the order of the identified model can be reduced or not, the Hankel singular values of the model were calculated and are shown in Figure 5.18. The Hankel singular values measure the contribution of each state to the input/output behaviour. Minor values mean that the corresponding states had less contribution, hence they can be discarded. As shown in Figure 5.18, the last Hankel singular value is very small when compared with the other three. Hence the fourth-order model can be reduced to a third-order one by discarding the fourth state. Figure 5.19 shows the comparison of the Bode diagram between the fourth-order and the reduced models. The deviation between the two models is minor.

5.5.3 Controller Design

A Linear Quadratic Gaussian (LQG) servo controller was incorporated into the plant to implement the feedback control. The LQG servo is one of the most basic optimal techniques for dynamic controller design. It balances control efforts with tracking performance and is able to deal with process and measurement noises. In most cases, a LQG controller consists of a linear quadratic integral (LQI) optimal gain and a linear quadratic estimator (LQE) state estimator.

LQI optimal gain: Firstly, given the model of the plant in state-space:

$$\begin{aligned} &x[k+1] = Ax[k] + Bu_d[k], \qquad x[k_0] = x_0 \\ &y[k] = Cx[k] \end{aligned} \tag{5.12}$$

As shown in Figure 5.20, the LQI is able to calculate an optimal gain matrix K to minimize the following cost function with the control law $u = -Kz = -K[x; x_i]$

$$J_u(x[k_0], k_0) = \sum_{k_0}^{k_f} (z[k]^T \Psi z[k] + u_d[k]^T \Phi u[k]) + z[k_f]^T \Psi z[k_f] \tag{5.13}$$

where x_i is the integration of the state error, Ψ and Φ are weighting matrices which balance the control efforts (power consumed by the actuator) and the control performance (the time over which the plant was driven from the initial state to the reference state), and k_o and k_f correspond to the start and end of the regulating time. If the horizon tends to infinity ($k_f \rightarrow \infty$), the last term in Equation (5.12) becomes negligible. The solution to Equation (5.12) can be written as

$$u_d^0[k] = -Kz[k], \;\; K = (\Phi + B^T PB)^{-1} B^T PA \tag{5.14}$$

where $u_d^0[k]$ is the control input at the k^{th} time step. K and P satisfy the discrete time algebraic Riccati equation

$$A^T\big(P - PB(\Phi + B^T PB)\big)A + \Psi - P = 0 \tag{5.15}$$

Nonetheless, it can be seen that the connection of the weighting matrices Ψ and Φ with the closed-loop dynamics is indirect. Hence, in practice, some trial-and-error procedures have to be performed to obtain satisfactory closed-loop dynamics[121]. As Φ and Ψ are both unit matrices, the optimal gain K is calculated:

$$K = [-0.0954 \quad -0.0845 \quad 0.0413 \quad 0.2238] \tag{5.16}$$

Kalman state estimator: In control theory, the LQE commonly refers to the Kalman state estimator. The Kalman estimator uses the model of the plant, the known control inputs and measurements to form an estimate of the plant's states. The Kalman estimator has two important benefits. Firstly, it can use noisy measurements to estimate values which tend to be closer to the true values of the measurements. Secondly, in most cases there are more internal states than states which can be measured. The Kalman estimator can estimate the entire internal state by combining a series of measurements. For example, in this study there are three state values needed in the LQI to calculate an optimal gain K. However, only one state value is measured at each time step. The entire three states can be obtained using the Kalman state estimator. A model with process and measurement noise can be described as[122]

$$\begin{aligned} x[k+1] &= Ax[k] + Bu_d[k] + Gw_i[k] \\ y[k] &= Cx[k] + Du_d[k] + Hw_i[k] + w_b[k] \end{aligned} \tag{5.17}$$

where $w_i[k]$ and $w_b[k]$ are the process and measurement noise respectively, and $w_i[k]\sim(0,Q)$ (mean $\overline{w[k]}=0$, covariance $\overline{w[k]w[k]^T}=Q$), $v[k]\sim(0,R)$. The Kalman estimator estimates a state value $\hat{x}$ which minimizes the error covariance:

$$\lim_{K\to\infty} E\left((x[k]-\hat{x})(x[k]-\hat{x})^T\right) \tag{5.18}$$

The optimal solution is

$$\begin{gathered}\frac{d}{dt}\hat{x} = A\hat{x} + Bu + L(y - c\hat{x} - Du_d)\\ \begin{bmatrix}\hat{y}\\ \hat{x}\end{bmatrix} = \begin{bmatrix}C\\ I\end{bmatrix}\hat{x} + \begin{bmatrix}D\\ 0\end{bmatrix}u_d\end{gathered} \tag{5.19}$$

with

$$\begin{aligned}&L = (PC^T + \bar{N})\bar{R}^{-1}\\ &\bar{R} = R + HN + N^TH^T + HQH^T\\ &\bar{N} = G(QH^T + N)\\ &\frac{dP}{dt} = AP + PA^T - PC^TQ^{-1}CP + R\end{aligned} \tag{5.20}$$

For the slat noise control (shown in Figure 5.16), the process noises are fluctuations in the duty cycle and other unknown disturbances. As shown in Figure 5.21, the fluctuations of the duty cycle were sufficiently low to be ignored. The other disturbances could not be measured, so an estimation of 0.02 was imposed for the process noise covariance. The measurement noises consist of several aspects, for example, the background noise of the wind tunnel, the self-noise of the plasma actuator etc. The levels of both the background noise and the self-noise in the near-field are much lower than that of the slat noise within the bandpass frequency of the filter, hence they can be neglected. However, the RMS of the acoustic pressure over a short time step deviated significantly from the corresponding convergent value (shown in Figure 5.15). In this study, these deviations are grouped into the measurement noise. According to the measurements, the covariance of the measurement noise was approximately 0.8.

LQG servo controller: Finally, the Kalman estimator was connected to the LQI optimal gain to form the one-degree-of-freedom LQG servo controller (shown in Figure 5.22). The inputs of the controller are the differences between the reference and the feedback. The outputs are the commands to the plasma actuator: $u=-K[\hat{x};x_i]$. This controller ensures the output tracks the reference command and rejects process disturbances, $w_{i,}$ and measurement noise, w_b. The parameters of the controller in state-space are

$$\begin{aligned}
A &= \begin{bmatrix} -0.45 & 0.51 & 0.2 & -0.25 \\ -0.44 & 0.57 & -0.45 & 0.03 \\ -0.04 & 0.05 & 0.07 & 0.31 \\ 0 & 0 & 0 & 1 \end{bmatrix} \\
B &= [\,0.00034 \;\; -0.0049 \;\; -0.005 \;\; 0.2] \\
C &= [\,0.09537 \;\; 0.08446 \;\; -0.04134 \;\; -0.2241] \\
D &= [\,-0.00008086]
\end{aligned} \tag{5.21}$$

5.5.4 Implementation of Feedback Control

The controller was implemented using Matlab/Simulink together with the real time block tools provided by dSPACE. The diagram of the controller is shown in Figure 5.23, wherein the signal collecting block was responsible for acquiring the slat noise at a sampling rate of 20 kHz, and the role of the RMS block was to calculate the RMS values over every time step. The difference between the RMS value and the reference was taken as the input to the LQG servo controller. The controller then calculated out the corresponding control input. The block “MeandutyAdd” was used to compensate the offset that was obtained in the model identification described previously. The saturation block, with an upper limit of 0.45 and a lower limit of 0.23, forces the commands to collapse into the appropriate range. Finally, the control input was fed into the PWM port of the dSPACE system.

To verify the effects of the controller, an experiment was conducted at AOA = 4 degrees, u_∞ = 25 m/s. The reference was set to 4.5 Pa. Figure 5.24 shows the time history of the RMS of pressure, which was measured using the near-field microphone and calculated over a time step of 0.2 s, and the duty cycle (input to the plant) as the feedback control is activated. Although at some time steps, the RMS of pressure deviates obviously away from the reference, it is suspected that the deviation mainly results from the computation of RMS over a short time period. In addition, the mean of the RMS is approximate 4.43 Pa, which is close to the reference of 4.5 Pa. In a general view, the RMS of pressure traces the reference well. Figure 5.25 shows the comparison of the output voltages in the far-field between ‘controller on’ and ‘controller off’. It is obvious that the acoustic pressures were attenuated significantly when the controller was turned on.

5.6 Summary

Several tonal noises appear in the slat noise spectrum at AOA = 4 degrees, u_∞ = 25 m/s. It was found that the dominant tone was associated with the vortex shedding off the slat cusp through the Kelvin-Helmholtz instability rather than, as previously suggested, a mechanism similar to that seen in a cavity flow. The strength of the plasma can be regulated by the duty cycle of the PWM. The ionized-wind velocity presents a linearly relationship with the duty cycle as its value falls within the range of from 0.23 to 0.45. When plasma actuator is working, three kind of interferences impose negative effect on the measurements of noise signal.

The dominant tone was successfully suppressed by the use of a plasma actuator run in an open-loop control. The maximum reduction of 11 dB was achieved at a frequency of approximately 5.6 kHz. From a control perspective, the slat noise reduction by the plasma actuator should be classified as high-frequency control, because the time scale of the body force generated by the actuator was substantially shorter than the time scale of the slat dominant tone. A quasi-static feedback control system was developed, in which an LQG servo controller was responsible for calculating the control input in terms of the feedback signals. The experimental results show that the controller does work to effectively suppress the slat noise.

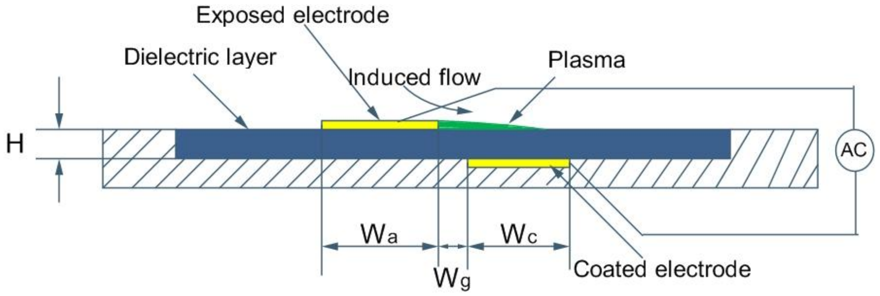

Figure 5.1: Schematic diagram of an SDBD actuator.

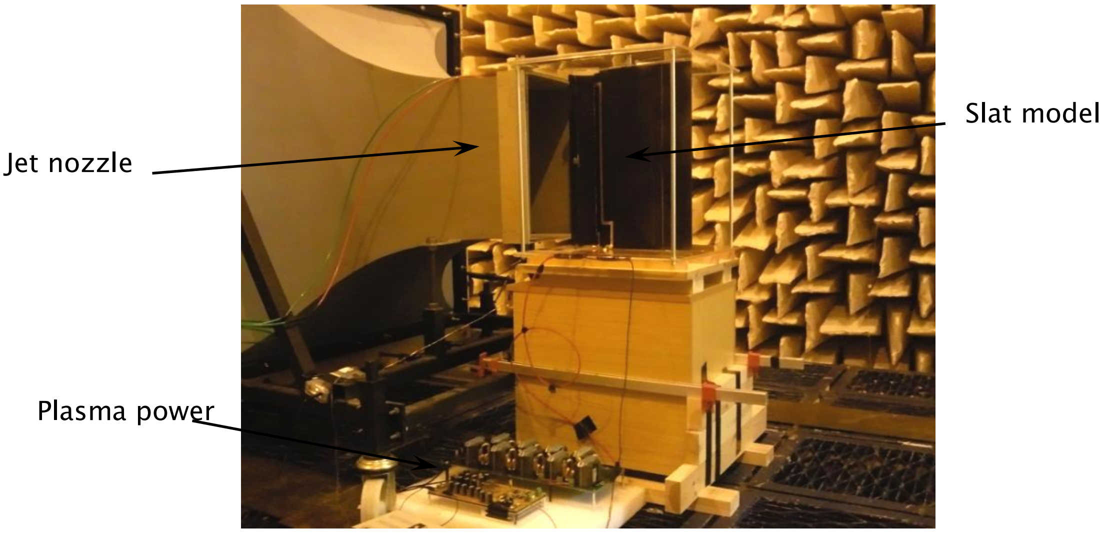

Figure 5.2: Slat experimental model installed in the ISVR DARP anechoic chamber.

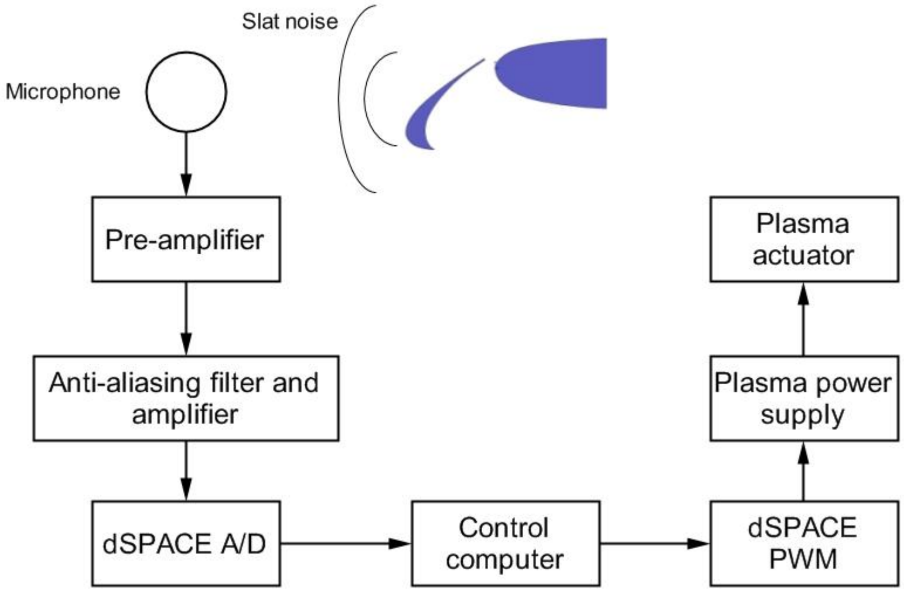

Figure 5.3: Main instruments used in the research.

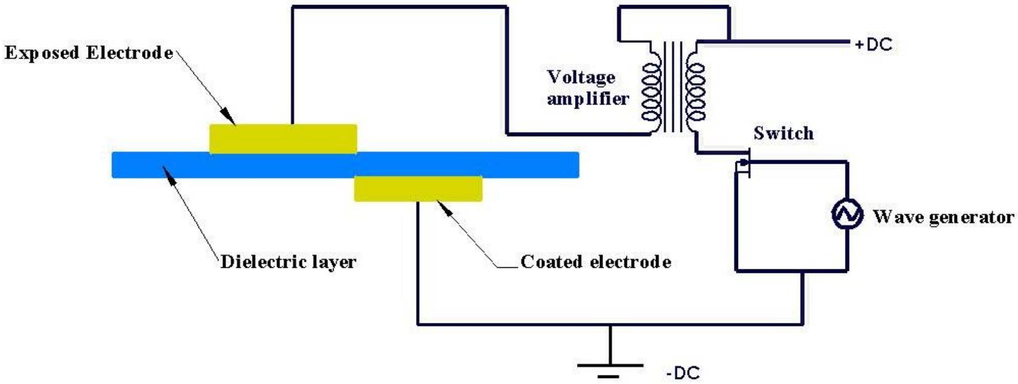

Figure 5.4: Schematic diagram of an electric circuit for a plasma power supply.

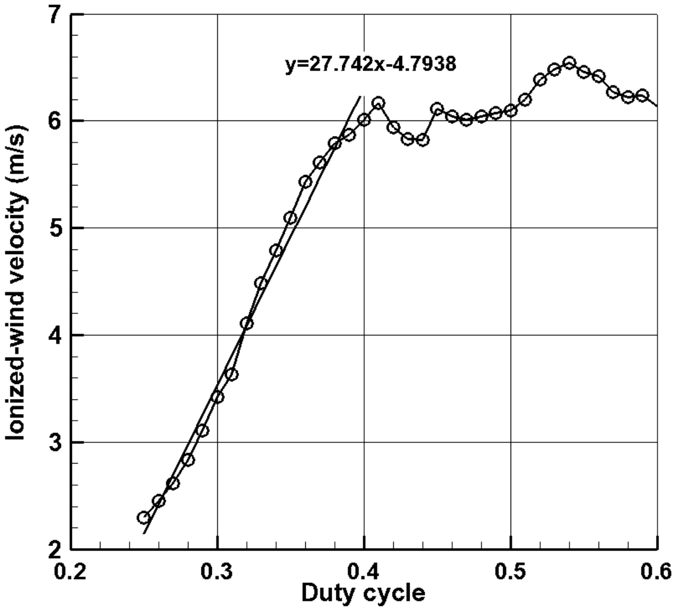

a) Relationship between the duty cycle and the induced wind velocity

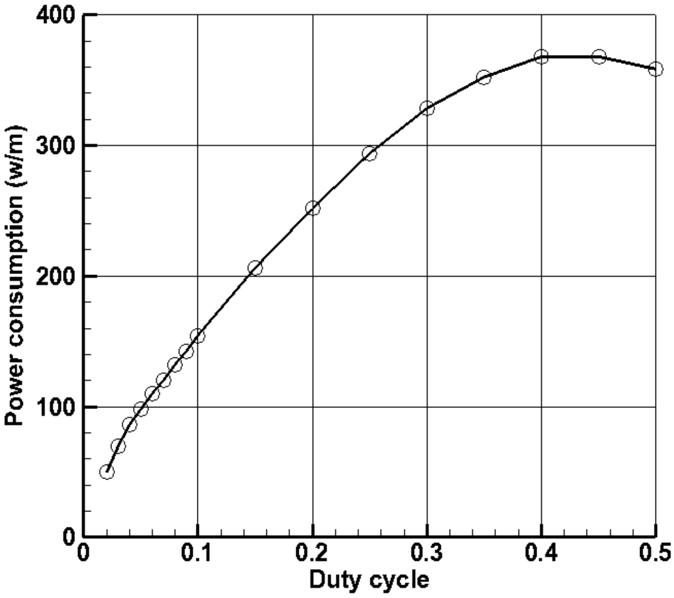

b) Relationship between the duty cycle and the dissipated power.

Figure 5.5: Relationship between the duty cycle and the induced wind velocity and dissipated power, in which the DC voltage is fixed at 30 V and the driving frequency at 12.5 kHz.

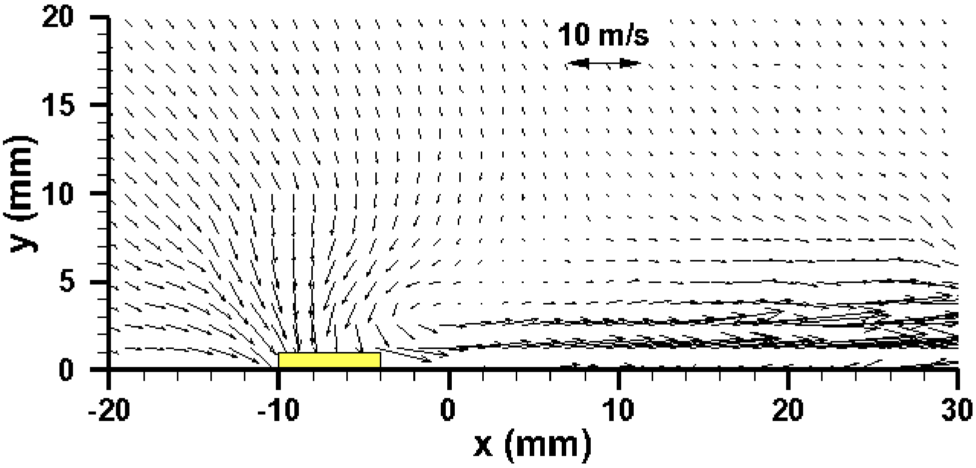

Figure 5.6: Velocity field around the exposed electrode measured by PIV.

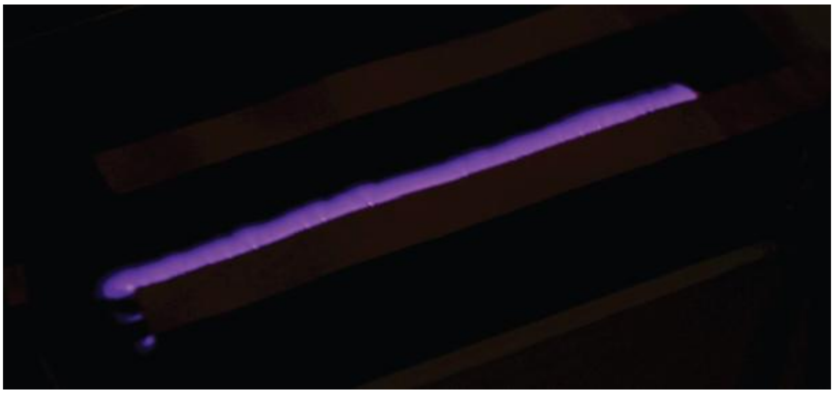

Figure 5.7: Image as plasma actuator working, evenly plasma is generated at the edge of the exposed electrode, some plasma filaments also can be seen.

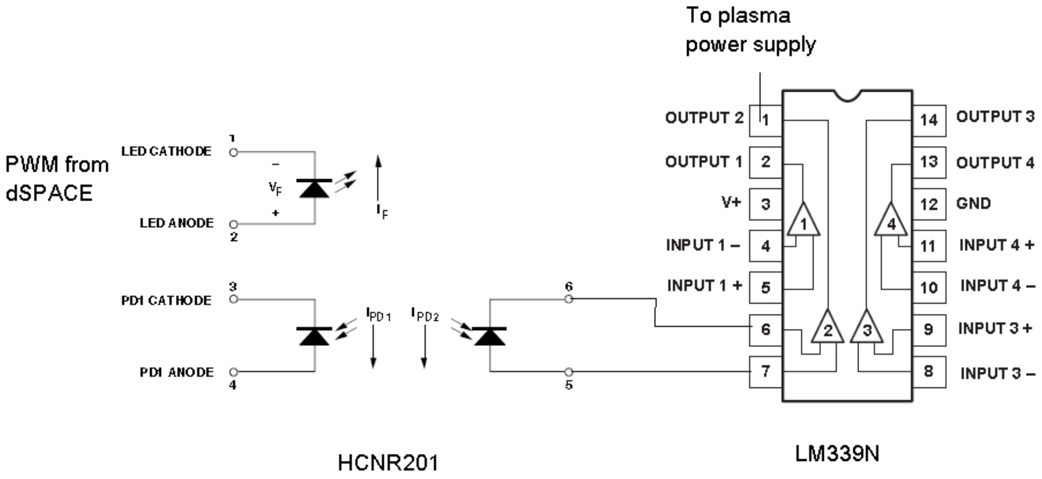

Figure 5.8: Optocoupler used to separate the ground cables of dSPACE with plasma power supply.

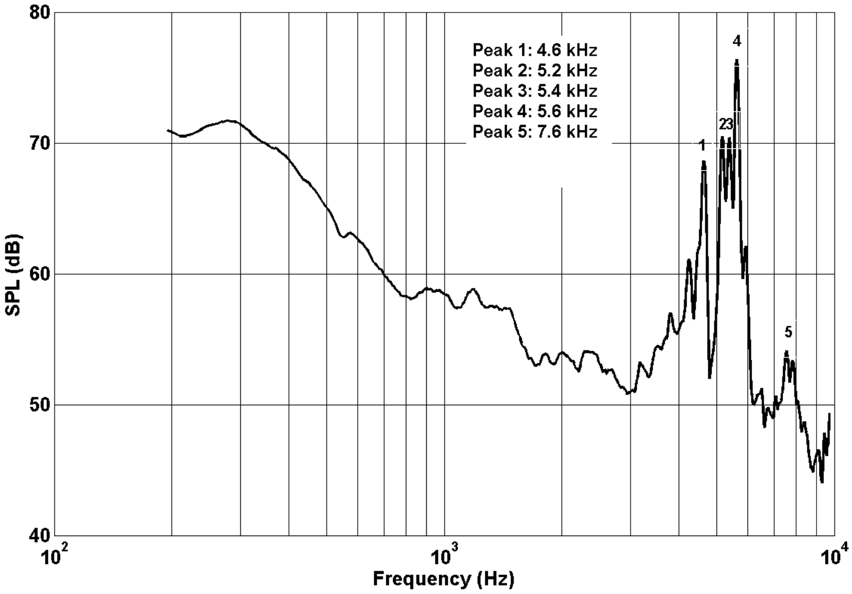

Figure 5.9: SPL in the far-field at AOA = 4 degrees, u_∞ = 25 m/s, showing five peaks.

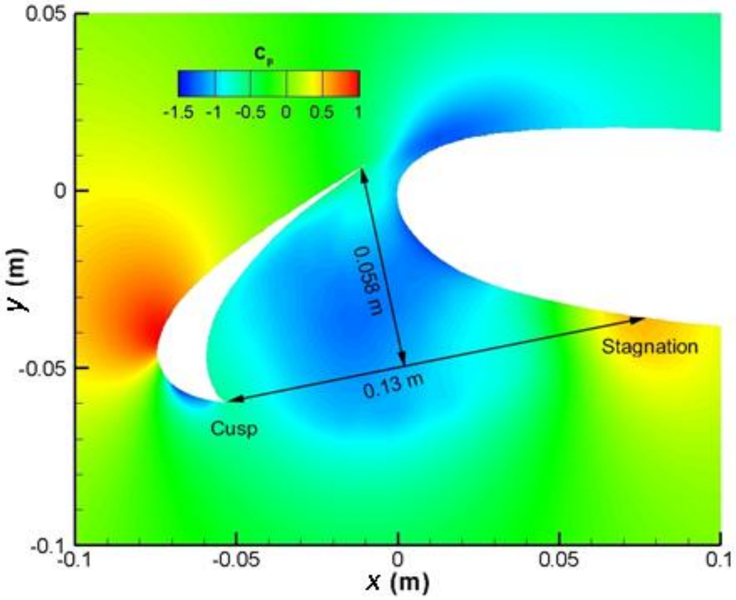

Figure 5.10: Static pressure coefficient distribution in the vicinity of slat at AOA = 4 degrees, u_∞ = 25 m/s.

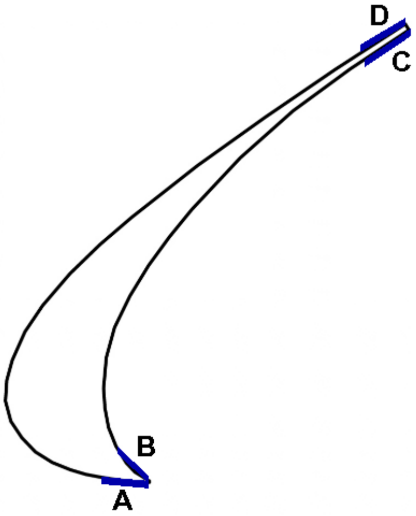

Figure 5.11: A strip with a thickness of 0.5 mm and a width of 10 mm mounted at positions A, B, C, D, which corresponded to both side surfaces of the cusp and trailing edge of the slat respectively, to measure the alteration of the slat noise.

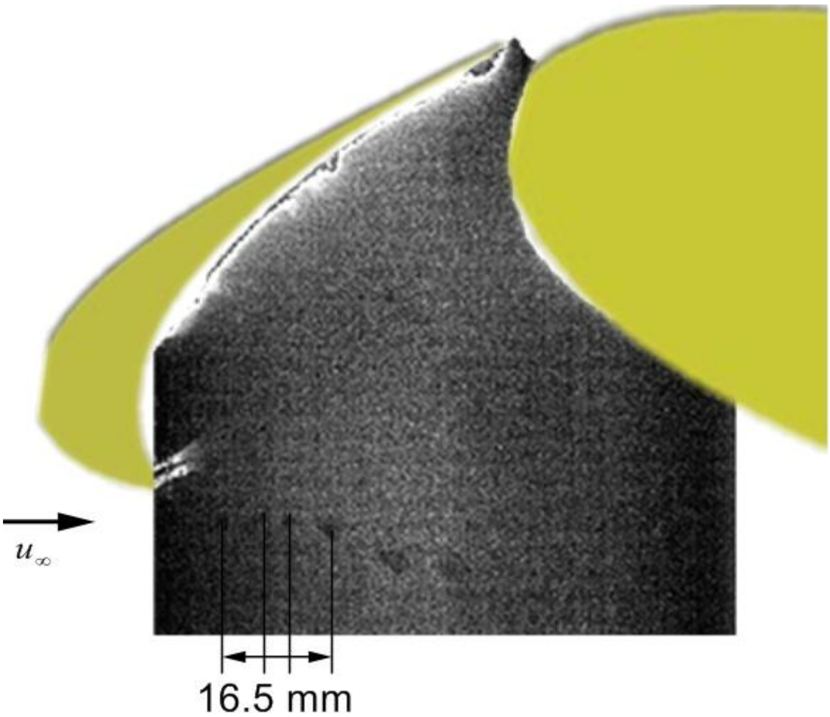

Figure 5.12: PIV visualization around the slat at AOA = 4 degrees, u_∞ = 15 m/s.

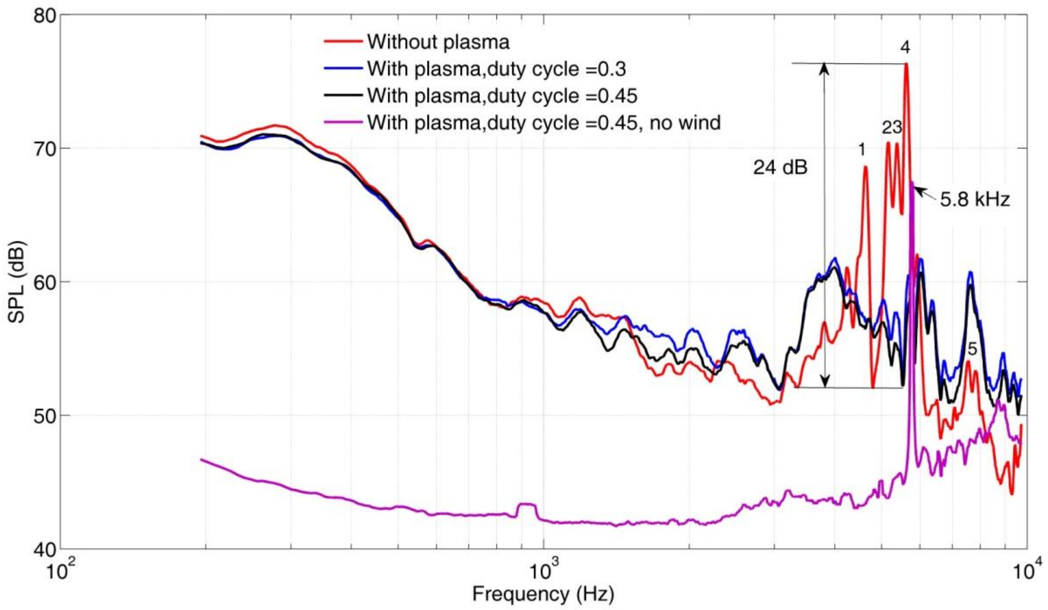

Figure 5.13: Slat noise reduction in the far-field due to plasma actuator at AOA = 4 degrees, u_∞ = 25 m/s.

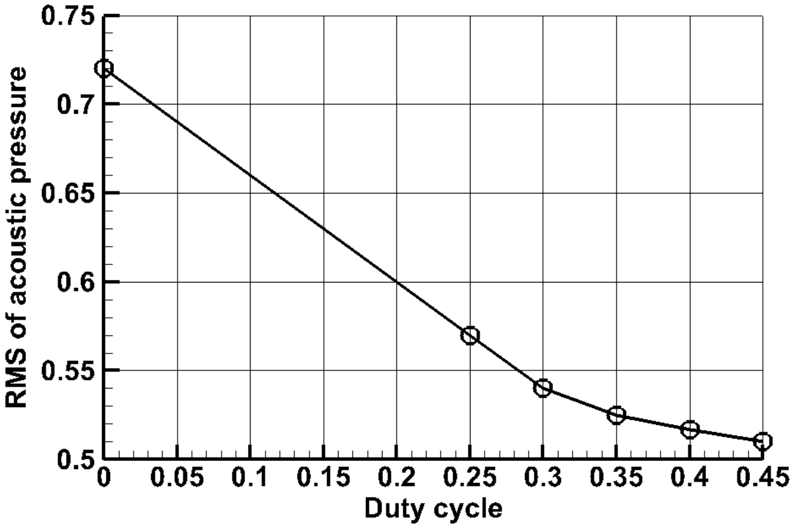

Figure 5. 14: RMS of acoustic pressure in the far-field with duty cycle at AOA = 4 degrees, u_∞ = 25 m/s.

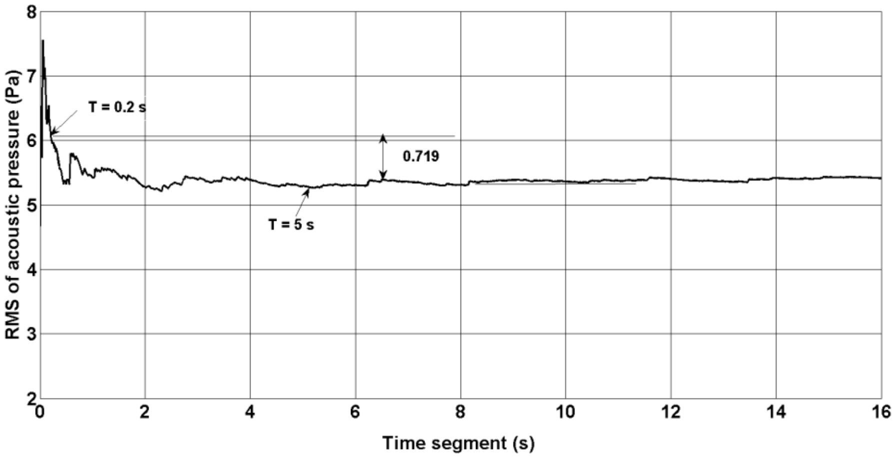

Figure 5.15: X-axis represents the time segment over which the RMS of acoustic pressure in the near-field is calculated.

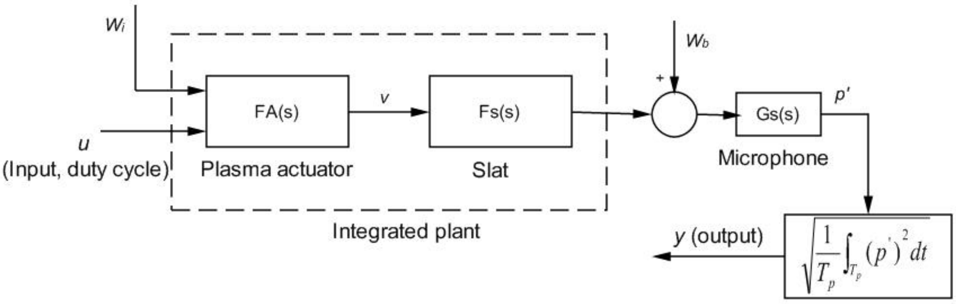

Figure 5.16: Open-loop control of the integrated plant which consisted of the plasma actuator and slat, W_i and W_b are the process noise and measurement noise respectively, T_p is the time step of 0.2 s.

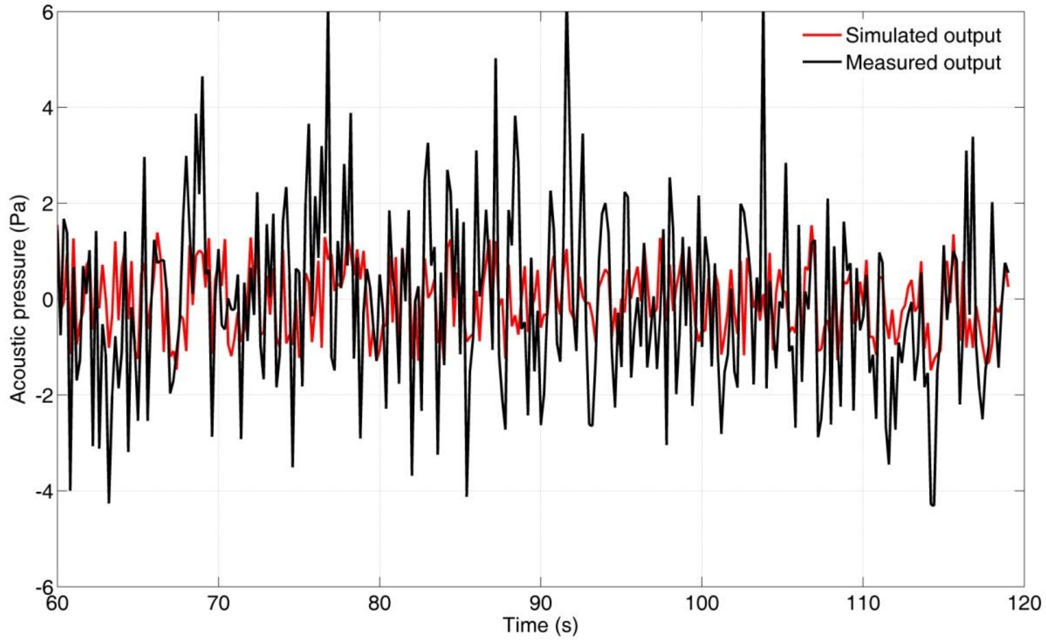

Figure 5.17: Comparison of simulated and measured output at AOA = 4 degrees, u_∞ = 25 m/s.

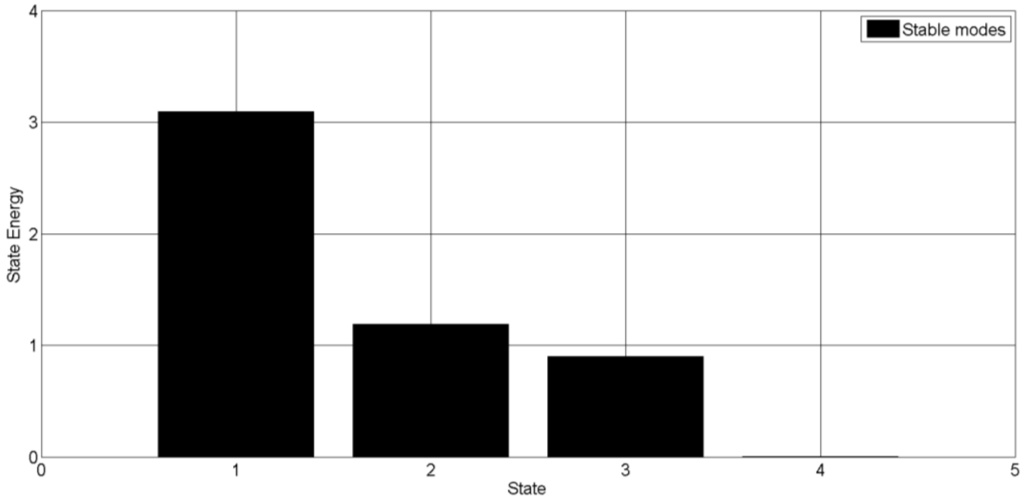

Figure 5.18: Four Hankel singular values of the identified model, the fourth value is minor when compared with the others.

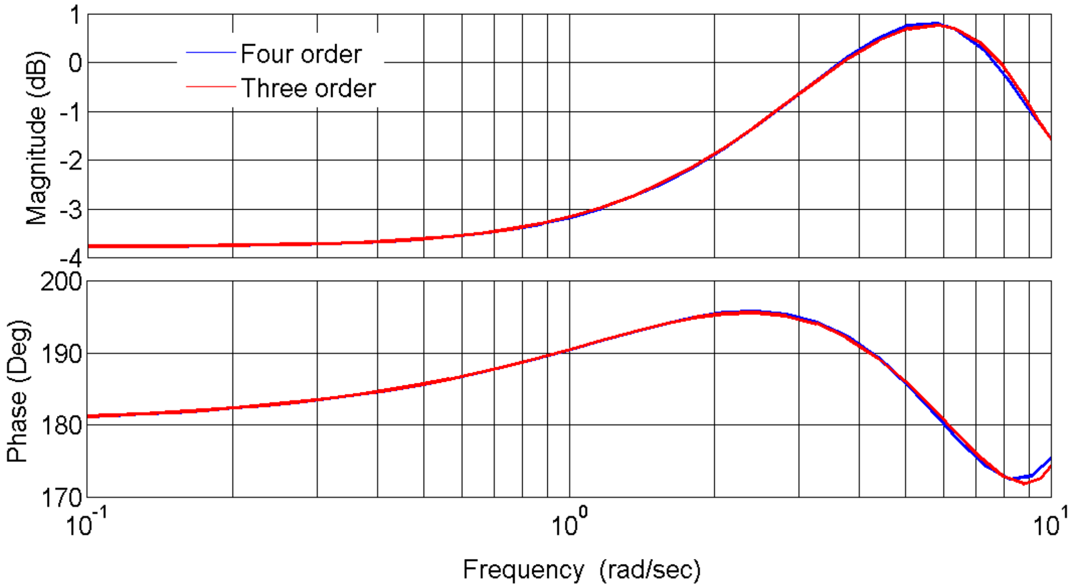

Figure 5.19: Comparison of Bode diagram between the original and the reduced model.

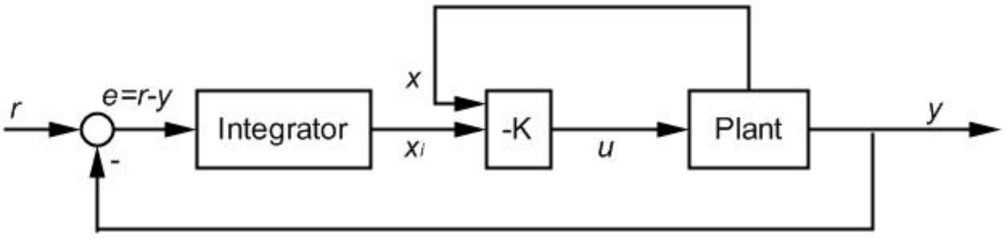

Figure 5.20: Schematic diagram for an LQI controller.

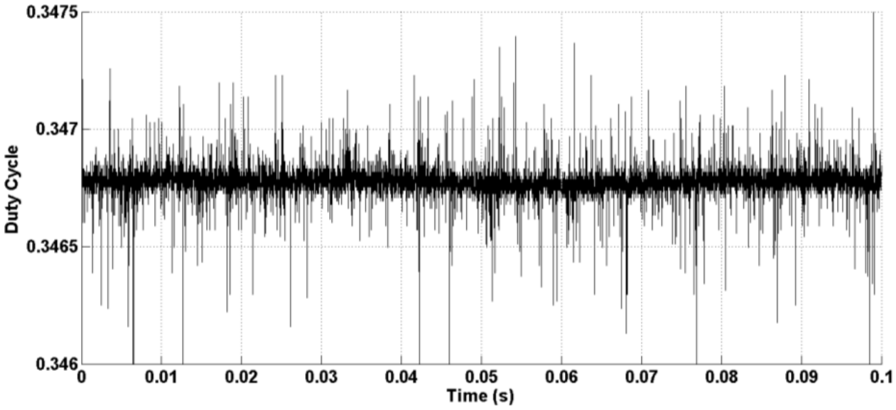

Figure 5.21: History of duty cycle fluctuations, which is measured at the signal port of the plasma power supply.

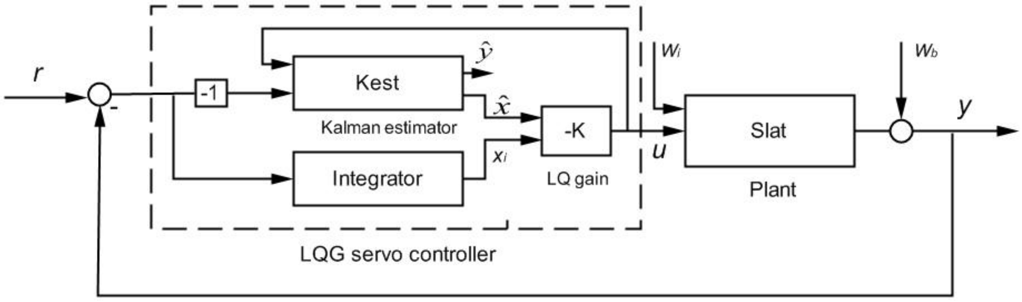

Figure 5.22: Schematic diagram of the LQG servo controller, in which *r* is the reference.

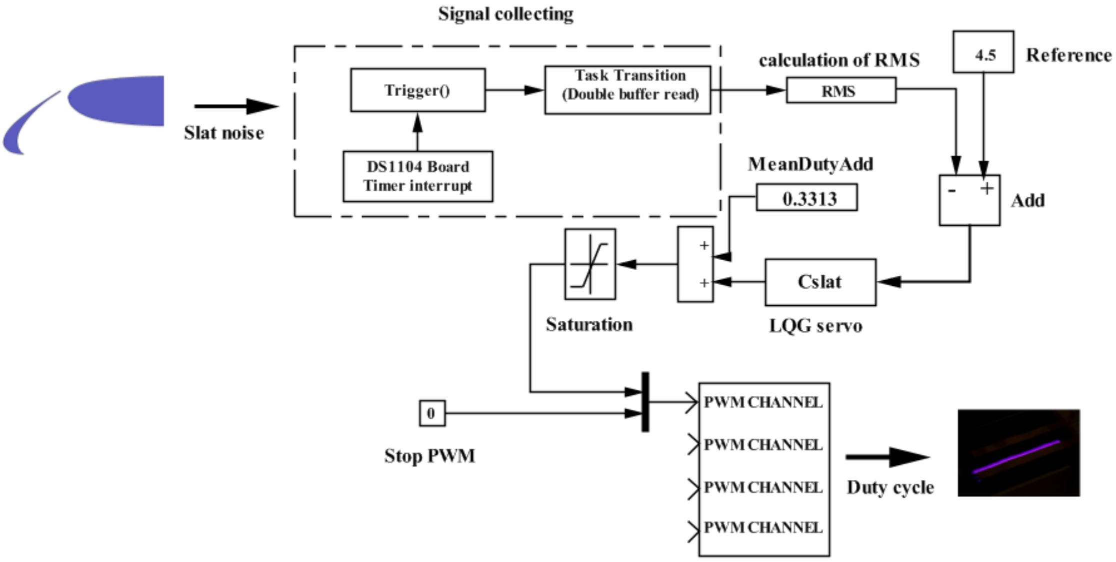

Figure 5.23: Implementation of the feedback control using the Simulink tools of Matlab together with the tools provided by the dSPACE system.

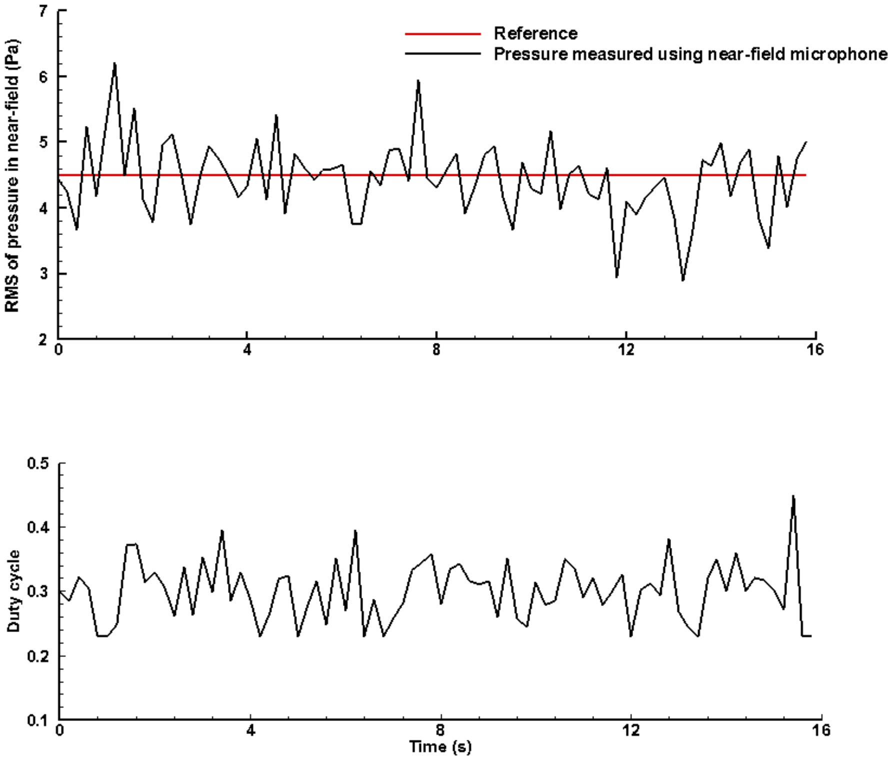

Figure 5.24: Time history of the RMS of pressure measured using the near-field microphone and the duty cycle as the control is activated. The reference was set to 4.5 Pa (represented by the red line), AOA = 4 degree and u_∞ = 25 m/s.

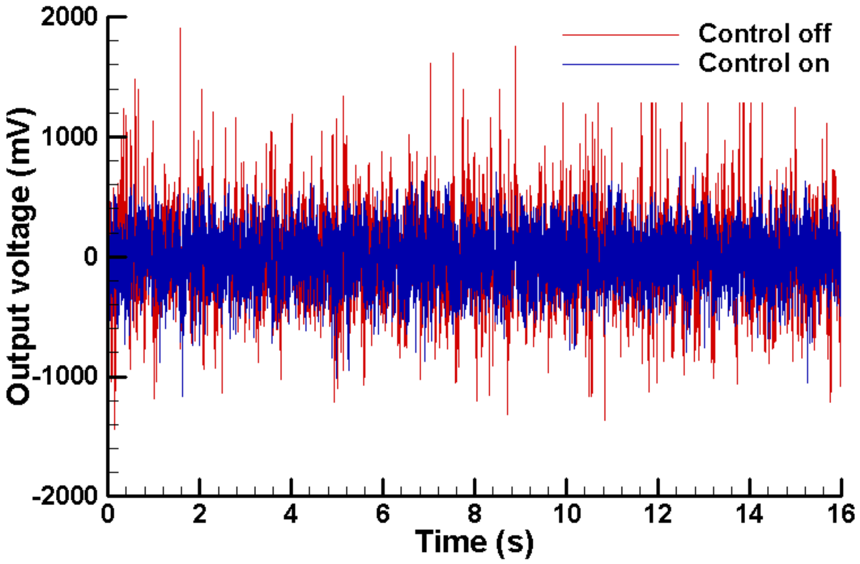

Figure 5.25: Comparison of time history of the output voltage of the far-field microphone at the output port of the amplifier between 'turn on' and 'turn off'.

Chapter 6

Summary and Future Work

In this final chapter the main results obtained are summarized and suggestions for future studies are given.

6.1 Summary

The objective of this work was to investigate the mechanisms behind slat noise and to develop methods to reduce the slat noise. Both experiments and numerical simulations were performed to achieve these goals. A wind tunnel model was designed, constructed and tested in a series of experiments, including aerodynamic, noise and control algorithm development tests. The wind tunnel model consisted of two elements, a slat and a main element. The deflection angle of the slat was set to 30 degrees. The chord of the main element was 350 mm and the chord for the slat was 88 mm. Most of the experiments and numerical simulations were performed at a freestream velocity of 25 m/s. This corresponded to a *Re* number of approximately 5.7×10^5 (based on the main element chord).

With respect to the noise mechanisms of slat noise, focus was concentrated on the relationship between the level of the slat noise and the angle of attack of the main element. The near-field noise was measured using an on-surface microphone, while the far-field noise was acquired using another microphone. The velocity in the slat region was measured using a hot-wire anemometer. PIV was employed to obtain the velocity field and fast PIV was used to visualize the dynamic processes of the flow around the slat. Numerical simulations were performed using the DDES technique. Based on the experimental and computational results, several conclusions were derived:

a) The slat noise level depended on the AOA. In this study, the noise level was at its lowest at an AOA = 6 degrees and highest at AOA = 8 degrees. Within an AOA range of 8 to 12 degrees, the slat noise level gradually decreased with the increasing AOA.

b) Several physical variables, including TKE, $\overline{|\omega_z|}$, $\overline{|\nabla \cdot L|}$ and p'_{rms}, were employed to locate the noise sources of the slat. At AOA = 8 degrees, the locations of the noise sources identified by those variables changed. It was suggested that the variable p'_{rms} was the most suitable one for locating the noise sources. It was found that the flow in the gap region represented a typical flow along a large curvature surface. The flow in the gap region was kept in a state of equilibrium by two kinds of force, the eccentricity force and the normal stress. This resulted in a gradual increase of velocity from the trailing edge of the slat to the leading edge of the main element.

c) As the angle of attack was increased to a certain value (8 degrees in this study), vortical structures were intermittently generated due to flow interaction, which occurred between the shear layer originating from the slat cusp and the flow convected from the stagnation line on the main element. Intense slat noise was produced as the vortical structures approached the slat cove surface. With the angle of attack increasing further, the slat noise became weak. This interaction effect became weaker as the shear layer deviated away from the surface of the main element. A pressure dipole, which corresponded to the first mode associated with the POD of the pressure fluctuations, was found in the slat gap region, with its axis aligned from the trailing edge of the slat to the leading edge of the main element, using the POD technique. The second mode indicated that the pressure fluctuations in the reattachment region and in the interaction region were spatially cross-related.

A slat noise attenuation method of air blowing was numerically tested; air was blown out on the suction surface of the slat near the trailing edge of the slat. The numerical simulations showed that the slat noise levels over most of the frequencies, especially above a *St* number of 7, were significantly attenuated. Meanwhile the lift coefficient was also increased significantly. A higher velocity magnitude of air blowing was found to result in a higher level of reduction in the slat noise. However the slat noise peak appearing in the slat noise spectrum at a *St* number of around 3.5 could not be reduced by the air blowing. The absolute values of the pressure fluctuations in the interaction region were also not obviously reduced, although the relative pressure fluctuations (non-dimensionalized by the local dynamic pressure) were decreased by the air blowing.

When a strip was mounted onto the pressure surface of the main element, the experimental results showed that the broadband noise of the slat was effectively reduced. The position and height of the strip had an influence on the level of reduction to some extent. The numerical simulations showed that the mean flow fields associated with the two cases of with and without the strip were similar. However the size of the circulation region was slightly increased by the strip. The static pressure near the leading edge of the main element was also increased due to the strip. This led to a drop in the lift coefficient of approximately 10 percent. The POD analysis of the pressure fluctuations showed that the pressure dipole, which corresponds to the first mode in the POD, was suppressed. The second mode was also fundamentally altered by the strip. This observation implied that the intermittently generated vortical structures and the flow oscillation in the slat cove were suppressed by this method as well. The flow oscillation in the slat cove can be regarded as a self-sustaining system containing multiple modes when no external forces acting on it. As there were sufficient disturbances externally acting on the system, the system turned into a forced oscillation system and its oscillation became weak. Consequently, the slat noise level was attenuated.

Several tonal noise components were found in the slat noise spectrum at an AOA = 4 degrees, u_∞ = 25 m/s. The PIV measurements showed that the dominant tone was closely associated with the vortex shedding off the slat cusp. To suppress the tonal components, a plasma actuator was developed, wherein the plasma intensity was regulated by means of a duty cycle signal which was generated by the dSPACE system. An optocoupler was also developed to shield the instruments from the strong ground cable interference. The tone was successfully suppressed by the use of a plasma actuator in an open-loop control system. The maximum reduction of 11 dB was achieved at a frequency of approximately 5.6 kHz. A feedback control system was also implemented to effectively attenuate the slat noise. Firstly, the plant of the slat noise was identified by an ARX algorithm, wherein a total of 600 input/output data pairs were used. The input data were generated from the duty cycle and the output data was the RMS of the acoustic pressure. It was found that a polynomial model with three poles and two zeros could preferably describe the plant. Based on the indentified model, a quasi-static feedback control system with a LQG servo controller was developed. The experimental results showed that the controller could work effectively to suppress the slat noise.

6.2 Future Work

Although the main features of slat noise have been investigated, and three methods (air blowing, adding a strip and plasma actuation) have been proven to be effective in the reduction of the slat noise, some further work still needs to be done. For example:

- The air blowing method needs to be experimentally verified. It would also be beneficial to conduct future tests with the air blowing employed on the cove surface near the trailing edge of the slat.
- In the strip method, the strip had an obviously negative effect on the aerodynamic performance of the wing, wherein the lift coefficient was decreased by approximately 10 percent. Various geometric strips could be tested in the future with the aim of achieving a working compromise between the reduction in the slat noise and the aerodynamic performance of the wing.
- The plasma actuator mainly suppressed the tonal components of the slat noise, whilst merely exerting a slight effect on the broadband noise. It is therefore necessary to improve the authority of the plasma actuator. Some appropriate positions at which the actuator could be mounted are the suction surface or cove surface near the trailing edge of the slat.

Bibliography

[1] Goldstein, M. E., *Aeroacoustics*. New York: McGraw-Hill International Book Company, 1976.

[2] Busquin, M. A., "European aeronautics: A vision for 2020, meeting society's needs and winning global leadership," Rept. of the Group of Personalities, KI-34-01-827-EN-C, January 2001.

[3] Khorrami, M. R., Choudhari, M. M., Singer, B. A., Lockard, D. P., and Streett, C. L., "In search of the physics: The interplay of experiment and computation in slat aeroacoustics," AIAA Paper 2003-0980, 41st Aerospace Sciences Meeting, Reno, NV, U.S.A, January 2003.

[4] Davy, R., and Remy, H., "Airframe noise characteristics of a 1/11 scale airbus model," AIAA Paper 1998-2335, 4th AIAA/CEAS Aeroacoustics Conference, Toulouse, France, June 1998.

[5] Dobrzynski, W., Nagakura, K., Gehlhar, B., and Buschbaum, A., "Airframe noise studies on wings with deployed high-lift Devices," AIAA Paper 1998-2337, 4th AIAA/CEAS Aeroacoustics Conference, Toulouse, France, June 1998.

[6] Guo, Y. P., and Joshi, M. C., "Noise characteristics of aircraft high hift systems," *AIAA Journal*, Vol. 41, No. 7, 2003, pp. 1247-1256.

[7] Lighthill, M. J., "On sound generated aerodynamically, I: general theory," *Proceedings of the Royal Society of London,*, Vol. A211, 1952, pp. 564-587.

[8] Lighthill, M. J., "On sound generated aerodynamically, II: turbulence as a source of sound," *Proceedings of the Royal Society of London,*, Vol. A222, 1954, pp. 1-32.

[9] Ffowcs Williams, J. E., and Hawkings, D. L., "Sound generated by turbulence and surfaces in arbitrary motion," *Philosophical Transactions of the Royal Society of London*, Vol. A264, No. 1151, 1969, pp. 321-342.

[10] Powell, A., "Some aspects of aeroacoustics: from Rayleigh until today," *Journal of Vibration and Acoustics*, Vol. 112, 1990, pp. 145-159.

[11] Howe, M., "Contributions to the theory of aerodynamic sound, with application to excess jet noise and the theory of the flute " *Journal of Fluid Mechanism*, Vol. 71, 1975, pp. 625-673.

[12] Powell, A., "Aerodynamic noise and the plane boundary," *Journal of Acoustic Society of Amrican*, Vol. 32, No. 8, 1960, pp. 982-900.

[13] Singer, B. A., and Guo, Y. P., "Development of computational aeroacoustics tools for airframe noise calculations," *International Journal of Computational Fluid Dynamics*, Vol. 18, No. 6, 2004, pp. 455-469.

[14] Curle, N., "The influence of solid boundaries upon aerodynamic sound," *Soc. London Ser.*, Vol. A231, No. 1187, 1955, pp. 505-514.

[15] Pilon, A. R., and Lyintzis, A. S., "Development of an improved Kirchhoff methodfor jet aeroacoustics," *AIAA Journal*, Vol. 36, No. 5, 1998, pp. 783-290.

[16] Lockard, D. P., Singer, B. A., and Brentner, K. S., "Simulation of acoustic scattering from a trailing edge.," *Journal of Sound and Vibration*, Vol. 230, No. 3, 2000, pp. 541-560.

[17] Wang, M., Lele, S. K., and Moin, P., "Computation of quadrupole noise using acoustic analogy.," *AIAA Journal*, Vol. 34, No. 11, 1996, pp. 2247-2254.

[18] Brentner, K. S., and Farassat, F., "Modeling aerodynamically generatedsoundof helicopter rotors.," *Progress Aerospace Science*, Vol. 39, 2003, pp. 83-120.

[19] Lyrintzis, A. S., "Review: the use of Kirchhoff's method computational aeroacoustics," *Journal of Fluids Engineering*, Vol. 116, 1994, pp. 665–676

[20] Soderman, P. T., Kafyeke, F., Burnside, N. J., Chandrasekharan, R., Jaeger, S. M., and Boudreau, J., "Airframe noise study of a CRJ-700 aircraft model in the NASA AMES 7 by 10 foot wind tunnel No. 1," AIAA Paper 2002-2406, 8th AIAA/CEAS Aeroacoustics Conference, Breckenridge, CO, June 2002.

[21] Dobrzynski, W., and Pott-Pollenske, M., "Slat noise source studies for farfield noise prediction," AIAA Paper 2001-2158, 7th AIAA/CEAS Aeroacoustics Conference and Exhibit, Maastricht, Netherlands, May 2001.

[22] Chow, L. C., Mau, K., and Remy, H., "Landing gears and high lift devices airframes noise research," AIAA Paper 2002-2408, 8th AIAA/CEAS Aeroacoustics Conference & Exhibit, Breckenridge, Colorado, June 2002.

[23] Choudhari, M. M., and Khorrami, M. R., "Effect of three-dimensional shear-layer structures on slat cove unsteadiness," *AIAA Journal*, Vol. 45, No. 9, 2007, pp. 2174-2185.

[24] Imamura, T., Enomoto, S., Yokokawa, Y., and Yamamoto, K., "Three-dimensional unsteady flow computations around a conventional slat of high-lift devices," *AIAA Journal*, Vol. 46, No. 5, 2008, pp. 1045-1053.

[25] Dobrzynski, W., "Almost 40 years of airframe noise research: What did we achieve?," *Journal of Aircraft*, Vol. 47, No. 2, 2010, pp. 353-367.

[26] Tam, C. K. W., and Pastouchenko, N., "Gap Tones," *AIAA Journal*, Vol. 39, No. 8, 2001, pp. 1442-1448.

[27] Roger, M., and Perennes, S., "Low-frequency noise sources in two-dimensional high-lift devices," AIAA Paper 2000-1972, 6th AIAA/CEAS Aeroacoustics Conference, Lahaina, HI, U.S.A, June 2000.

[28] Rossiter, J. E., "Wind-tunnel experiments on the flow over rectangular cavities at subsonic and transonic speeds," Aeronautical Research Council Report 3428,

[29] Molin, N., and Roger, M., "The use of Amiet's methods in predicting the noise from 2D high-lift devices," AIAA Paper 2000-2064, 6th AIAA/CEAS Aeroacoustics Conference, Lahaina, HI, June 2000.

[30] Singer, B. A., Lockard, D. P., and Brentner, K. S., "Computational aeroacoustic analysis of slat trailing-edge flow," *AIAA Journal*, Vol. 38, No. 9, 2000, pp. 1558-1564.

[31] Dobrzynski, W., Gehlhar, B., and Buchholz, H., "Model and full scale high-lift wing wind tunnel experiments dedicated to airframe noise reduction," *Aerospace Science and Technology*, Vol. 5, 2001, pp. 27-33.

[32] Khorrami, M. R., and Lockard, D. P., "Effects of geometrical details on slat noise generation and propagation," AIAA Paper 2006-2664, 12th AIAA/CEAS Aeroacoustics Conference, Cambridge, Massachusetts, May 2006.

[33] Horne, W. C., James, K. J., Arledge, T. K., and Soderman, P. T., "Measurements of 26%-scale 777 Airframe Noise in the NASA Ames 40- by 80 Foot Wind Tunnel," AIAA Paper 2005-2810, 11th AIAA/CEAS Aeroacoustics Conference (26th AIAA Aeroacoustics Conference), Monterey, California, May 2005.

[34] Kolb, A., Faulhaber, R., Drobietz, R., and Grünewald, M., "Aeroacoustic wind tunnel study on a Two-dimensional High-lift configuration,," AIAA Paper 2007-3447, AIAA/Confederation of European Aerospace Societies, May 2007.

[35] Imamura, T., Ura, H., Yokokawa, Y., Enomoto, S., Yamamoto, K., and Hirai, T., "Designing of slat cove filler as a noise reduction device for leading-edge slat," AIAA Paper 2007-3473, 13th AIAA/CEAS Aeroacoustics Conference, Rome, Italy, May 2007.

[36] Pott-Pollenske, M., "Results from noise testing of slat and wing leading edge liners in AWB," Silence(r) Consortium D1.6-5.2-02, 2003.

[37] Ma, Z., Smith, M. G., Richards, S. K., and Zhang, X., "Attenuation of slat trailing edge noise using acoustic liners," *aeroacoustics*, Vol. 5, No. 4, 2006, pp. 311-333.

[38] Crighton, D. G., "Airframe noise in aeroacoustics of flight vehicles: theory and practice," NASA RP 1258, 1991.

[39] Pott-Pollenske, M., Werner, D., Heino, B., Sebastien, G., Gerd, S., and Ullrich, F., "Airframe noise characteristics from flyover measurements and prediction," AIAA Paper 2006-2567, 12th AIAA/CEAS Aeroacoustics Conference, Cambridge, Massachusetts, May 2006.

[40] Lockard, D. P., and Lilley, G. M., "The airframe noise reduction challenge," NASA/TM-2004-213013, 2004.

[41] Mueller, T. J., *Aeroacoustic measurements*. London: Springer, 2002.

[42] Jacob, M. C., Robert, G., Fremion, N., and Guerrand, S., "In-flow acoustic measurements on high speed train," AIAA Paper 2000-2011, 6th AIAA/CEAS aeroacoustic conference, Lahaina HI,

[43] Vincent, F., Jean, B., and Renaud, D., "Determination of acoustic directivity from microphone array measurements using correlated monopoles," AIAA Paper 2008-2855, 14th AIAA/CEAS Aeroacoustics Conference, Vancouver, Canada, May 2008.

[44] Takao, S., "Generalized inverse beam-forming algorithm resolving coherent/incoherent, distributed and multipole sources," AIAA Paper 2008-2954, 14th AIAA/CEAS Aeroacoustics Conference, Vancouver, Canada, May 2008.

[45] Lars, K., and Klaus, E., "Microphone-array processing for wind-tunnel measurements with strong background noise," AIAA Paper 2008-2907, 14th AIAA/CEAS Aeroacoustics Conference, Vancouver, Canada, May 2008.

[46] Tam, C. K. W., "Computational aeroacoustics: An overview of computational challenges and applications," *International Journal of Computational Fluid Dynamics*, Vol. 18, No. 6, 2004, pp. 547-567.

[47] Colonius, T., and Lele, S. K., "Computational aeroacoustics: progress on nonlinear problems of sound generation," *Progress in Aerospace Sciences*, Vol. 40, 2004, pp. 345-416.

[48] Ewert, R., and Emunds, R., "CAA slat noise studies applying stochastic sound sources based on solenoidal digital filters," AIAA Paper 2005-2862, 11th AIAA/CEAS Aeroacoustics Conference, Monterey, California, May 2005.

[49] Colonius, T., and Lele, S. K., "Computational aeroacoustics: progress on nonlinear problems of soundgeneration," *Progress in Aerospace Sciences*, Vol. 40, 2004, pp. 345–416.

[50] Wang, M., Freund, J. B., and Lele, S. K., "Computational Prediction of Flow-Generated Sound," *Annu. Rev. Fluid Mech.*, Vol. 38, 2006, pp. 483-512.

[51] Bogey, C., Bailly, C., and Juve, D., "Computation of flow noise using source terms in linearized Euler's equations," *AIAA Journal*, Vol. 40, No. 2, 2002, pp. 235-243.

[52] Piomelli, U., and Balaras, E., "Wall-layer models for large-eddy simulations," *Annu. Rev. Fluid Mech.*, Vol. 34, 2002, pp. 349-374.

[53] Caruelle, B., and Ducros, F., "Detached-eddy simulations of attached and detached boundary layers," *International Journal of Computational Fluid Dynamics*, Vol. 17, No. 6, 2003, pp. 433-451.

[54] Spalart, P. R., "Trends in turbulence treatments," AIAA Paper 2000-2306, Computational Fluid Dynamics Symposium, Denver, Colorado, USA, June 2000.

[55] Spalart, P. R., "Strategies for turbulence modelling and simulations," *International Journal of Heat and Fluid Flow*, Vol. 21, 2000, pp. 252-263.

[56] Spalart, P. R., and Allmaras, S. R., "An one-equation turbulence model for aerodynamic flows," AIAA Paper 1992-0439, 30th Aerospace Sciences Meeting and Exhibit, Reno, NV, Jan. 1992.

[57] Trefethen, L. N., "Group velocity in finite difference schemes," *Siam Review* Vol. 24, 1982, pp. 113-136.

[58] Tam, C. K. W., Webb, J. C., and Dong, Z., "A study of the short wave components in computational acoustics," *Journal of Computational Acoustics* Vol. 1, 1993, pp. 1-30.

[59] Kurbatskii, K. A., and Tam, C. K. W., "Direct numerical simulation of automobile cavity tone," NASA CP-2000-209790, 2000.

[60] Konig, D., Koh, S. R., Schroder, W., and Meinke, M., "Slat noise source identification," AIAA paper 2009-3100, 30th AIAA Aeroacoustics Conference, Miami, Florida, May 2009.

[61] Andreou, C., Graham, W., and Shin, H. C., "Aeroacoustic study of airfoil leading edge high-lift devices," AIAA Paper 2006-2515, 27th AIAA Aeroacoustics Conference, Cambridge, Massachusetts, May 2006.

[62] Arnott, A., Schneider, G., Neitzke, K. P., Agocs, J., Sammler, B., Schroder, A., and Kompenhans, J., "Multi-window PIV for high-lift measurements," 20th International Congress on Instrumentation in Aerospace Simulation Facilities ICIASF, Goettingen, August 2003.

[63] Spalart, P. R., Deck, S., Shur, M. L., Squires, K. D., Strelets, M. K., and Travin, A., "A new version of detached-eddy simulation, resistant to ambiguous grid densities," *Theor. Comput. Fluid Dyn.*, Vol. 20, 2006, pp. 181-195.

[64] Deck, S., "Zonal-Detached-Eddy simulation of the flow around a high-lift configuration," *AIAA Journal*, Vol. 43, No. 11, 2005, pp. 2372-2384.

[65] Choudhari, M. M., and Khorrami, M. R., "Slat cove unsteadiness: effect of 3D flow structures," AIAA Paper 2006-0211, 44th AIAA Aerospace Sciences Meeting and Exhibit, Reno, NV, Jan. 2006.

[66] Lockard, D. P., and Choudhari, M. M., "Noise Radiation from a Leading-Edge Slat," AIAA Paper 2009-3101, 15th AIAA/CEAS Aeroacoustics Conference, Miami, Florida, May 2009.

[67] Casper, J. H., Lockard, D. P., Mehdi R. Khorrami, M. R., and Streett, C. L., "Investigation of volumetric sources in airframe noise simulations," AIAA Paper 2004-2805, 10th AIAA/CEAS Aeroacoustics Conference,

[68] Dobrzynski, W., Ewert, R., Pott-Pollenske, M., Herr, M., and Delfs, J., "Research at DLR towards airframe noise prediction and reduction," *Aerospace Science and Technology*, Vol. 12, 2008, pp. 80-90.

[69] Khorrami, M. R., and Singer, B. A., "Time-accurate simulations and acoustic analysis of slat free shear layer," *AIAA Journal*, Vol. 40, No. 7, 2002, pp. 1284-1291.

[70] Khorrami, M. R., Choudhari, M. M., Singer, B. A., Lockard, D. P., and Streett, C. R., "In search of the physics: The interplay of experiment and computation in slat aeroacoustics," AIAA Paper 2003-0980, 41st Aerospace Sciences Meeting & Exhibit, Reno, Nevada, January 2002.

[71] Lilley, G. M., "The radiated noise from isotropic turbulence revisited," NASA Contract Report 93-75, 1993.

[72] Sarkar, S., and Hussaini, M. Y., "Computation of the sound generated by isotropic turbulence," NASA Contract Report 93-74, 1993.

[73] Yokokawa, Y., Imamura, T. I., Ura, H., Uchida, H., Ito, T., and K., Y., "Studies on airframe noise generation at high-lift devices in relation to aerodynamic performances," AIAA Paper 2008-2960, 14th AIAA/CEAS Aeroacoustics Conference, Vancouver, British Columbia, May 2008.

[74] Takeda, K., Zhang, X., and Nelson, P. A., "Unsteady aerodynamics and aeroacoustics of a high-lift device configuration," AIAA Paper 2002-0570, January 2002.

[75] McGinley, C. B., Ander, J. B., and Spaid, F. W., "Measurements of Reynolds stress profiles on a high-lift airfoil," AIAA Paper 1998-2620, 16th Applied Aerodynamics Conference, Albuquerque, NM, June 1998.

[76] Paschal, K., Jenkins, L., and Yao, C., "Unsteady slat wake characteristics of a 2-D high-lift configuration," AIAA Paper 2000-0139, 38th Aerospace Sciences Meeting and Exhibit, Reno, Nevada, January 2000.

[77] Lumley, J. L., *The structure of inhomogeneous turbulent flows*. Nauka, Moscow and Toulouse, France: Atmospheric Turbulence And Radio Wave Propagation, 1967.

[78] Lewin, G., and Haj-hariri, H., "Reduced-order modeling of a heaving airfoil," *AIAA Journal*, Vol. 43, No. 2, 2005, pp. 270-283.

[79] Arad, B., Gazit, Y., and Ludmirsky, A., "A sliding discharge device for producing cylindrical shock waves," *Journal of Physics*, Vol. 77, 1987, pp. 360-367.

[80] Zouzou, N., Takashima, K., Moreau, E., and Mizuno, A., "Sliding discharge study in axisymmetric configuration," 28th ICPIG, Prague, Czech Republic, 2007.

[81] Louste, C., Artana, G., Moreau, E., and Touchard, G., "Sliding discharge in air at atmospheric pressure: electrical properties," *Journal of Electrost*, Vol. 63, 2005, pp. 615-620.

[82] Kunhardt, E., "Generation of large-volume, atmospheric-pressure, nonequilibrium plasmas," *IEEE Transactions on Plasma Science*, Vol. 28, No. 1, 2000, pp. 189-200.

[83] Louis, N. C., and Mark, S., "Actuators for active flow control," *Annual Review of Fluid Mechanics*, Vol. 43, 2011, pp. 247-272.

[84] Corke, T. C., Post, M. L., and Orlov, D. M., "SDBD plasma enhanced aerodynamics: concepts, optimization and applications," *Progress in Aerospace Sciences*, Vol. 43, No. 7, 2007, pp. 193-217.

[85] Moreau, E., "Airflow control by non-thermal plasma actuators," *Journal of Physics*, Vol. 40, 2007, pp. 605-636.

[86] Corke, T. C., Enloe, C. L., and P.W., S., "Dielectric barrier discharge plasma actuators for flow control," *Annual Review of Fluid Mechanics*, Vol. 42, 2010, pp. 505-529.

[87] Corke, T. C., and Matlis, E., "Phased plasma arrays for unsteady flow control," *Fluids 2000 Conference and Exhibit*, Vol. 2000-2323, 2000,

[88] Orlov, D. M., "Modelling and simulation of single dielectric barrier discharge plasma actuators." Vol. PhD thesis, University of Notre Dame, 2006.

[89] Enloe, C. L., McLaughlin, T. E., VanDyken, R. D., Kachner, K. D., Jumper, E. J., and Corke, T. C., "Mechanisms and responses of a single dielectric barrier plasma actuator: plasma morphology," *AIAA Journal*, Vol. 42, No. 3, 2004, pp. 589–594.

[90] Pons, J., Moreau, M., and Gerard, T., "Asymmetric surface dielectric barrier discharge in air at atmospheric pressure: electrical properties and induced airflow characteristics," *Journal of Physics, D: Applied Physics*, Vol. 38, 2005, pp. 3635-3642.

[91] Forte, M., Jolibois, J., Pons, J., Moreau, E., Touchard, G., and Cazalens, M., "Optimization of a dielectric barrier discharge actuator by stationary and non-stationary measurements of the induced flow velocity: application to flow control," *Experiments in Fluids*, Vol. 43, No. 6, 2007, pp. 917-928.

[92] Santhanakrishnan, A., and Jacob, J. D., "Flow control with plasma synthetic jet actuators," *Journal of Physics, D: Applied Physics*, Vol. 40, No. 3, 2007,

[93] Orlov, D. M., and Corke, T. C., "Numerical simulation of aerodynamic plasma actuator effects," AIAA Paper 2005-1083, 43rd AIAA Aerospace Sciences Meeting and Exhibit, Reno, Nevada, USA, Jan., 2005.

[94] Thomas, F., Corke, T., Iqbal, M., Kozlov, A., and Shatzman, D., "Optimization of SDBD plasma actuators for active aerodynamic flow control," *AIAA Journal*, Vol. 47, No. 9, 2009, pp. 2169-2175.

[95] Orlov, D. M., Thomas, A., Chuan, H., Hesham, O., and Corke, T. C., "Modeling and experiment of leading edge separation control using SDBD plasma actuators," AIAA paper 2007-0877, 45th AIAA Aerospace Sciences Meeting and Exhibit, Reno, Nevada, USA, Jan. 2007.

[96] Chuan, H., Corke, T. C., and Patel, M. P., "Plasma flaps and slats: an application of weakly ionized plasma actuators," *Journal of Aircraft*, Vol. 46, No. 3, 2009, pp. 864-873.

[97] Flint, T., Thomas, C., Muhammad, I., Alexey, K., and David, S., "Optimization of dielectric barrier discharge plasma actuators for active aerodynamic flow control," *AIAA Journal*, Vol. 47, No. 9, 2009, pp. 2169-2178.

[98] James, M., Wesley, B., Woszidlo, R., Taubert, L., and Wygnanski, I., "Single dielectric barrier discharge plasma actuators for improved airfoil performance," *Journal of Aircraft*, Vol. 46, No. 3, 2009, pp. 847-855.

[99] Chan, S., Zhang, X., and Gabriel, S., "The attenuation of cavity tones using plasma actuators,," *AIAA Journal*, Vol. 45, No. 7, 2007, pp. 1525-1538.

[100] Huang, X., Chan, S., and Zhang, X., "An atmospheric plasma actuator for aeroacoustic applications," *IEEE Transactions on Plasma Science*, Vol. 35, No. 3, 2007, pp. 693-695.

[101] Huang, X., Chan, S., Zhang, X., and Gabriel, S., "Variable structure model for flow-induced tonal noise control with plasma actuators," *AIAA Journal*, Vol. 46, No. 1, 2008, pp. 241-250.

[102] Huang, X., Zhang, X., and Yong, L., "Broadband flow-induced sound control using plasma actuators," *Journal of Sound and Vibration*, Vol. 329, No. 13, 2010, pp. 2477-2489.

[103] Seraudie, A., Aubert, E., Naudé, N., and Cambronne, J., "Effect of plasma actuators on a flat plate laminar boundary layer in subsonic conditions," AIAA paper 2006-3350, 3rd AIAA Flow Control Conference, San Francisco, USA, June 2006.

[104] Cattafesta, L. N., Williams, D. R., Rowley, C. W., and Alvi, F. S., "Review of active control of flow-induced cavity resonance," AIAA Paper 2003-3567, 33rd AIAA Fluid Dynamics Conference and Exhibit, Orlando, Florida, June, 2003.

[105] Cattafesta, L. N., and Williams, D. R., "Dynamics and control of High-Reynolds-Number flow over open cavities," *Annual Review of Fluid Mechanics*, Vol. 38, 2006, pp. 251-276.

[106] Cattafesta, L. N., Song, Q., Williams, D. R., Rowley, C. W., and Alvi, F. S., "Active control of flow-induced cavity oscillations," *Progress in Aerospace Sciences*, Vol. 44, 2008, pp. 479-502.

[107] Smith, B., Welteren, T., Maines, B., Shaw, L., Stanek, M., and Grove, J., "Weapons bay acoustic suppression from rod spoilers," AIAA Paper 2002-662, 40th AIAA Aerospace Sciences Meeting and Exhibit, Reno, Nevada, Jau. 2002.

[108] Ukeiley, L., Ponton, M., Seiner, J., and Jansen, B., "Suppression of pressure loads in cavity flows," *AIAA Journal*, Vol. 42, No. 1, 2004, pp. 70-79.

[109] Rowley, C. W., Williams, D. R., Colonius, T., Murray, R. M., and Macmynowski, D. G., "Linear models for control of cavity flow oscillations," *Journal of Fluid Mechanics,*, Vol. 547, 2006, pp. 317-330.

[110] Yan, P., Debiasi, M., Yuan, X., Little, J., Ozbay, H., and Samimy, M., "Experimental study of linear closed-loop control of subsonic cavity flow," *AIAA Journal*, Vol. 44, No. 5, 2006, pp. 929-938.

[111] Caraballo, E., Kasnakoglu, C., Serrani, A., and Samimy, M., "Control input separation methods for reduced-order model-based feedback flow control," *AIAA Journal*, Vol. 46, No. 9, 2008, pp. 2306-2322.

[112] Kihwan, K., Marco, D., Ryan, S., Andrea, S., and Mo, S., "Dynamic compensation of a synthetic jetlike actuator for closed-loop cavity flow control," *AIAA Journal*, Vol. 46, No. 1, 2008, pp. 232-240.

[113] Alexander, B., Denis, S., and Peter, J. S., "Closed-loop control of an open cavity flow using reduced-order models," *Journal of Fluid Mechanics,*, Vol. 641, 2009, pp. 1-50.

[114] Kihwan, K., Cosku, K., Andrea, S., and Mo, S., "Extremum-seeking control of subsonic cavity flow," *AIAA Journal*, Vol. 47, No. 1, 2009, pp. 195-205.

[115] Samimy, M., Debiasi, M., Carabllo, E., Serrani, A., Yuan, X., Little, J., and Myatt, J. H., "Feedback control of subsonic cavity flows using reduced-order models," *Journal of Fluid Mechanics,*, Vol. 579, 2007, pp. 315-346.

[116] Kaepernick, K., Koop, L., and Ehrenfried, K., "Investigation of the unsteady flow field inside a leading edge slat cove," AIAA paper 2005-2813, 26th AIAA Aeroacoustics Conference, Monterey, California, May 2005.

[117] Wiltse, J. M., and Glezer, A., "Direct excitation of small scale motions in free shear flows," *Physics of Fluids*, Vol. 10, 1998, pp. 2026-2036.

[118] Cabell, R. H., Kegerise, M. A., Cox, D. E., and Gibbs, G. P., "Experimental feedback control of flow-induced cavity tones," *AIAA Journal*, Vol. 44, No. 8, 2006, pp. 1807-1815.

[119] Shaw, L., and Northcraft, S., "Closed loop active control for cavity resonance," AIAA Paper 1999-1902, 5th AIAA/CEAS Aeroacoustics Conference and Exhibit, Bellevue, Washington, May 1999.

[120] Samimy, M., Debiasi, M., Caraballo, E., and Malone, J. L., J., "Exploring strategies for closed-loop cavity flow control," AIAA Paper 2004-0576, 42nd AIAA Aerospace Sciences Meeting and Exhibit, Reno, Nevada, Jan. 2004.

[121] Goodwin, G. C., Graebe, S. F., and Salgado, M. E., *Control system design*. Upper saddle river, New Jersey: Prentice-Hall, Inc., 2001.

[122] Lewis, F. L., *Optimal estimation*. New York: John wiley and Sons, 1986.